Tunable Resonant Narrow-Band Filter Based on Electro-optic Materials

Da Shu

ECOLE CENTRALE MARSEILLE

N° attribué par la bibliothèque

Réseaux résonnants accordables pour filtrage optique à bande étroite

THÈSE
Pour obtenir le grade de DOCTEUR
délivré par l'ECOLE CENTRALE MARSEILLE

Ecole Doctorale Physique et Sciences de la Matière
Discipline : *Optique, Photonique et Traitement d'image*

présentée et soutenue publiquement par Da SHU
le 7 Décembre 2012

Le directeur et co-directeur de thèse : Evgeni POPOV et Anne-Laure FEHREMBACH
Laboratoire d'accueil: *Institut Fresnel, équipe* C.L.A.R.T.E

Membres du jury:

Maria-Pilar BERNAL	*rapporteur*
Pierre CHAVEL	*examinateur*
Thomas DURT	*examinateur*
Anne-Laure FEHREMBACH	*codirectrice de thèse*
Ross MCPHEDRAN	*rapporteur*
Evgeni POPOV	*directeur de thèse*

2012

Contents

Introduction

A guided mode resonant (GMR) grating filter is a structure composed of a stack of a few dielectric layers in which a sub-wavelength grating is engraved. This kind of grating structures allows an incident plane wave to excite a mode of the stack which generates a resonance peak in the reflection and transmission spectra as a function of the wavelength. Their main interest is the thin spectral FWHM they can achieve: in practice, quality factors greater than 7000 have already been obtained[1]. Since their discovery in the 80s, they attracted a lot of interest, and various devices based on GMR have been developed, such as all-optical switching devices in WDM system[2], remote sensors[3], devices for security applications[4], etc.

Together with the expansion of application areas of the GMR filter, there are continuously new requirements for the filter performances to meet the practical needs, such as narrower filtering band, larger angular tolerance, oblique incidence, polarization independence, etc. Development of a tunable narrow band filter might be an effective way to enlarge the potential of the GMR grating filters.

The center wavelength of a GMR filter can be simply tuned by modifying the angles of incidence. Indeed, the resonance wavelength depends strongly on the angles of incidence (see for example reference[5]). Yet, this solution requires a sharp control of the angles of incidence which is not always possible. Moreover, changing the incidence angle also changes the reflection and transmission angles, making the filtered beam difficult to follow in practice. The tunability can also be obtained by modifying the parameters of the structure: the dimensions or the refractive indices. These modifications can be obtained for example by applying a strength, a magnetic or an electric field, or by controlling the temperature. For a review on the principles of tunability, applied to the Fabry-Perot filters, the interested reader can see the reference[6]. The impact of a modification of the thicknesses of the layer is quite complex to analyze, since the dilatation of the layers of different materials may be different. Moreover, these effects are usually weak. Among the effect that allow a modification of the indices, the electro-optic effect seems to be the most promising since it can be quite strong, targeted on a chosen area of the stack (the electro-optic layers), and independent from the other effects. That is why we concentrated our work on the electro-optic effect in resonant gratings. It must be noted that the modification of the parameters of the structure due to the temperature variations would be an interesting study in the scope of applications. The shift of the center wavelength with respect to the temperature modification during the use of the filter could be predicted, and insensitive designs could be proposed. However, these aspects have not been considered during this thesis.

The studies on guided mode resonant grating tunable by the electro-optic effects reported in the literature are not numerous. Magnusson and Wang firstly suggested that GMR filters can be used as tunable optical filters or as low-power optical switching devices[7]. Then theoretical studies[8] and other types of tunable GMR devices[2,3,9] have been demonstrated[10–12]. Some studies involve the E-O effect in liquid crystals to tune the resonance wavelength in dielectrics[13,14] or metallic (plasmonic)[15] GMR filters. Yet, most of these works are demonstrations of the possibility to tune the resonance wavelength using the E-O effect. Nothing is reported concerning a study aimed at understanding the underlying physics, and optimizing the tunability. Moreover, not all of the theoretical calculations reported take into account the anisotropy of the E-O crystal which is crucial in order to analyze the behavior of the component with respect to the incident polarization. At last, very few studies concern gratings having two-dimensional (2D) periodicity aiming to polarizationally invariant resonance effects.

Thesis Objective: In this thesis, we aim to develop the potential of resonant grating filters by studying the tunability properties of guided mode resonant gratings including a layer of electro-optic material.

The main questions that motivated our research are summarized as follows:

- How does the applied voltage affect the permittivity of E-O materials within different crystal orientations? What is the impact on the guided modes of the structure?
- What is the magnitude of the tunability achievable?
- How can the tunability be maximized? What are the favorable configurations? Is it possible to exhibit key parameters involved in the tunability?
- How does the anisotropy of the structure play on the characters of the GMR filter, such as: resonant peak linewidth and maximum, tunability, angular tolerance and polarization independence?

The research work that has been done during the thesis brought full or partial answers which are presented in the manuscript.

Thesis Overview
The manuscript is divided into four chapters:

- **Chapter 1** introduces the theoretical basis and the physical notions that are needed in the following of the manuscript, especially in Chapters 3 and 4. It is composed of two parts, one concerning the guided mode resonant gratings and the second the electro-optic effect. In the part devoted to GMR gratings, their physical principles, advantages and drawbacks are reminded. The solutions that have been proposed during the last twenty years to improve the performances of GMR grating for filtering applications are described and used as a starting point to design the structures studied in the following chapters. The concept of equivalent homogeneous planar structure is also introduced as a tool to estimate some optical properties of the filter.

  The rest of this chapter is devoted to a general introduction on the electro-optic effect, and how the refractive index can be modified by an external applied electric field. Both the linear and the quadratic E-O effect are described in this chapter.

- **Chapter 2** concerns the numerical method that was developed and used during the thesis to study the anisotropic resonant grating: the Fourier Modal Method. A brief description of the method is given in the general case when an anisotropic material is included as an homogeneous layer (which has been implemented during the thesis). It also mentions the output that can be obtained from the code and that is used to analyze the GMR filter characters throughout the chapters 3 and 4.

- **Chapter 3** concerns the material Lithium Niobate ($LiNbO_3$). We first chose the orientation of the crystal with respect to the static electric field with the purpose to maximize the influence of the E-O effect, and then study different modes excited in the grating structure, in order to figure out the relationship between the tunability of

the resonance peak and the modes. The performances of the whole structure, such as narrow filtering band, angular tolerance, tunability, polarization independence characters are analyzed and explained.

- **Chapter 4** presents our work on Barium Titanate based tunable resonant grating. Barium Titanate is interesting because of its large E-O effect coefficients. The same framework as for Chapter 3 is followed, but different conclusions are deduced because the orientation chosen for the crystal is different: the structure is anisotropic in the plane parallel to the direction of propagation of the guided modes. This fact leads to interesting observations on the behavior of the component with respect to the incident polarization.
- Finally, in the general **Conclusion** of the thesis, we cite several critic problems to be solved and also given some perspectives for the future work.

To complete the thesis, we also included two appendixes:

- **Appendix 1** shows the detailed derivation of several equations needed for the realization of the numeric tool based on the FMM. It contains the construction of the four blocks of the S matrix.
- **Appendix 2** is a summary of all the structures studied in the manuscript.

Chapter 1

Guided-Mode Resonant Grating and Electro-Optic Effect

In this chapter, we want to present some basic concepts of the guided mode resonant gratings and the electro-optic effect. A lot of theoretical work has been done to understand the physics of Guided Mode Resonant Gratings in various configurations[16]. We will give here a brief reminder of the most important results obtained especially concerning the optimization of the angular tolerance and the behavior with respect to the polarization of the incident wave.

The physics of the electro-optic effect is described by a well established theory[17]. We will introduce here the notations used to describe the modification by the electro-optic effect of the index ellipsoid of materials.

1.1 Guided Mode Resonance Grating

In this part, we introduce the component under study in this thesis: guided mode resonant (GMR) grating. We first explain the GRM Grating basic principle, then present the main interesting properties of GMR gratings for filtering applications. We recall the main drawbacks of GMR gratings, namely weak angular acceptance and strong sensitivity with respect to the incident wave polarization, then we present the configurations in which these drawbacks can disappear.

1.1.1 Guided-mode Resonant Grating: Basic Principles

Resonant gratings are simple structures composed of a stack of several dielectric layers on top of which a periodic nanostructure is engraved. The multilayer stack plays the role of a planar waveguide. A so called guided mode resonance phenomenon can occur due to the coupling of an eigenmode of the structure to the incident wave through one diffraction order of the grating. Figure 1.1 demonstrates the schematic diagram of a simple GMR structure.

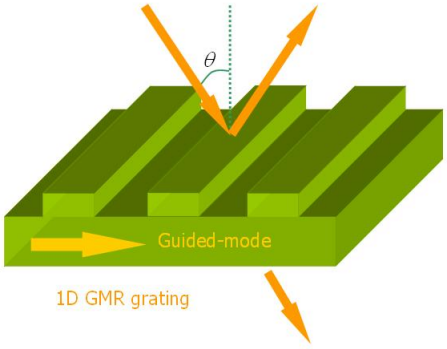

Figure 1.1 : *Schematic diagram of a one dimensional GMR filter structure.*

For example, for a grating having 1D periodicity and illuminated in a plane parallel to the direction of periodicity (classical incidence), the coupling condition of one mode through the m^{th} diffraction order writes:

$$| \sin\theta + m\frac{\lambda}{D} | \simeq n_f \quad , \tag{1.1}$$

where n_f is the effective index of the mode, D is the period of the grating, λ and θ are the incident wavelength and angle.

The coupling condition, in a more general case of incidence can also be written as:

$$\|\overrightarrow{k_{inc}} + \overrightarrow{K}\| \simeq \frac{2\pi}{\lambda} n_f \quad , \tag{1.2}$$

where $\overrightarrow{k_{inc}}$ is the in-plane incident wave vector, $\overrightarrow{K}$ is a vector of the reciprocal space of the grating. The coupling of the incident wave into the waveguide and the decoupling in the free space leads to a resonance peak in the reflectivity or transmittivity spectrum of the structure, as shown in Fig. 1.2.

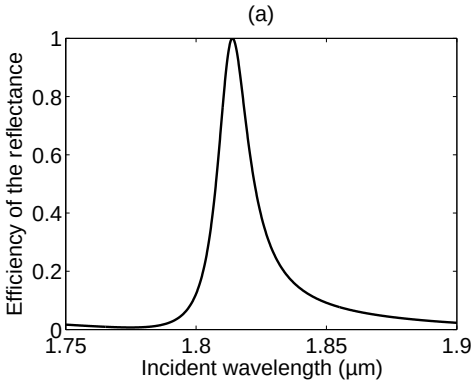

Figure 1.2 : *Reflection efficiency (structure 1.1 shown in Fig. 5.1 in Appendix 2) as a function of the incident wavelength λ.*

1.1.2 Equivalent Planar Structure

The grating structure modifies the effective modal index. It is possible to introduce an equivalent planar structure (without grating), which has optical properties as close as possible to the optical properties of the grating structure. For instance, the reflectivity of the equivalent structure will give a good estimation of the reflectivity of the grating structure without the resonance mode excitation, and the effective index of the mode will give a good estimation of the center wavelength of the peak using the coupling Eq. 1.2.

In the equivalent planar structure, the grating is replaced by a layer of homogenous material. The rest of the structure is kept unchanged as the following schema shows:

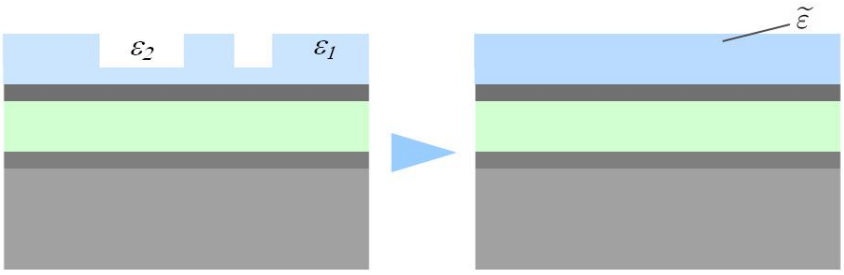

Figure 1.3 : *Schema of the equivalent planar structure.*

For example, the permittivity of the equivalent layer $\widetilde{\varepsilon}$ as a function of the permittivity of grating material ε_1 and of air ε_2 can be expressed as:

$$\widetilde{\varepsilon} = \varepsilon_1(1 - \frac{S_{hole}}{S_{total}}) + \varepsilon_2 \frac{S_{hole}}{S_{total}}, \tag{1.3}$$

where the S_{hole} is the area of the air holes, and $S_{total} = D^2$ is the area of one grating period. In other words, $\widetilde{\varepsilon}$ stands for the arithmetic mean of the permittivity of the grating.

Note that $\widetilde{\varepsilon}$ can be calculated in a different way using the numerical code based on the Fourier Modal Method, as it will be described in the chapter 2, so that $\widetilde{\varepsilon}$ becomes a tensor of anisotropic permittivity.

As said above, the equivalent planar structure can be used to obtain in a first approximation the propagation constant of the modes and the reflectivity of the resonant grating filter outside the resonance. We illustrate this below on an example. The structure considered is described in Fig. 5.2 (structure 3.1) in the Appendix 2.

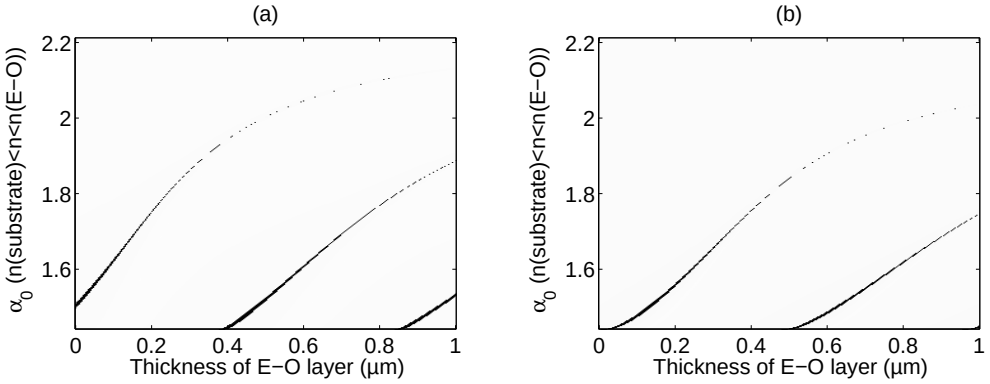

Figure 1.4 : *Reflected electric field as a function of the thickness of the $LiNbO_3$ layer with s polarized incident plane wave. (a). y direction component of reflected electric field; (b). x direction component of reflected electric field.*

We plot in Fig. 1.4 the amplitude of the reflected electric field as a function of the thickness h of the $LiNbO_3$ layer and the x component of the in plane evanescent incident wave number (the x - wave vector component normalized by the free-space wave number). We observe several resonant curves corresponding to modes of different orders and polarizations excited in the structure when the thickness of the $LiNbO_3$ layer varies. According to the modes coupling condition, taken under normal incidence on a grating with period D engraved on this stack, the center wavelength λ of a peak is approximately given by:

$$\lambda = \widetilde{\alpha}_g D \quad , \tag{1.4}$$

where $\widetilde{\alpha}_g \equiv n_f$ is the normalized component of the propagation vector along the x direction. Conversely, for the design of a structure, Eq. 1.4 gives us an approximate value of the period D which will give a peak at the chosen wavelength.

1.1.3 Some Important Properties for Filtering Applications

The first interesting property of the guided mode resonant grating is the proportionality between the spectral width of the peak and the modulation strength of the grating, that is to say the depth and the index contrast between the material of the layer and the grooves. As a consequence, for shallow gratings and weak index contrast the peak can be

very narrow (linewidth <0.5 nm), thus the resonant gratings can be used for narrow band filtering.

The second important property is that for particular symmetry of the structure, the reflectivity, or the transmissivity, or both of them, can reach a maximum of 100% close to the resonance. This can be demonstrated by using the energy conservation and the reciprocity theorem[18,19]. This is true as long as the material does not present absorption losses and if only the zero diffraction order of the grating is propagating in the substrate and the superstrate (sub-wavelength grating). For instance, a symmetry with respect to the axis normal to the plane of the layers (see Fig.1.5(a)) provides 100% of reflectivity at resonance. A symmetry with respect to a plane parallel to the plane of the layers (see Fig.1.5(b)) provides two peaks of 100% of reflectivity and 100% of transmissivity at two different wavelengths in the vicinity of the resonance. In any case, the reflectivity and transmissivity outside the peak are close to their values for the homogeneous planar structure. Hence, it is possible to obtain a reflection (notch) filter with a great rejection rate (ratio between the reflectivity at the maximum of the peak to that outside the peak). The equivalent planar structure has to be optimized as an anti-reflection stack, and the grating must be symmetric with respect to the normal of the layers. This kind of symmetry is easy to obtain in practice. On the other hand, to obtain a transmission (bandpass) filter, one has to use a mirror stack, and a structure which is symmetrical with respect to a plane parallel to the layer's plane. This kind of symmetry requires a grating at each side of the stack, or a grating in the middle of the stack, which is quite difficult to fabricate. Moreover, a dielectric mirror needs greater number of layers than an anti-reflective stack. As the thickness of the layers depends on the considered wavelength, this may be a strong drawback for example for applications at large wavelengths (mid infrared). That is the reason why most of the work on guided mode resonant gratings concerns reflection filters rather than transmission filters.

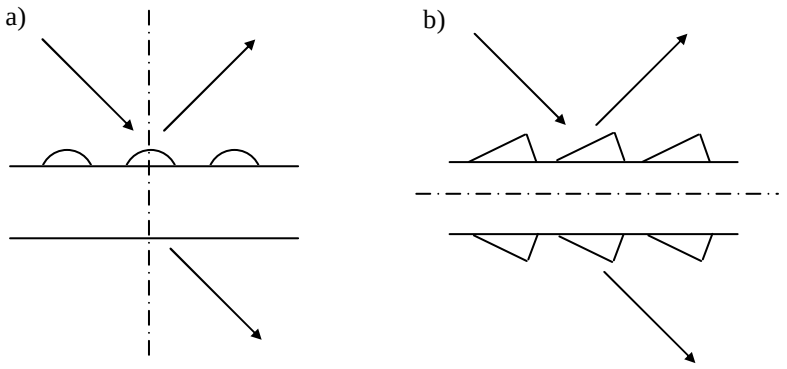

Figure 1.5 : *Resonant grating with: (a) a symmetry axis normal to the plane of the layers; (b) a symmetry plane parallel to the plane of the layers.*

Unfortunately, besides these interesting properties, it is well known that the resonant guided mode resonant filters in simple configurations have a weak angular acceptance, and the resonant peak depends strongly on the polarization of the incident wave. Hopefully, these drawbacks can be avoided by using some complex configurations which are presented in the next two paragraphs.

1.1.4 Angular Tolerances

From the coupling equation 1.1 it can be seen that in a simple configuration, the angular width of the peak varies in the same manner as the spectral width. Indeed, differentiating Eq. 1.1 leads to

$$\Delta\theta = \frac{|m|}{D|\cos(\theta)|}\Delta\lambda \tag{1.5}$$

It can be proved that in this case both the spectral and the angular width depends, besides on the grating depth, on the Fourier coefficient of the permittivity of the grating corresponding to the resonant diffraction order[16]. Hence, if the first diffraction order is used to excite the mode, the spectral and the angular width are both proportional to the first harmonic of the grating permittivity ε_1. In this configuration, it is not possible to obtain a small spectral width and a large angular tolerance. This may be a problem if the component can not be illuminated with a beam having a divergence smaller than the angular tolerance of the structure, because this will enlarge the spectral width of the peak and reduce the reflectivity maximum. In practice, if the component is fabricated using e-beam lithography, the grating area is a few millimeters square only, and a focused beam is necessary to illuminate the component. Moreover, in a recent study[20] it has been proved that the defaults of fabrication have an impact on the filter performances (spectral width and reduction of the maximum reflectivity). To avoid the deterioration of the filter performances, it is thus recommended to use a narrower beam, which covers smaller grating region to avoid fabrication defaults.

A solution to avoid the tight angular tolerances is found in normal incidence, when two counter-propagative modes can be excited in the structure. This would correspond to a crossing point between the dispersion curves of the two modes if they were not coupled to each others. However, the grating introduces a coupling between these two modes, which opens a gap in the dispersion relations of the modes close to the crossing point without the grating coupling. For the mode at the edge of the gap, it can be proved that the spectral width of the resonant peak still depends on the Fourier harmonic associated to the diffraction order used for the excitation of the mode (ε_1 if the resonant diffraction order is the first order). But the angular width of the peak now depends on the coupling strength between the two counter-propagative modes, which is related to the second Fourier harmonic of the grating permittivity ε_2 if the first diffraction order is resonant.

To increase ε_2 with respect to ε_1, a complex 1D basic pattern, composed of two grooves of different width has been proposed. For this so called 1D "bi-periodic" grating, the ε_2 coefficient can be much larger than ε_1, and a large $\Delta\theta/\Delta\lambda$ ratio can be obtained[21]. We report in Fig.1.6 a comparison between a 1D GMR Filter with a simple pattern and a 1D "bi-periodic" GMR Filter. When illuminated with a plane wave, the two structures can produce a peak with the same width. Yet, when they are illuminated with a Gaussian beam ($500\mu m$ diameter at waist), the peak obtained with the simple pattern structure is strongly deteriorated while that obtained with the "bi-periodic" GMR grating keeps the same form.

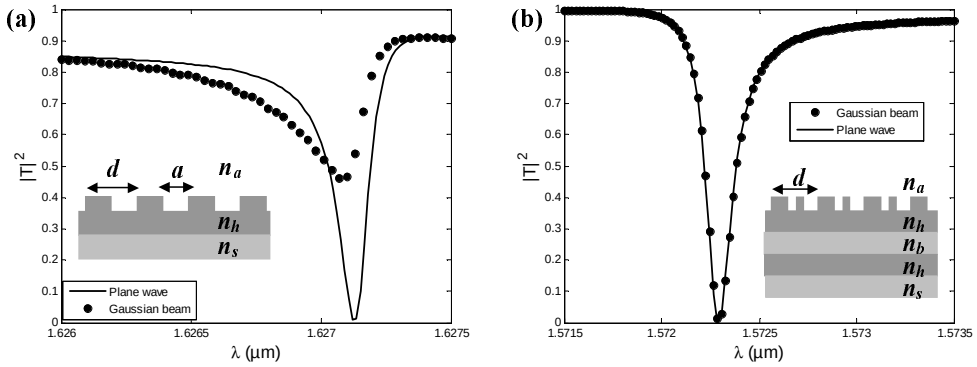

Figure 1.6 : *(figure from[21]) Transmissivity spectra for (a) a single groove grating (period 971 nm, groove width 250 nm, height 13 nm, refractive index n_a=1, n_h=2.07, n_b=1.47, and n_s=1.448, and layer thickness, from top to bottom, 65, 113, and 196 nm). Fourier coefficients: ϵ_1=0.76, ϵ_2=0.52. (b) Doubly periodic grating (period 1047.5 nm, groove widths 241.25 and 281.25 nm, height 382.6 nm, refractive index n_a=1,n_h =2.07, n_b=1.47, and n_s=1.448, and layers thickness, from top to bottom, 62.5, 263.5, and 79.1 nm). Fourier coefficients: ϵ_1=0.09, ϵ_2=1.04.*

1.1.5 Behavior with Respect to the Incident Polarization

The independence of the filter characteristics with respect to the polarization of the incident beam is another crucial property that is often requested in applications where the incident light is unpolarized or the polarization unknown. Yet, in a simple configuration where only one mode is excited, the resonance depends strongly on the polarization: it is maximum for one polarization, while for the orthogonal polarization, the resonance is not excited. For example, if the mode is TE (electric field perpendicular to the direction of propagation) and the plane of incidence parallel to a direction of periodicity, the mode can not be excited with a p polarization (magnetic field perpendicular to the plane of incidence). An important theoretical work has been developed in reference[22]. We remind in the following the most relevant conclusions.

We consider the reflectivity matrix $\mathbf{R}$ which relates the incident field to the reflected field in the zero order of diffraction of the grating. It is composed with four coefficients r_{ss}, r_{ps}, r_{sp} and r_{pp} corresponding respectively to the conversion of the field amplitude from s incident field to s reflected field, s incident field to p reflected field, p incident field to s reflected field, and p incident field to p reflected field:

$$\mathbf{R} = \begin{bmatrix} r_{ss} & r_{ps} \\ r_{sp} & r_{pp} \end{bmatrix} \tag{1.6}$$

It can be proved that the energy reflection coefficient $|R|^2$ can be expressed with respect to the eigenvalues L_1, L_2 and eigenvectors $\mathbf{V}_1$, $\mathbf{V}_2$ of the matrix $\mathbf{R}^*\mathbf{R}$, where $\mathbf{R}^*$ is the transposed and complex conjugated of $\mathbf{R}$:

$$|R|^2 = L_1|\mathbf{V}_1^*.\mathbf{I}|^2 + L_2|\mathbf{V}_2^*.\mathbf{I}|^2 \tag{1.7}$$

where $\mathbf{I}$ is a unitary vector collinear to the electric field of the incident wave. It is important to note that as $\mathbf{R}^*\mathbf{R}$ is an Hermitian matrix, then L_1 and L_2 are real and positive and its eigenvectors are orthogonal in the sense that their Hermitian scalar product is null: $\mathbf{V}_1^*.\mathbf{V}_2 = 0$. From Eq. 1.7, it can be seen that when the polarization of the incident wave varies, the reflectivity bounds are L_1 and L_2. Thus, $L_1 = L_2$ is a sufficient and necessary

condition for which the reflectivity does not depend on the polarization. Moreover, it is observed numerically that when an eigenmode is excited, one eigenvalue (for example L_1) is resonant. The associated eigenvector $\mathbf{V}_1$ corresponds to the field of the incident wave that allows the full excitation of the mode. If the incident field is collinear to the second eigenvector $\mathbf{V}_2$, the eigenmode is not excited. Hence, an important conclusion is that the simultaneous excitation (for the same wavelength and angles of incidence) with orthogonal polarization of two eigenmodes is the prerequisite of the polarization independence. Moreover, note that obtaining the same reflectivity for an s-polarized and a p-polarized incident wave does not mean that the structure is polarization independent, unless the s and p polarizations correspond to the eigenvectors of the $\mathbf{R}^s * \mathbf{R}$ matrix. On the other hand, if the s an p reflectivities reach 100% for the same angle and wavelength of incidence, it can be said that the structure is polarization independent for this incidence. Several solutions have been proposed to excite two modes with orthogonal polarizations for the same angle and wavelength of incidence. For example, one can excite a TE and a TM mode with a 1D grating under oblique incidence along the direction of periodicity. It is also possible to illuminate a grating along a plane of symmetry. In this case, two modes can be excited, one with a field symmetrical and the other anti-symmetrical with respect to the plane of incidence[23]. These two modes can be excited at the same wavelength and angle of incidence for suitable grating parameters.

In the case of grating having 2D periodicity and illuminated under normal incidence, four counter-propagative eigenmodes are exited along the two directions of periodicity, and couple to each other by pairs, which ensures the polarization independence. Moreover, this configuration is favorable for the angular tolerance enhancement. In the following, we will work with this kind of a 2D "bi-periodic" gratings illuminated under normal incidence. A "bi-periodic" grating with 2D periodicity has a period D and contains four air holes with different diameters, holes A and A' have the same diameter D_1, the diameter is D_2 for hole B, and D_3 for hole C (see Fig. 1.7). Note that the holes A and A' have the same diameter so that the grating is symmetrical with respect to the normal to the layers. The values of the diameters are designed to enhance ε_2 with respect to ε_1 and then optimize the angular tolerance.

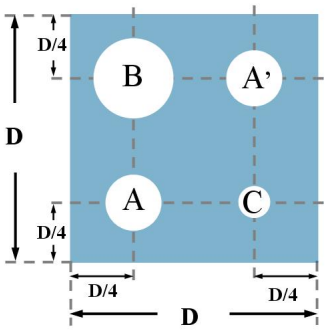

Figure 1.7 : *Top view of the designed grating pattern.*

Reference[22] firstly put up the conception of this kind of structure and reference[21] introduces in detail the experimental realization of a narrow band, polarization independent filter based on this configuration.

We are interested in designing a filter with a tunable center wavelength. This could be done simply by changing the angle of incidence, but this solution is difficult to realize since

a precise control of the rotation of the sample is required, and moreover, the direction of the reflected beam changes, together with the incident beam. We prefer studying a solution that relies on a modification of the effective index of the mode, which will lead, according to the coupling condition, to a shift of the peak. There are various approaches to modify the refractive index of a material, such as applying a magnetic field, a mechanical stress, etc[24]. In particular, we will focus on the electro-optic effect (modification of the refractive index when an electric field is applied) with a static electric field.

1.2 Tunability Using the Electro-optic Effect

For some specific materials, optical properties can change when they are subjected to a static or low-frequency (up to several GHz) externally applied electric field. This is known as the electro-optic effect (E-O effect)[24]. In this section, we give a general introduction of the E-O effect in the materials.

1.2.1 Electro-Optic Effect Applications

Since the electro-optic effect was discovered, it has been widely applied in various domains. The linear E-O effect can be used to make light modulators, deflectors and filters.[25–27] It allows in particular the modulation of laser beams up to several gigahertz.[28].

For example, the electro-optic modulator is an optical device used to modulate a beam of light by a signal-controlled element which is affected by electro-optic effect. These kind of modulators are key components in high-speed and wide bandwidth optical communication systems. Both $LiNbO_3$ and $BaTiO_3$ are attractive ferroelectric materials for this application[29,30]. Taking advantage of the Pockels effect, an applied external electric field will cause variation in phase retardation which can be used to manipulate the polarization state of light beam. In this phase modulator working together with a polarization analyzer, the different phase delays will be converted into an intensity variation of the light, realizing a so called amplitude modulation. The modulation also may change the frequency, or the direction of the modulated beam[31]. These guided-wave modulators can be designed in chips and associated with fiber systems. In particular, lithium niobate and barium titanate, the two typical electro-optic materials widely used are studied in this thesis. E-O tunable filters can be designed in a variety of different ways[32–34]. These include birefringent, Solc, Fabry-Perot, and tunable Bragg filters. The particular design selected depends on whether narrow transmission, suppression of side lobes, wide field of view, high sensitivity, high-speed response, or other features are desired. Tunable spectral filters have been demonstrated in a variety of materials for the different configurations with some experimental success. E-O tunable filters offer the potential for electrically controlling the filter bandpass and bandwidth. Furthermore, certain devices have been demonstrated that are polarization independent and have been used as E-O laser modulators.

1.2.2 Modification of the Index Ellipsoid

The optical properties of an anisotropic material medium are characterized by the optical index ellipsoid, described by the equation:

$$(\frac{x_1}{n_1})^2 + (\frac{x_2}{n_2})^2 + (\frac{x_3}{n_3})^2 = 1 \quad , \tag{1.8}$$

where n_1, n_2, n_3 are the principal refractive indices, which also correspond to the principal lengths along the ellipsoid axes. If the medium is uniaxial, then $n_1 = n_2 = n_o, n_3 = n_e$; for a biaxial medium, $n_1 \neq n_2 \neq n_3$.

When an external static electric field **E** is applied to an E-O medium, its index ellipsoid will be modified according to the equation:

$$\sum_{i=1}^{3}\sum_{j=1}^{3}\left(\frac{1}{\widetilde{n}^2}\right)_{ij} x_i x_j = 1 \quad , \tag{1.9}$$

with the following relationship:

$$(\frac{1}{\widetilde{n}^2})_{ij} = (\frac{1}{n_0^2})_{ij} + (\Delta\frac{1}{n^2})_{ij}(\mathbf{E}) \quad , \tag{1.10}$$

where $\widetilde{n}$ is the modified new refractive index, $(\frac{1}{n_0^2})_{ij}$ represents the coefficients of the index ellipsoid equation without applied electric field , which means that $(\frac{1}{n_0^2})_{11} = \frac{1}{n_1^2}$, $(\frac{1}{n_0^2})_{22} = \frac{1}{n_2^2}$, $(\frac{1}{n_0^2})_{33} = \frac{1}{n_3^2}$ and $(\frac{1}{n_0^2})_{ij} = 0$ for $i \neq j$. The last term in the Eq. 1.10 stands for the modification of the index caused by the static electric field **E**. This is the key variable, and it will be explained in detail in the following subsection.

1.2.2.1 Electro-optic Coefficients

The term electro-optic effect encompasses a number of distinct phenomena, which may have strong effect on the refractive index of the material and can be subdivided into two basic categories[35]:

- (a) linear electro-optic effect: the change in the refractive index is linearly proportional to the electric field. It is often called the Pockels effect, since Friedrich Pockels discovered it in 1893;
- (b) quadratic electro-optic effect: the change in the refractive index is proportional to the square of the electric field. It is also known as the Kerr effect since John Kerr discovered it in 1875 in optically isotropic media such as liquids or gases.

From the previous section we know that an applied external electric field will modify the refractive index according to Eq. 1.10, and the last term of this equation can be expanded into:

$$(\Delta\frac{1}{n^2})_{ij} = \underbrace{\sum_{k} r_{ijk}E_k}_{linear} + \underbrace{\sum_{k,l} s_{ijkl}E_k E_l}_{quadratic} \quad , \tag{1.11}$$

where E_k stands for the component of the applied electric field along the k direction. The constants r_{ijk} are the linear electro-optic coefficients, and s_{ijkl} are the quadratic electro-optic coefficients. We neglect higher order terms in the expansion because they are too small for most applications.

In most practical applications of the electro-optic effect, the quadratic effect is expected to be small as compared to the linear effect and is often neglected when the linear effect is present. There are some crystals (those with centrosymmetric point groups) in which the linear effect vanishes and the quadratic effect becomes the dominant phenomenon.

1.2.2.2 Coefficient Notation Simplification

For the linear E-O effect coefficient, the ordinary notations have three indices, $i, j, k = 1, 2, 3$, so that it is a third-rank tensor with $3^3 = 27$ elements. From symmetry considerations ($(\Delta\frac{1}{n^2})_{ij} = (\Delta\frac{1}{n^2})_{ji}$), it is convenient to renumber the pair of indices (i,j), $i, j = 1, 2, 3$ as a single index $i = 1, 2, ..., 6$ in accordance with the rule in Table 1.1:

Table 1.1 : *Table for the index i that represents the pair if indices* (i, j).

j \ i	1	2	3
1	1	6	5
2	6	2	4
3	5	4	3

Thus the linear E-O coefficients can be represented by only 18 r_{ij} elements.

For the same reasons, the same rule applies for the indices i and j of the quadratic E-O effect coefficients s_{ijkl}. Moreover, the coefficients s_{ijkl} are also invariant under permutations of the indices k and l, so that $k, l = 1, 2, 3$ can be renamed in another single index $k = 1, 2, ..., 6$ using the same rule as in the Table above. It is then useful to introduce a vector $E^{(2)}$ which contains 6 elements given by $E_k^{(2)} = E_k^2$ for $k = 1$, 2 or 3, and $E_4^{(2)} = 2E_2E_3$, $E_5^{(2)} = 2E_1E_3$ and $E_6^{(2)} = 2E_1E_2$. Thus the quadratic E-O effect coefficients can be expressed by a $6 \times 6 = 36$ elements instead of a $3^4 = 81$ elements.

Considering the general case, in which Pockels coefficients and Kerr coefficients tensors are both full matrices, assuming that there is an external electric field $E = (E_1, E_2, E_3)$ applied, with a coordinate system consistent with the orientation of the crystal, the modified index is given by:

$$(\Delta\frac{1}{n^2})_{ij} = \begin{bmatrix} r_{11} & r_{12} & r_{13} \\ r_{21} & r_{22} & r_{23} \\ r_{31} & r_{32} & r_{33} \\ r_{41} & r_{42} & r_{43} \\ r_{51} & r_{52} & r_{53} \\ r_{61} & r_{62} & r_{63} \end{bmatrix} \begin{bmatrix} E_1 \\ E_2 \\ E_3 \end{bmatrix} + \begin{bmatrix} s_{11} & s_{12} & s_{13} & s_{14} & s_{15} & s_{16} \\ s_{21} & s_{22} & s_{23} & s_{24} & s_{25} & s_{26} \\ s_{31} & s_{32} & s_{33} & s_{34} & s_{35} & s_{36} \\ s_{41} & s_{42} & s_{43} & s_{44} & s_{45} & s_{46} \\ s_{51} & s_{52} & s_{53} & s_{54} & s_{55} & s_{56} \\ s_{61} & s_{62} & s_{63} & s_{64} & s_{65} & s_{66} \end{bmatrix} \begin{bmatrix} E_1^2 \\ E_2^2 \\ E_3^2 \\ 2E_2E_3 \\ 2E_1E_3 \\ 2E_1E_2 \end{bmatrix} \tag{1.12}$$

1.2.2.3 E-O effect Tensor of a Typical Material

Both the linear and quadratic electro-optic coefficients depend on the crystalline symmetry. In this part, we give the form of E-O tensor for the two classes of symmetry to which belong the materials under study in chapters 3 and 4, $LiNbO_3$ and $BaTiO_3$.

- Trigonal symmetry
  Class 3m (for example:$LiNbO_3$)

$$Pockels \begin{bmatrix} 0 & -r_{22} & r_{13} \\ 0 & r_{22} & r_{13} \\ 0 & 0 & r_{33} \\ 0 & r_{51} & 0 \\ r_{51} & 0 & 0 \\ -r_{22} & 0 & 0 \end{bmatrix} \quad Kerr \begin{bmatrix} s_{11} & s_{12} & s_{13} & s_{14} & 0 & 0 \\ s_{12} & s_{11} & s_{13} & -s_{14} & 0 & 0 \\ s_{31} & s_{31} & s_{33} & 0 & 0 & 0 \\ s_{41} & -s_{41} & 0 & s_{44} & 0 & 0 \\ 0 & 0 & 0 & 0 & s_{44} & s_{41} \\ 0 & 0 & 0 & 0 & s_{14} & \frac{s_{11}-s_{12}}{2} \end{bmatrix}$$

- Tetragonal symmetry
  Class 4mm (for example:$BaTiO_3$)

$$Pockels \begin{bmatrix} 0 & 0 & r_{13} \\ 0 & 0 & r_{13} \\ 0 & 0 & r_{33} \\ 0 & r_{42} & 0 \\ r_{51} & 0 & 0 \\ 0 & 0 & 0 \end{bmatrix} \quad Kerr \begin{bmatrix} s_{11} & s_{12} & s_{13} & 0 & 0 & 0 \\ s_{12} & s_{11} & s_{13} & 0 & 0 & 0 \\ s_{31} & s_{31} & s_{33} & 0 & 0 & 0 \\ 0 & 0 & 0 & s_{44} & 0 & 0 \\ 0 & 0 & 0 & 0 & s_{44} & 0 \\ 0 & 0 & 0 & 0 & 0 & s_{66} \end{bmatrix}$$

1.3 Summary

This chapter can be considered as the introductory paragraph of the whole thesis. It is divided into two separate parts: the first one introducing guided-mode resonant gratings, and the second one discussing the electro-optic effect. In the part concerning GMR gratings, we mainly introduced the physical principle of this type of grating. We emphasized the importance of the planar equivalent structure and the link between the effective index of the guided mode and the center wavelength of the peak. We introduced the "bi-periodic" two dimensional grating pattern. All the simulation works in the following chapters are based on this grating pattern, in order to optimize the angular tolerance of the designed filters. At last, we gave some elements of theory concerning the behavior of guided mode resonant gratings with respect to the polarization of the incident wave: a necessary condition to ensure a polarization independent behavior is the excitation, with orthogonal polarizations, of two modes for the same wavelength and angles of incidence.

The electro-optic effect is the second physical phenomenon introduced in this first chapter. The external voltage applied to the E-O material causes the modification of its refractive index. By taking advantage of this, we will in the following confirm the possibility to tune the center wavelength of the filter and study the effects introduced by the anisotropy of the material. The linear electro-optic effect in two E-O materials, namely Lithium Niobate and Barium Titanate, is analyzed in chapter 3 and chapter 4 respectively. The effects caused by the quadratic electro-optic effect involved with the Barium Titanate is also explained in the chapter 4.

Chapter 2

Numeric Tool Based on the Fourier Modal Method (FMM)

2.1 Introduction

The key subject of this chapter is presenting the realization of a numeric tool, which was used to analyze the behavior of the tunable GMR filters involved in the thesis. This tool is based on the Fourier Modal Method (FMM), which is also known as rigorous coupled waves analysis (RCWA). Generations of researchers have worked on the electromagnetic theory of gratings and tried to implement a stable and effective numerical solution of the electromagnetic behavior for various types of gratings. My work also is involved in this search, and it is based on a numerical code written by A.-L. Fehrembach. I have developed a new version of this program, which allows the treatment of multilayer structures containing both homogenous anisotropic layers and periodic isotropic grating structures.

We will firstly introduce the development of the FMM and the entire algorithm for the general grating problem. Further on, the approach dealing with anisotropic case will be developed. Some important functions of the developed numeric tool will be described at the end of this chapter.

2.2 Basis of the Numerical Resolution of the Diffraction by a Grating

2.2.1 Statement of the Problem

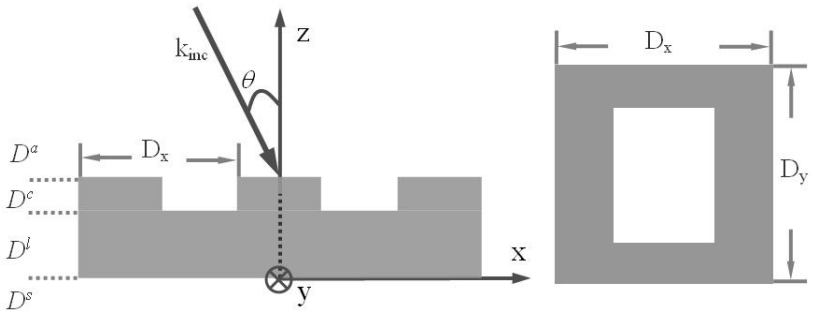

Figure 2.1 : *The geometry schematic diagram of the diffraction grating of thickness h and period D_x along x, D_y along y, illuminated by a plane wave with wavelength λ and angle of incidence θ.*

Figure 2.1 illustrates the schematic diagram of a two-dimensional periodic grating structure illuminated by a plane wave. The area D^a (z > d+h) is the incident medium that consists of a dielectric material characterized by a homogeneous real permittivity ϵ^a; Region D^s (z < 0), can be made of materials with complex permittivity ϵ^s; Intermediate medium D^c (d <z <d+h) is the grating part, whose thickness equals to h. Medium D^l (0 <z <d) is the multilayer stack part, which can be composed of homogeneous isotropic or anisotropic materials. Note that in the numerical code, the grating part is not necessary at the top of the stack.

2.2.2 Fourier Transformation of Permittivity and Pseudoperiodicity of the Field

In the region D^c, the permittivity can be complex and is modulated periodically along the x axis with a period denoted D_x, along y axis with a period denoted D_y. The permittivity of the grating can be decomposed into Fourier series:

$$\epsilon_c(x,y,z) = \sum_{m=-\infty}^{+\infty} \sum_{n=-\infty}^{+\infty} \epsilon_{mn}(z) \exp\left(imK_x x + inK_y y\right), \tag{2.1}$$

where K_x is the lattice vector component along the x axis, $K_x = \frac{2\pi}{D_x}$; K_y is the lattice vector component along the y axis, $K_y = \frac{2\pi}{D_y}$.

The incident plane wave has an unit amplitude and its wavelength in vacuum equals to λ, it propagates in the medium D^a and is incident on the interface between media D^a and D^c under the angle θ relative to the axis z. We consider the time harmonic case, so that the time dependence $\exp(-i\omega t)$ can be skipped. We assume that the grating surface is infinite. Due to the periodicity, the denoted total field $\mathbf{F}$ satisfies the following relationship:

$$\mathbf{F}(x + D_x, y + D_y, z) = \exp\left(i(\alpha_0 D_x + \beta_0 D_y)\right)\mathbf{F}(x,y,z), \tag{2.2}$$

for further, it can be represented by the Fourier series with its Fourier components $\mathbf{F}_{mn}(z)$:

$$\mathbf{F}(x,y,z) = \sum_{n=-\infty}^{\infty} \sum_{m=-\infty}^{\infty} \mathbf{F}_{mn}(z) \exp\left(i(\alpha_m x + \beta_n y)\right), \tag{2.3}$$

with

$$\alpha_m = \alpha_0 + mK_x, \quad \beta_n = \beta_0 + nK_y, \tag{2.4}$$

The representation in Eq. 2.3 is called a pesudo-Fourier serie for the quasi-periodic total field function.

Our aim will clearly be the determination of the function $\mathbf{F}_{mn}(z)$, which corresponds to the amplitude of the (m,n)-th diffraction order.

2.2.3 Rayleigh Expansions in the Substrate and Superstrate

As shown in Fig. 2.1, the substrate D^s and superstrate D^a media are homogeneous, the electromagnetic fields in these two areas $\mathbf{F}^{(a)}$ and $\mathbf{F}^{(s)}$ can be directly written in the form of Rayleigh expansions:

$$\mathbf{F}^{(a)} = \mathbf{I}\exp[i(\alpha_0 x + \beta_0 y - \gamma_{00}^{(a)} z)] + \sum_{m,n} \mathbf{R}_{mn} \exp[i(\alpha_m x + \beta_n y + \gamma_{mn}^{(a)} z)],$$

$$\mathbf{F}^{(s)} = \sum_{m,n} \mathbf{T}_{mn} \exp[i(\alpha_m x + \beta_n y - \gamma_{mn}^{(s)} z)] \quad , \tag{2.5}$$

where $\mathbf{F}$ stands for electric $\mathbf{E}$ or magnetic field $\mathbf{H}$, and $\mathbf{I}$, $\mathbf{R}$, $\mathbf{T}$ are, respectively, the incident, reflected or transmitted electric or magnetic fields. Meanwhile, the component of the wavevector for the incident wave and the (m, n) diffraction order are given by:

$$\alpha_0 = k^{(a)} \sin\theta \cos\varphi, \quad \beta_0 = k^{(a)} \sin\theta \sin\varphi, \quad \gamma_{00}^{(a)} = k^{(a)} \cos\theta, \tag{2.6}$$

$$\alpha_m = \alpha_0 + mK_x, \quad \beta_n = \beta_0 + nK_y, \quad \gamma_{mn}^{(a,s)} = [k^{(a,s)2} - \alpha_m^2 - \beta_n^2]^{1/2}, \tag{2.7}$$

where φ is the azimutal angle of incidence, $k^{(a,s)2} = k_0^2 n^{(a,s)2}$, and the sign of $\gamma_{mn}^{(a,s)}$ should be chosen such that

$$Re[\gamma_{mn}^{(a,s)}] + Im[\gamma_{mn}^{(a,s)}] > 0. \tag{2.8}$$

2.3 Fourier Modal Method (FMM)

In order to determinate the field within the region D^s, we use the Fourier Modal Method, which will be detailed in this section.

2.3.1 Introduction

The Fourier modal method (FMM) was at first proposed by Moharam and Gaylord in 1981[36] and has quite a long history in the field of rigorous diffraction modeling. The general idea of FMM is the same as of the more general differential method and lies in expanding all the electromagnetic quantities (for example, electric field **E**, magnetic field **H** , permittivity tensor ϵ, permeability tensor μ) into the Fourier series. Starting from the Maxwell equation, the field in substrate and superstrate can be written as Rayleigh expansions, whereas inside the inhomogeneous (grating) region the Fourier components depend on the z-coordinate. Maxwell equations are then transformed into an system of infinite number of first-order ordinary differential equations. If the optogeometrical parameters of the grating region are z-invariant, this system can be solved by the eigenvalues/eigenvectors technique. Then using the limit condition at the grating interfaces it is possible to calculate the field everywhere.

In order to implement the theory and to find a numerical solution of the diffraction problem, it is necessary to truncate the Fourier series and the number of equations. One of the most important criterium in verifying the solution is a test of convergence with respect to the truncation parameter.

The first formulations of both differential method and FMM suffered from the beginning from slow convergence in the case of metallic gratings having 1D periodicity in TM (transverse magnetic) polarization. In the 90s the reason for this slow convergence has been established[37–40]. In fact, it is due to two factors: (i) growing exponential terms corresponding to the evanescent diffraction orders, and (ii) inadequate factorization in the Fourier space of the product of the permittivity and the electric field. The elimination of these two factors that spoiled the performance has been found in introducing the so-called scattering (S) matrix propagation algorithm, and in establishing the so-called inverse rule of Fourier factorization[39]. For gratings having 2D periodicity, in 2001, Popov and Nevière[41,42] presented a new general differential method but without implementation details and numerical data for 2D periodical gratings.

In the grating region, we use the algorithm proposed by Li for 2D gratings[43].

In 2003, Zeng et al[44] presented a Fourier modal analysis of crossed anisotropic gratings that permitted both the permittivity and permeability in the grating region to be tensorial and assumed the grating structure is orthogonal in two periodic directions. This analysis can be a good reference for our study and is used in describing the anisotropic planar section of the structure. We first consider a general case, which means that there is no restrictions on the permittivity and permeability tensors of the medium in the region D^l.

2.3.2 Fourier Representation of Maxwell Equations

In chapter 1, we have explained that our research focus on a grating structure in which both isotropic dielectric material grating, homogenous isotropic and anisotropic layers are involved at the same time. We describe in the following how each case is treated in the numerical code. We especially emphasize the case of the homogeneous anisotropic layer which has been implemented in the code during the thesis.

2.3.2.1 Homogenous Anisotropic Layer

We start from the time-harmonic Maxwell Equation:

$$\begin{aligned} \nabla \times \mathbf{H} &= \frac{\partial \mathbf{D}}{\partial t} = -i\omega\epsilon_0\epsilon_r\mathbf{E} \\ \nabla \times \mathbf{E} &= -\frac{\partial \mathbf{B}}{\partial t} = i\omega\mu_0\mu_r\mathbf{H}, \end{aligned} \tag{2.9}$$

where $\mathbf{E}$ and $\mathbf{H}$ denote the complex vectors of electric and magnetic field, ϵ_0 and μ_0 are the permittivity and permeability in vacuum, $\epsilon_r = \begin{bmatrix} \epsilon_{11} & \epsilon_{12} & \epsilon_{13} \\ \epsilon_{21} & \epsilon_{22} & \epsilon_{23} \\ \epsilon_{31} & \epsilon_{32} & \epsilon_{33} \end{bmatrix}$ and $\mu_r = \begin{bmatrix} \mu_{11} & \mu_{12} & \mu_{13} \\ \mu_{21} & \mu_{22} & \mu_{23} \\ \mu_{31} & \mu_{32} & \mu_{33} \end{bmatrix}$ are the matrix form of permittivity and permeability tensors for a general anisotropic medium.

The next step is to replace the electric field and magnetic field by their pseudo-Fourier transform (Eq. 2.3). When projected on the coordinate axis, these equations lead to a set of six coupled partial differential equations:

$$i\beta[\mathbf{H}]_z - \frac{\partial}{\partial z}[\mathbf{H}]_y = -i\omega\epsilon_0(\epsilon_{11}[\mathbf{E}]_x + \epsilon_{12}[\mathbf{E}]_y + \epsilon_{13}[\mathbf{E}]_z) \tag{2.10}$$

$$-i\alpha[\mathbf{H}]_z + \frac{\partial}{\partial z}[\mathbf{H}]_x = -i\omega\epsilon_0(\epsilon_{21}[\mathbf{E}]_x + \epsilon_{22}[\mathbf{E}]_y + \epsilon_{23}[\mathbf{E}]_z) \tag{2.11}$$

$$-i\alpha[\mathbf{H}]_y - i\beta[\mathbf{H}]_x = -i\omega\epsilon_0(\epsilon_{31}[\mathbf{E}]_x + \epsilon_{32}[\mathbf{E}]_y + \epsilon_{33}[\mathbf{E}]_z) \tag{2.12}$$

$$i\beta[\mathbf{E}]_z - \frac{\partial}{\partial z}[\mathbf{E}]_y = i\omega\mu_0(\mu_{11}[\mathbf{H}]_x + \mu_{12}[\mathbf{H}]_y + \mu_{13}[\mathbf{H}]_z) \tag{2.13}$$

$$-i\alpha[\mathbf{E}]_z + \frac{\partial}{\partial z}[\mathbf{E}]_x = i\omega\mu_0(\mu_{21}[\mathbf{H}]_x + \mu_{22}[\mathbf{H}]_y + \mu_{23}[\mathbf{H}]_z) \tag{2.14}$$

$$-i\alpha[\mathbf{E}]_y - i\beta[\mathbf{E}]_x = i\omega\mu_0(\mu_{31}[\mathbf{H}]_x + \mu_{32}[\mathbf{H}]_y + \mu_{33}[\mathbf{H}]_z), \tag{2.15}$$

where $\frac{\partial}{\partial x}$ and $\frac{\partial}{\partial y}$ have been replaced by $i\alpha$ and $i\beta$, α and β are diagonal matrices with diagonal elements $(\alpha)_{mn} = \delta_{mn}\alpha_n \equiv \delta_{mn}(\alpha_0 + n\frac{2\pi}{D_x})$ and $(\beta)_{mn} = \delta_{mn}\beta_n \equiv \delta_{mn}(\beta_0 + n\frac{2\pi}{D_y})$ respectively. Here α_0 (β_0) is the x(y)-component of the propagation vector and δ_{mn} is the Kronecker delta symbol. $[\mathbf{F}]_a$ is a column vector containing the Fourier components of F_a for F representing either the electric field or magnetic field and a being equal to x, y or z.

From Eq. 2.11 and 2.14 we can find that vectors $[\mathbf{E}_z]$ and $[\mathbf{H}_z]$ can be expressed in term of $[\mathbf{E}_x]$, $[\mathbf{E}_y]$, $[\mathbf{H}_x]$, $[\mathbf{H}_y]$ only , which are the solution of the system of equations 2.10, 2.11, 2.13 and 2.14. They are listed as follow:

$$\begin{aligned} [\mathbf{E}]_z &= -\frac{\alpha}{\omega\epsilon_0\epsilon_{33}}[\mathbf{H}]_y + \frac{\beta}{\omega\epsilon_0\epsilon_{33}}[\mathbf{H}]_x - \frac{\epsilon_{31}}{\epsilon_{33}}[\mathbf{E}]_x - \frac{\epsilon_{32}}{\epsilon_{33}}[\mathbf{E}]_y \\ [\mathbf{H}]_z &= \frac{\alpha}{\omega\mu_0\mu_{33}}[\mathbf{E}]_y + \frac{\beta}{\omega\mu_0\mu_{33}}[\mathbf{E}]_x - \frac{\mu_{31}}{\mu_{33}}[\mathbf{H}]_x - \frac{\mu_{32}}{\mu_{33}}[\mathbf{H}]_y, \end{aligned} \tag{2.16}$$

then we substitute these two expressions into the other four equations and order to eliminate $[\mathbf{E}_z]$ and $[\mathbf{H}_z]$. We thus obtain a set of first-order differential equations of the form:

$$\frac{d}{dz}\begin{pmatrix}[\mathbf{E}_x]\\ [\mathbf{E}_y]\\ [\mathbf{H}_x]\\ [\mathbf{H}_y]\end{pmatrix} = \mathbf{M}\begin{pmatrix}[\mathbf{E}_x]\\ [\mathbf{E}_y]\\ [\mathbf{H}_x]\\ [\mathbf{H}_y]\end{pmatrix} \quad , \tag{2.17}$$

where $\mathbf{M}$ is a known 4×4 block matrix $\begin{bmatrix} M_{11} & M_{12} & M_{13} & M_{14}\\ M_{21} & M_{22} & M_{23} & M_{24}\\ M_{31} & M_{32} & M_{33} & M_{34}\\ M_{41} & M_{42} & M_{43} & M_{44}\end{bmatrix}$ with elements given as follows:

$$\begin{aligned}
M_{11} &= -i(\frac{\alpha\epsilon_{31}}{\epsilon_{33}} + \frac{\mu_{23}\beta}{\mu_{33}})\\
M_{12} &= -i(\frac{\alpha\epsilon_{32}}{\epsilon_{33}} + \frac{\mu_{23}\alpha}{\mu_{33}})\\
M_{13} &= \frac{i}{\omega\epsilon_0}[\frac{\alpha\beta}{\epsilon_{33}} + k_0^2(\mu_{21} - \frac{\mu_{23}\mu_{31}}{\mu_{33}})]\\
M_{14} &= \frac{i}{\omega\epsilon_0}[\frac{-\alpha^2}{\epsilon_{33}} + k_0^2(\mu_{22} - \frac{\mu_{23}\mu_{32}}{\mu_{33}})]\\
M_{21} &= -i(\frac{\beta\epsilon_{31}}{\epsilon_{33}} + \frac{\mu_{13}\beta}{\mu_{33}})\\
M_{22} &= -i(\frac{\beta\epsilon_{32}}{\epsilon_{33}} + \frac{\mu_{13}\alpha}{\mu_{33}})\\
M_{23} &= \frac{i}{\omega\epsilon_0}[\frac{\beta^2}{\epsilon_{33}} - k_0^2(\mu_{11} - \frac{\mu_{13}\mu_{31}}{\mu_{33}})]\\
M_{24} &= \frac{i}{\omega\epsilon_0}[\frac{-\alpha\beta}{\epsilon_{33}} - k_0^2(\mu_{12} - \frac{\mu_{13}\mu_{32}}{\mu_{33}})]\\
M_{31} &= \frac{i}{\omega\mu_0}[-\frac{\alpha\beta}{\mu_{33}} - k_0^2(\epsilon_{21} - \frac{\epsilon_{23}\epsilon_{31}}{\epsilon_{33}})]\\
M_{32} &= \frac{i}{\omega\mu_0}[\frac{\alpha^2}{\mu_{33}} - k_0^2(\epsilon_{22} - \frac{\epsilon_{23}\epsilon_{32}}{\epsilon_{33}})]\\
M_{33} &= -i(\frac{\alpha\mu_{31}}{\mu_{33}} + \frac{\epsilon_{23}\beta}{\epsilon_{33}})\\
M_{34} &= -i(\frac{\alpha\mu_{32}}{\mu_{33}} - \frac{\epsilon_{23}\alpha}{\epsilon_{33}})\\
M_{41} &= \frac{i}{\omega\mu_0}[-\frac{\beta^2}{\mu_{33}} + k_0^2(\epsilon_{11} - \frac{\epsilon_{13}\epsilon_{31}}{\epsilon_{33}})]\\
M_{42} &= \frac{i}{\omega\mu_0}[\frac{\alpha\beta}{\mu_{33}} + k_0^2(\epsilon_{12} - \frac{\epsilon_{13}\epsilon_{31}}{\epsilon_{33}})]\\
M_{43} &= -i(\frac{\beta\mu_{31}}{\mu_{33}} - \frac{\epsilon_{13}\beta}{\epsilon_{33}})\\
M_{44} &= -i(\frac{\beta\mu_{32}}{\mu_{33}} + \frac{\epsilon_{13}\alpha}{\epsilon_{33}})
\end{aligned} \tag{2.18}$$

These expressions are valid for the most general anisotropic case outside of the grating slice, and then the diffraction problem is reduced to a boundary-value problem.

In the case of E-O material studied in the thesis, we consider the permeability to be equal to μ_0, without magnetic effects. So in this case, the matrix M can be written as:

$$M = \begin{bmatrix} -\alpha\frac{\epsilon_{31}}{\epsilon_{33}} & -\alpha\frac{\epsilon_{32}}{\epsilon_{33}} & \frac{\alpha\beta}{\omega\epsilon_0\epsilon_{33}} & \omega\mu_0 - \frac{\alpha^2}{\omega\epsilon_0\epsilon_{33}} \\ -\beta\frac{\epsilon_{31}}{\epsilon_{33}} & -\beta\frac{\epsilon_{32}}{\epsilon_{33}} & -\omega\mu_0 + \frac{\beta^2}{\omega\epsilon_0\epsilon_{33}} & -\frac{\beta\alpha}{\omega\epsilon_0\epsilon_{33}} \\ \frac{-\alpha\beta}{\omega\mu_0} - \omega\epsilon_0(\epsilon_{21} - \frac{\epsilon_{23}\epsilon_{31}}{\epsilon_{33}}) & \frac{\alpha^2}{\omega\mu_0} - \omega\epsilon_0(\epsilon_{22} - \frac{\epsilon_{23}\epsilon_{32}}{\epsilon_{33}}) & \frac{\beta\epsilon_{23}}{\epsilon_{33}} & \frac{\alpha\epsilon_{23}}{\epsilon_{33}} \\ \frac{-\beta^2}{\omega\mu_0} + \omega\epsilon_0(\epsilon_{11} - \frac{\epsilon_{13}\epsilon_{31}}{\epsilon_{33}}) & \frac{\alpha\beta}{\omega\mu_0} + \omega\epsilon_0(\epsilon_{12} - \frac{\epsilon_{13}\epsilon_{32}}{\epsilon_{33}}) & \frac{\beta\epsilon_{13}}{\epsilon_{33}} & \frac{-\beta\epsilon_{13}}{\epsilon_{33}} \end{bmatrix} \tag{2.19}$$

2.3.2.2 Homogenous Isotropic Layer

The homogenous isotropic layers such as the electrode, the buffer layer are the simplest case. In these layers, the permittivity can be complex but is kept constant scalar, $\epsilon = n^2$, and in most situations the permeability can be taken as $\mu = \mu_0$. Thus in this case, the matrix M can be written as:

$$M = \begin{bmatrix} 0 & 0 & \frac{\alpha\beta}{\omega\epsilon_0\epsilon} & \omega\mu_0 - \frac{\alpha^2}{\omega\epsilon_0\epsilon} \\ 0 & 0 & -\omega\mu_0 + \frac{\beta^2}{\omega\epsilon_0\epsilon} & -\frac{\beta\alpha}{\omega\epsilon_0\epsilon} \\ \frac{-\alpha\beta}{\omega\mu_0} & \frac{\alpha^2}{\omega\mu_0} - \omega\epsilon_0\epsilon & 0 & 0 \\ \frac{-\beta^2}{\omega\mu_0} + \omega\epsilon_0\epsilon & \frac{\alpha\beta}{\omega\mu_0} + \omega\epsilon_0 & 0 & 0 \end{bmatrix} \tag{2.20}$$

2.3.2.3 Isotropic Material Grating

In the case of a grating, as already explained, some cautions have to be taken when factorizing the product of the permittivity and electric field. We do not detail here the calculations which can be found in reference[43]. The system of equations can be set in a form similar to Eq. 2.17 but where **M** contains the Fourier transform of the permittivity:

$$M = \begin{bmatrix} 0 & 0 & \alpha[[\epsilon]]^{-1}\beta & k_0^2 - \alpha[[\epsilon]]^{-1}\alpha \\ 0 & 0 & \beta[[\epsilon]]^{-1}\beta - k_0^2 & -\beta[[\epsilon]]^{-1}\alpha \\ \alpha\beta & \alpha^2 - k_0^2\lceil\lfloor\epsilon\rfloor\rceil & 0 & 0 \\ k_0^2\lfloor\lceil\epsilon\rceil\rfloor - \beta^2 & \alpha\beta & 0 & 0, \end{bmatrix} \tag{2.21}$$

where we have introduced a notation $[[.]]$ for the coefficients of the usual 2D Fourier transform of ϵ, as defined by Eq.2.1:

$$[[\epsilon]]_{mn,jl} = \epsilon_{m-j,n-l}, \tag{2.22}$$

then two notations $\lceil . \rceil, \lfloor . \rfloor$ defined by

$$\lceil\epsilon\rceil_{mn} = \frac{1}{D_x}\int_0^{D_x} \epsilon(x,y)\exp[-i(m-n)K_x x]dx, \tag{2.23}$$

$$\lfloor\epsilon\rfloor_{mn} = \frac{1}{D_y}\int_0^{D_y} \epsilon(x,y)\exp[-i(m-n)K_y y]dy, \tag{2.24}$$

and at last two notations $\lfloor\lceil.\rceil\rfloor$ and $\lceil\lfloor.\rfloor\rceil$ defined by

$$\lfloor\lceil\epsilon\rceil\rfloor_{mn,jl} = \frac{1}{D_y}\int_0^{D_y}\{\lceil 1/\epsilon\rceil^{-1}\}\times exp[-i(n-l)K_y y]dy^2, \tag{2.25}$$

$$\lceil\lfloor\epsilon\rfloor\rceil_{mn,jl} = \frac{1}{D_x}\int_0^{D_x}\{\lfloor 1/\epsilon\rfloor^{-1}\}\times exp[-i(m-j)K_x x]dx^2, \tag{2.26}$$

2.3.3 Eigenvalue Problem

We already have done the operation of elimination of the field components $[\mathbf{E}_z]$ and $[\mathbf{H}_z]$ in the previous subsection, so that Eq. 2.17 is transformed into an eigenvalue problem:

$$M\begin{pmatrix}\mathbf{E}_{xmn}\\ \mathbf{E}_{ymn}\\ \mathbf{H}_{xmn}\\ \mathbf{H}_{ymn}\end{pmatrix} = \gamma\begin{pmatrix}\mathbf{E}_{xmn}\\ \mathbf{E}_{ymn}\\ \mathbf{H}_{xmn}\\ \mathbf{H}_{ymn}\end{pmatrix}, \tag{2.27}$$

where γ is the eigenvalue of Eq. 2.27, and each of $(\mathbf{E}_x, \mathbf{E}_y, \mathbf{H}_x, \mathbf{H}_y)$ is represented as a column vector of the corresponding Fourier coefficients. Each of these solutions of Eq. 2.27 is considered as a mode that propagates in z-direction, thus the adjective " modal " in the name of the method.

During the programming, we set the truncation orders of the Fourier series with respect to x and y as $N_x = 2n_x + 1$ and $N_y = 2n_y + 1$ respectively, where n_x and n_y stand for the lower and upper limits of the sums in the truncated series, so that M is a $4N_xN_y \times 4N_xN_y$ matrix. All of the eigenvalues of M are divided into two sets according to the rule: eigenvalues with positive imaginary parts are put in set Σ^+, eigenvalues with negative imaginary parts are put in set Σ^-, the real eigenvalues are distributed between Σ^+ and Σ^- according to the sign of their real part. The eigenvalues belonging to sets Σ^+ and Σ^- are denoted by γ_l^+ and γ_l^- respectively, where l runs from 1 to $2N_xN_y$.

Thus the Fourier coefficients of the field within the region D^c can be written as:

$$\begin{pmatrix}\mathbf{E}_{xmn}\\ \mathbf{E}_{ymn}\\ \mathbf{H}_{xmn}\\ \mathbf{H}_{ymn}\end{pmatrix} = \begin{pmatrix}W^+_{mnl} & W^-_{mnl}\end{pmatrix}\begin{pmatrix}e^{i\gamma^+ z} & 0\\ 0 & e^{i\gamma^- z}\end{pmatrix}\begin{pmatrix}\mathbf{U}_l\\ \mathbf{D}_l\end{pmatrix}, \tag{2.28}$$

where $\mathbf{E}_{xmn}$ is $N_xN_y \times 1$ column vector, the same is valid for the other three vectors at the left, $W^{\pm}_{mnl}$ are $4N_xN_y \times 2N_xN_y$ matrices containing the the eigenvectors of Eq. 2.27. The propagating factors containing complex exponentials of the eigenvalues with positive or negative imaginary parts are organized in two diagonal $2N_xN_y \times 2N_xN_y$ matrices respectively. $\mathbf{U}_l$ and $\mathbf{D}_l$ are unknown modal field amplitudes at z = 0 in the form of $2N_xN_y \times 1$ column vectors.

2.4 Propagation Algorithm

In order to determine the modal field amplitudes $\mathbf{U}$ and $\mathbf{D}$, we need the help of a propagation algorithm that avoids the growing exponential terms, as already mentioned above. In this section, we will demonstrate how to pass from the transfer matrix algorithm to the scattering matrix algorithm in succession.

2.4.1 T - Matrix Algorithm

During the grating modeling, a stack of successive layers is always studied by a separate analysis in each layer. At the interface between two consecutive layers, the conditions of continuity of the tangential components of the electric and magnetic fields result in a matrix equation that binds the complex amplitudes of the fields on both sides of the interface. The amplitudes of the different orders in transmission and reflection for the whole grating structure can be obtained by multiplying the transfer matrices of the different layers. This direct approach is so called " T - matrix " algorithm.

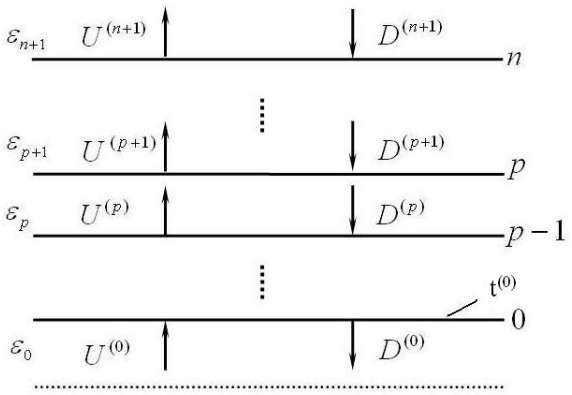

Figure 2.2 : *Schematic representation and notations used for propagation of the modes in a grating structure.*

Figure 2.2 is a schematic presentation of a layered grating stack, the field in each layer has been represented as upward or downward propagating and decaying waves. The notations U and D are column vectors whose elements represent the up- and down-going wave amplitudes. Thus the grating problem was divided into two separate problems: the eigenmode problem and the problem of determining the mode amplitudes. According to the continuity conditions at the interface $z = z_p$, between the layer p and $p-1$, we obtain the following equation:

$$\mathbf{W}^{(p+1)} \begin{bmatrix} \mathbf{U}^{(p+1)}(y_p+0) \\ \mathbf{D}^{(p+1)}(y_p+0) \end{bmatrix} = \mathbf{W}^{(p)} \begin{bmatrix} \mathbf{U}^{(p)}(y_p-0) \\ \mathbf{D}^{(p)}(y_p-0) \end{bmatrix} \quad , \tag{2.29}$$

where matrix $\mathbf{W}$ contains the eigenvectors of the Eq. 2.27. The propagation between two successive interfaces can be described by the transfer matrix:

$$\begin{bmatrix} \mathbf{U}^{(p)}(y_p-0) \\ \mathbf{D}^{(p)}(y_p-0) \end{bmatrix} = \phi^{(p)} \begin{bmatrix} \mathbf{U}^{(p)}(y_{p-1}+0) \\ \mathbf{D}^{(p)}(y_{p-1}+0) \end{bmatrix} \quad , \tag{2.30}$$

where $\phi^{(p)} = \begin{bmatrix} \exp(i\gamma_m^{(p)+} h_p) & 0 \\ 0 & \exp(i\gamma_m^{(p)-} h_p) \end{bmatrix}$ and the exponential functions are the components of diagonal matrices. It is necessary to mention that all eigenvalues with positive or negative imaginary parts are separated equally into two set Σ^+ and Σ^-. And also $h_p = z_p - z_{p-1}$ stands for the thickness of the p^{th} layer.

From the Eq. 2.29 and 2.30 we can get the relationship between the field amplitudes in the two layers, written in following form:

$$\begin{bmatrix} \mathbf{U}^{(p+1)}(y_p+0) \\ \mathbf{D}^{(p+1)}(y_p+0) \end{bmatrix} = (\mathbf{W}^{(p+1)})^{-1} \mathbf{W}^{(p)} \phi^{(p)} \begin{bmatrix} \mathbf{U}^{(p)}(y_{p-1}+0) \\ \mathbf{D}^{(p)}(y_{p-1}+0) \end{bmatrix} \tag{2.31}$$

We can note that $\mathbf{t}^{(p)} = (\mathbf{W}^{(p+1)})^{-1}\mathbf{W}^{(p)}$ represents the interface transfer matrix $\mathbf{t}^{(p)}$ between layer p and $p+1$. Meanwhile, the matrix $\mathbf{t}^{(p)}\phi^{(p)}$ represents the layer transfer matrix across the p^{th} layer.

So if we consider the grating structure with the n layers, we can establish a relationship between the fields on both sides of the grating by a transfer matrix written as:

$$\begin{bmatrix}\mathbf{U}^{(n+1)}\\ \mathbf{D}^{(n+1)}\end{bmatrix} = \prod_{i=1}^{n}\mathbf{t}^{(i)}\phi^{(i)}\mathbf{t}^{(0)}\begin{bmatrix}\mathbf{U}^{(0)}\\ \mathbf{D}^{(0)}\end{bmatrix} \tag{2.32}$$

However this algorithm has a serious defect, when the layer thickness or the number of layers increases, and due to the growing exponentials, the product of these sub-matrices $\mathbf{t}^{(i)}\phi^{(i)}$ can lead to significant numerical errors[42]. The cause of them[45,46] is the loss of significant digits when handling exponential functions which describe the propagation of different modes within the grating. To solve this numerical problem, the " Scattering-matrix propagation " (" S - matrix ") algorithm has been introduced[40,47].

2.4.2 Introduction and Definition of the S - Matrix

The S - matrix algorithm permits to avoid the loss of the significant digits during the calculations. For a certain grating stack of n layers, a matrix $\mathbf{S}$ can be constructed to link the amplitudes of the field in the layer $p+1$ and in the incident medium 0. It needs to be emphasized that $\mathbf{S}^{(p)}$ stands for the matrix of stack with p slices as marked in Fig. 2.2, and not only the matrix of the p^{th} slice in the stack. For a stack of p layers shown in Fig. 2.3, the scattering matrix of this stack can be written as:

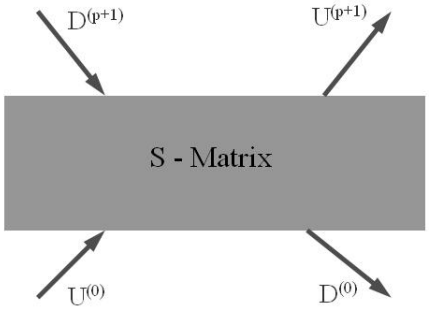

Figure 2.3 : *The scattering matrix of a p layers stack.*

$$\begin{bmatrix}\mathbf{U}^{(p+1)}\\ \mathbf{D}^{(0)}\end{bmatrix} = \mathbf{S}^{(p)}\begin{bmatrix}\mathbf{U}^{(0)}\\ \mathbf{D}^{(p+1)}\end{bmatrix} \tag{2.33}$$

It must also be divided into a 2×2 blocks matrix as Eq. 2.34 shown:

$$\mathbf{S}^{(p)} = \begin{bmatrix}\mathbf{T}_{uu}^{(p)} & \mathbf{R}_{ud}^{(p)}\\ \mathbf{R}_{du}^{(p)} & \mathbf{T}_{dd}^{(p)}\end{bmatrix} \quad , \tag{2.34}$$

this block form of $\mathbf{S}$ matrix operates with two inputs and generates two outputs in the layer 0 and $(p+1)$. For example, sub-matrices $\mathbf{T}_{dd}^{(p)}$ is a transmission part, which gives the

amplitude of the orders transmitted downwards in layer 0, and generated by an incident wave in the layer $(p+1)^{th}$ from above and penetrating through the first p layers, while $\mathbf{R}_{ud}^{(p)}$ means the reflection matrix, which gives the amplitudes of the waves propagating upwards in the medium $(p+1)$ and generated by the incident wave propagating downwards in layer $(p+1)$.

We will present out the construction of the matrix $\mathbf{S}^{(p)}$ in the next subsection and in Appendix 1.

2.4.3 Construction of the S-Matrix

By assuming the simpler case that there is no upward incidence in the medium 0 as in the Fig. 2.4, we can find two sub-matrices of **S** - matrix.

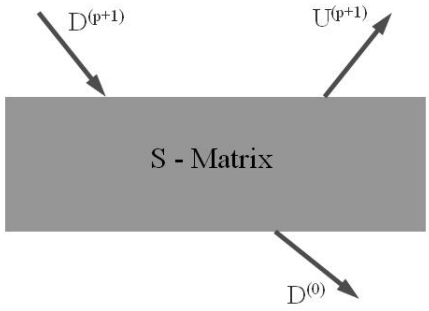

Figure 2.4 : *A simple case of scattering matrix for p layers stack.*

If $\mathbf{U}^{(0)}$ is null, then from Eq. 2.34 it is easy to get:

$$\begin{aligned} \mathbf{U}^{(p+1)} &= \mathbf{R}_{ud}^{(p)}\mathbf{D}^{(p+1)} \\ \mathbf{D}^{(0)} &= \mathbf{T}_{dd}^{(p)}\mathbf{D}^{(p+1)}. \end{aligned} \tag{2.35}$$

The detailed derivation of the $\mathbf{R}_{ud}^{(p)}$ and $\mathbf{T}_{dd}^{(p)}$ is given in Appendix 1[40,47]. We have:

$$\begin{aligned} \mathbf{R}_{ud}^{(p)} &= [\mathbf{t}_{11}^{(p)}\Omega^{(p)} + \mathbf{t}_{12}^{(p)}][\mathbf{t}_{21}^{(p)}\Omega^{(p)} + \mathbf{t}_{22}^{(p)}]^{-1} \\ \mathbf{T}_{dd}^{(p)} &= \mathbf{t}_{11}^{(p-1)}[\phi_{-}^{(p)}]^{-1}(\mathbf{t}_{21}^{(p)}\Omega^{(p)} + \mathbf{t}_{22}^{(p)}) \end{aligned} \tag{2.36}$$

where $\phi_{+}^{(p)}$ and $\phi_{-}^{(p)}$ are the two set of exponential functions matrix $\phi^{(p)}$ that we have introduced before, and $\Omega^{(p)} = \phi_{+}^{(p)}\mathbf{R}_{ud}^{(p-1)}[\phi_{-}^{(p)}]^{-1}$ is introduced in order to simplify the equation.

The remaining two blocks $\mathbf{R}_{du}^{(p)}$ and $\mathbf{T}_{uu}^{(p)}$ can be obtained similarly by considering no incident wave in the medium $p+1^{th}$ and an incident wave in the medium 0:

$$\begin{aligned} \mathbf{T}_{uu}^{(p)} &= [\mathbf{t}_{11}^{(p)} - \mathbf{R}_{ud}^{(p)}\mathbf{t}_{21}^{(p)}]\phi_{+}^{(p)}\mathbf{T}_{uu}^{(p-1)} \\ \mathbf{R}_{du}^{(p)} &= \mathbf{R}_{du}^{(p-1)} - \mathbf{T}_{dd}^{(p)}\mathbf{t}_{21}^{(p)}\phi_{+}^{(p)}\mathbf{T}_{uu}^{(p-1)}. \end{aligned} \tag{2.37}$$

2.5 Calculation of the Diffracted Field and Efficiencies

In this part, we want to describe several functions of the program, which mainly refer to the diffraction efficiency calculation.

2.5.1 Notations

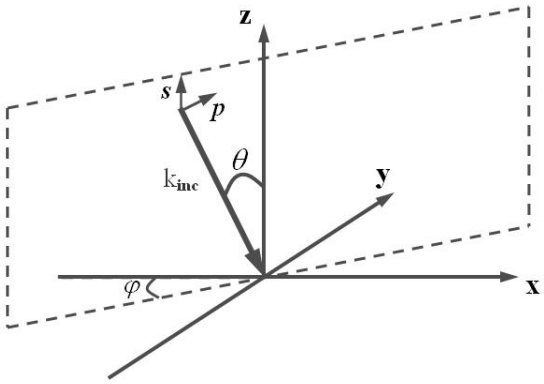

Figure 2.5 : *Notations of coordinate system and incidence wave used for efficiency calculation.*

First, when the coordinate system is set as shown in Fig. 2.5, the incident wave vector, normalized with respect to the wavevector in vacuum k_0, can be written naturally as:

$$\widehat{k}_i = (\widetilde{\alpha}_0, \widetilde{\beta}_0, -\widetilde{\gamma}_0) \quad , \tag{2.38}$$

where $\widetilde{\alpha}_0$, $\widetilde{\beta}_0$, $\widetilde{\gamma}_0$ are the components of the incident wave vector along x, y, z direction respectively, normalized by k_0. Second, we choose an unity vector $\widehat{e}_s$ (Eq. 2.22) that is perpendicular to $\widehat{k}_i$ and the z-axis, and corresponds to an incidence with polarization s, which means that the electric field vector is perpendicular to the plane of incidence.

$$\widehat{e}_s = \frac{1}{\sqrt{\widetilde{\alpha}_0^2 + \widetilde{\beta}_0^2}}(-\widetilde{\beta}_0, \widetilde{\alpha}_0, 0) \tag{2.39}$$

Third, these two vectors, accompanied by another unity vector $\widehat{e}_p$ which corresponds to the direction of p polarization, compose an orthogonal triad. The components of $\widehat{e}_p$ can be found by calculating the cross product of vector $\widehat{k}_i$ and $\widehat{e}_s$:

$$\widehat{e}_p = \widehat{k}_i \times \widehat{e}_s = \frac{1}{\sqrt{\widetilde{\alpha}_0^2 + \widetilde{\beta}_0^2}}(\widetilde{\alpha}_0\widetilde{\gamma}_0, \widetilde{\beta}_0\widetilde{\gamma}_0, \widetilde{\alpha}_0^2 + \widetilde{\beta}_0^2) \tag{2.40}$$

2.5.2 Incident Field Representation

In the cladding D^a, we assume that we have a single incident plane wave $\mathbf{F}_I$, which has only two non-zero elements in the Fourier space of $2N_xN_y$ dimensions. At the same time, because we want to analyze simultaneously the incidence with two different polarizations, the vector $\mathbf{F}_I$ takes two different forms, $\mathbf{F}_I^{(s)}$ and $\mathbf{F}_I^{(p)}$, which stand for incidence with s and p polarization, respectively:

$$\mathbf{F}_I^{(s)} = \begin{pmatrix} \vdots \\ \mathbf{E}_{00,x}^{(s)} \\ \vdots \\ \vdots \\ \mathbf{E}_{00,y}^{(s)} \\ \vdots \end{pmatrix}, \qquad \mathbf{F}_I^{(p)} = \begin{pmatrix} \vdots \\ \mathbf{E}_{00,x}^{(p)} \\ \vdots \\ \vdots \\ \mathbf{E}_{00,y}^{(p)} \\ \vdots \end{pmatrix}. \tag{2.41}$$

Here, $\mathbf{E}_{00,x}$ and $\mathbf{E}_{00,y}$ are the amplitudes of the incident electric field $\mathbf{E}_x$ and $\mathbf{E}_y$, and their positions in the vector are numbered $2n_xn_y+(n_x+n_y+1)$ and $2n_xn_y+(n_x+n_y+1)+N_xN_y$, respectively.

2.5.3 Representation of Reflected and Transmitted Fields

Similar to the presentation of the incident field, we can also denote the reflected field $\mathbf{F}_R$ and transmitted field $\mathbf{F}_T$ at the top or bottom of the grating stack as:

$$\mathbf{F}_R = \begin{pmatrix} \mathbf{E}_{-N_xN_y,x} \\ \vdots \\ \mathbf{E}_{mn,x} \\ \vdots \\ \vdots \\ \mathbf{E}_{mn,y} \\ \vdots \\ \mathbf{E}_{N_xN_y,y} \end{pmatrix}, \qquad \mathbf{F}_T = \begin{pmatrix} \mathbf{E}_{-N_xN_y,x} \\ \vdots \\ \mathbf{E}_{mn,x} \\ \vdots \\ \vdots \\ \mathbf{E}_{mn,y} \\ \vdots \\ \mathbf{E}_{N_xN_y,y} \end{pmatrix}. \tag{2.42}$$

The matrix S gives the link between the incident and the diffracted amplitudes:

$$\mathbf{F}_R = \mathbf{R}_{ud}\mathbf{F}_I, \qquad \mathbf{F}_T = \mathbf{T}_{dd}\mathbf{F}_I. \tag{2.43}$$

There also exist two solutions for the reflected and transmitted field, each corresponding to s and p polarizations obtained with the two incident fields as given in the previous subsection. It should be stressed that the two solutions are obtained using the same S-matrix submatrices. The remaining z-components of the field can be calculated according to the Maxwell equations using the values of the other two components $\mathbf{E}_x$ and $\mathbf{E}_y$, as discussed in the next subsection.

2.5.4 Efficiency Calculation

As usually, the diffraction efficiency is defined as the energy flux in direction perpendicular to the grating plane carried away by the corresponding diffraction order, divided by the same quantity of the incident wave, i.e. as the ratio of the z-components of the Poynting vectors of the diffracted and incident waves. Because of the anisotropic layer, the incidence wave with linear polarization can generate both TE and TM modes in the guiding-wave layer. For this reason, we calculate and present in the next chapters four different efficiencies R_{ss}, R_{sp}, R_{ps}, R_{pp} instead of only one total reflection efficiency R_{total}.

These four variables refer to:
-R_{ss} means the ratio of s polarized reflection energy and the incidence energy with s polarization;
-R_{sp} means the ratio of p polarized reflection energy and the incidence energy with s polarization;
-R_{ps} means the ratio of s polarized reflection energy and the incidence energy with p polarization;
-R_{pp} means the ratio of p polarized reflection energy and the incidence energy with p polarization.

If the electric field amplitude of the incidence wave vector $\widehat{\mathbf{E}}_{inc}$ equals to 1, then its components for an arbitrary linearly polarized wave can be rewritten in the xyz coordinate system as:

$$\begin{aligned}
\widehat{\mathbf{E}}_{inc} &= \cos\psi\widehat{e}_s + \sin\psi\widehat{e}_p = (E_x, E_y, E_z) \\
E_x &= \frac{1}{k_0\sqrt{\alpha_0^2+\beta_0^2}}(-k_0\beta_0\cos\psi + \alpha_0\gamma_0\sin\psi) \\
E_y &= \frac{1}{k_0\sqrt{\alpha_0^2+\beta_0^2}}(k_0\alpha_0\cos\psi + \beta_0\gamma_0\sin\psi) \\
E_z &= \frac{1}{k_0\sqrt{\alpha_0^2+\beta_0^2}}((\alpha_0^2+\beta_0^2)\sin\psi)
\end{aligned} \tag{2.44}$$

The magnetic field vector can be found for each order with wave vector $\mathbf{k}$ by:

$$\mathbf{H} = \frac{1}{\omega\mu}\mathbf{k}\wedge\mathbf{E} \tag{2.45}$$

- For the incident wave, ($k_z = -|\gamma| < 0$), the magnetic field x and y components are expressed, respectively:

$$\begin{aligned}
H_x &= \frac{1}{\omega\mu}(\beta E_z + |\gamma| E_y) \\
H_y &= \frac{1}{\omega\mu}(-|\gamma| E_x - \alpha E_z)
\end{aligned} \tag{2.46}$$

  and then Poynting vector z component equals to:

$$P_{inc} = \frac{1}{2}Re(E_x\overline{H}_y - E_y\overline{H}_x)$$

- For the reflected field component, ($k_z = |\gamma| > 0$), so that the x and y components of magnetic field vector and the z component of the electric field can be expressed as:

$$\begin{aligned}
E_z^+ &= -\frac{1}{|\gamma|}(\alpha E_x^+ + \beta E_y^+) \\
H_x^+ &= \frac{1}{\omega\mu}(\beta E_z^+ - |\gamma| E_y^+) \\
H_y^+ &= \frac{1}{\omega\mu}(|\gamma| E_x^+ - \alpha E_z^+)
\end{aligned} \tag{2.47}$$

and then the Poynting vector in z direction can be expressed as:

$$P_{ref} = \frac{1}{2} Re(E_x^+ \overline{H_y^+} - E_y^+ \overline{H_x^+}) \tag{2.48}$$

The total reflected efficiency is then obtained by:

$$R = \frac{P_{ref}}{P_{inc}} \tag{2.49}$$

- For the part in transmission, ($k_z = -|\gamma| < 0$), the x and y components of magnetic field vector and the z component of the electric field can be expressed as:

$$\begin{aligned} E_z &= \frac{1}{|\gamma|}(\alpha E_x + \beta E_y) \\ H_x &= \frac{1}{\omega\mu}(\beta E_z + |\gamma| E_y) \\ H_y &= \frac{1}{\omega\mu}(-|\gamma| E_x - \alpha E_z) \end{aligned} \tag{2.50}$$

then the Poynting vector in z direction and transmitted efficiency can also be obtained in the same way as in reflection.

When we are interested in the polarization states of the propagative order and, in particular, in the conversion of polarization, it is necessary to separate both the incident and the diffracted electric fields into two orthogonal polarizations s and p with respect to the plane containing the direction of propagation and the (Oz) axis:

$$\begin{aligned} \mathbf{E}_s &= (\widehat{e}_s.\mathbf{E})\widehat{e}_s, \\ \mathbf{E}_p &= \mathbf{E} - \mathbf{E}_s. \end{aligned} \tag{2.51}$$

Note that the same vector $\widehat{e}_s$ can be used to describe the s polarized field for the incident, reflected or transmitted wave.

The s and p components of the magnetic field vector can be found for each order with wave vector $\mathbf{k}$:

$$\begin{aligned} \mathbf{H}_s &= \frac{1}{\omega\mu}\mathbf{k} \wedge \mathbf{E}_s \quad , \\ \mathbf{H}_p &= \frac{1}{\omega\mu}\mathbf{k} \wedge \mathbf{E}_p \quad . \end{aligned} \tag{2.52}$$

Then the Poynting vector z component can be separated in two parts corresponding to the s and p polarizations:

$$\begin{aligned} P &= P_p + P_s \\ P_s &= -\frac{1}{2} Re(E_s \overline{H}_s) \\ P_p &= \frac{1}{2} Re(E_p \overline{H}_p) \end{aligned} \tag{2.53}$$

The reflective efficiency can be calculated:

$$R_{ss} = \frac{P_{s,ref}}{P_{s,inc}}, \quad R_{sp} = \frac{P_{p,ref}}{P_{s,inc}}$$
$$R_{ps} = \frac{P_{s,ref}}{P_{p,inc}}, \quad R_{pp} = \frac{P_{p,ref}}{P_{p,inc}} \tag{2.54}$$

2.6 Validation of the Numerical Code

The results of the calculation for arbitrary anisotropic layer without the grating structure (denoted as SD in the table) have been compared with G. Tayeb's program (GT). The numerical experiment uses a "substrate + layer + superstrate " structure, having wavelength of the normally incident plane wave equal to 1550nm, with either s or p polarization. The permittivities for the results given in the Table were take as:

$$\epsilon^a = 1.44, \quad \epsilon^s = 1.69, \quad \epsilon^c = \begin{bmatrix} 2 & 0.25 & 0.15 \\ 0.25 & 4 & 0.35 \\ 0.15 & 0.35 & 3 \end{bmatrix}$$

Table 2.1 : *The comparison of the efficiency calculation.*

	R_{ss}	R_{sp}	T_{ss}	T_{sp}
GT	0.2993540737	0.10094275E-02	0.6445701967	0.550663020E-01
SD	0.29935407	0.100942725E-02	0.64457020	0.55066302E-01
	R_{ps}	R_{pp}	T_{ps}	T_{pp}
GT	0.35958481E-02	0.120529657E-01	0.9273450306	0.570061556E-01
SD	0.35958481E-02	0.12052966E-01	0.92734503	0.57006156E-01

We have also used different values of the permittivity tensor components and compared the efficiencies, the results always coincide, even with asymmetrical permittivity tensor, which gave gains or losses.

Other tests were performed against existing independent numerical codes in the case of isotropic media.

In the case of anisotropic layers and grating structures, modelized in the next chapters, we have made test for energy balance, convergence with respect to the truncation parameters, and tests for fulfillment of the requirements of the reciprocity theorem.

2.7 Conclusion

In this chapter, we have briefly explained the method for numerical modeling and also the process of program realization. The works in the following two chapters are mostly based on this numerical code, in which the Fourier Modal Method is used to calculate the distribution of electromagnetic field in both reflection and transmission, giving the possibility to calculate diffraction efficiencies in normal or oblique incidences and different polarizations. To analyze the performance of a given filter structure, we need this program to locate the center wavelength of resonant peak, to calculate the linewidth and the angular tolerance.

However, this program also has its limits: it can deal with a structure consisting of isotropic, anisotropic layers and isotropic grating but it does not give the possibility to model gratings structures fabricated inside the anisotropic material. The second limitation is that it is not made for structures with periodicity in two non-orthogonal directions.

Chapter 3

Guided Mode Resonant(GMR) Filters Based on Lithium Niobate

3.1 Introduction

Lithium Niobate ($LiNbO_3$) is a ferroelectric material suitable for a variety of applications[48,49]. Its excellent electro-optic, nonlinear, and piezoelectric properties has made of it one of the most thoroughly characterized and widely applied material[50]. For specific electro-optic applications, its large E-O coefficients and low half-wave voltage[51] are always utilized for optical modulation and Q-switching of infrared wavelengths.[52–54]

In this chapter, we present a theoretical study of the properties of a guided mode resonance (GMR) grating including a layer of $LiNbO_3$. The aimed application is narrow band tunable spectral filtering, thus we focus on the spectral tunability performances, but also on the behavior of the filter with respect to the polarization and angular divergence of the incident beam. The approach we used is the following: using the 2D "doubly periodic" grating structure in order to improve the angular acceptance of the filter; introducing a layer of electro-optic material $LiNbO_3$ as guiding layer (in which the field of the guided mode is maximum), in order to maximize the guided mode sensitivity to the changes of the permittivity tensor of $LiNbO_3$; using two layers of ITO as electrodes to apply external voltage. The structure is illuminated under normal incidence to ensure both polarization independence with respect to the incident field and optimized angular acceptance, at least when no voltage is applied.

When the external voltage is adjusted, it modifies the permittivity tensor of $LiNbO_3$ and thus the guided mode. This results, as desired, in a spectral shift of the resonant peak. However, some complementary questions arise: what spectral tunability magnitude can we get, what is the best configuration, does it break the polarization independence property, does it modify the angular acceptance?

First, we present the E-O characteristics of the $LiNbO_3$ and our choice of the orientation of the crystal with respect to the applied static electric field in order to maximize the change of the permittivity tensor ε_{LiNbO_3}; Second, the structure under study is presented in detail and the reason for choosing this specific design is explained; Then, the behavior of the resonance peak when a static voltage is applied is studied. The TE and TM guided mode resonance cases are compared. The important features such as spectral and angular widths, spectral tunability and modification of the peak with respect to the incident polarization are addressed in detail. Finally, some information concerning the manufacturing of the device is mentioned at the end of the chapter.

3.2 Electro-Optic Effect in $LiNbO_3$

In this part, we recall the electro-optic properties of $LiNbO_3$. We deduce from the values of the E-O coefficients of the $LiNbO_3$ the adequate orientation of the crystal with respect to the applied static electric field, and we study how the permittivity tensor ε_{LiNbO_3} is modified in this configuration.

3.2.1 Physical and Optical Properties of $LiNbO_3$

Lithium Niobate has a 3m point group-symetry (symetry axis is the c-axis), thus it is a uniaxial anisotropic crystal. Some of its physical properties are enumerated in table 3.1. We observe that $LiNbO_3$ has interesting properties that make it suitable for optoelectronic applications: its large transparent spectral range, from 450nm to 5200nm, which

covers from visible to infrared light; its high refractive index; and its low absorption coefficient. Many investigations[55,56] focused on its physical and mechanical properties have been continued for decades aimed to improve its properties for applications.

For our purpose, the interesting property is the strong E-O coefficients which are shown in the last row of table 3.1. Because $LiNbO_3$ is a crystal with a 3m point-group symmetry, only eight elements of the E-O tensors are non-null, with only four values. These elements are as follows[57]:

$$r_{12} = r_{61} = -r_{22}, \quad r_{33}, \quad r_{51} = r_{42}, \quad r_{13} = r_{23}. \tag{3.1}$$

Table 3.1 : *Physical properties of Lithium Niobate.*[58]

material $LiNbO_3$	
symmetry system	3m
transparency band(nm)	450 - 5200
absorption coefficient	0.1%/cm at 1064nm
refractive index	n_o=2.211, n_e=2.138 at 1550 nm n_o=2.322, n_e=2.156 at 1064 nm n_o=2.286, n_e=2.203 at 632.8 nm
Sellmerier equations λ in μm	$n_o^2(\lambda) = 4.9048 + 0.11768/(\lambda^2 - 0.04750) - 0.027169\lambda^2$ $n_e^2(\lambda) = 4.5820 + 0.09917/(\lambda^2 - 0.04443) - 0.021950\lambda^2$
E-O coefficients (pm/V)	r_{33}=30.8, r_{13}=8.6 r_{22}=3.4, r_{51}=28

According to the Sellmerier equations in table 3.1, we can calculate the refractive indexes values at upper and lower limit of the wavelength range $\lambda = [1400nm, 1700nm]$, and their deviation with respect to those at 1550nm:

- λ= 1400nm: n_o=2.2165, n_e=2.1426 deviation Δn_o= 2.5% , Δn_e=2.2%
- λ= 1700nm: n_o=2.2095, n_e=2.1366 deviation Δn_o= 2.1% , Δn_e=1.9%.

The effect of the dispersion of the reflective indexes can be neglected, during the simulation, we can always use the value at 1550nm.

3.2.2 Electro-optic Effect in $LiNbO_3$

In Chapter 1, we have recalled the useful tools to study the effect, on the permittivity tensor of an electo-optic material, when applying an external static electric field. Here, we apply this theory to the particular case of $LiNbO_3$.

When no voltage is applied, $LiNbO_3$ is a uniaxial crystal with optical c-axis chosen along z, whose extraordinary n_e and ordinary n_o refractive index are given in table 3.1. In the orthogonal (x, y, z) system (x and y are chosen freely in the plane perpendicular to $z = c$), its index ellipsoid writes as

$$(\frac{x^2 + y^2}{n_o^2} + \frac{z^2}{n_e^2}) = 1 \quad , \tag{3.2}$$

and is represented in figure 3.1.

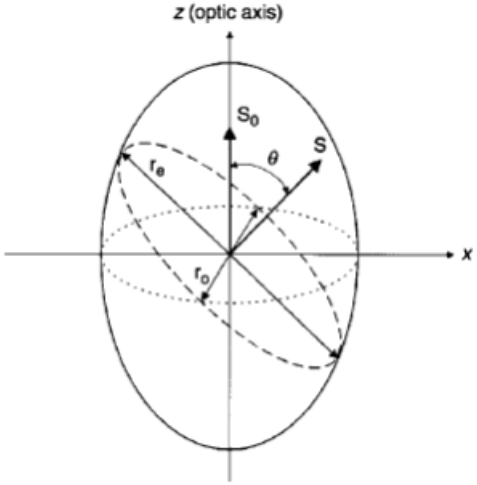

Figure 3.1 : *Refractive index ellipsoid of $LiNbO_3$.*

The optical axis Oz is a symmetry axis and in the xy plane the material behaves as an isotropic medium.

In our study, only the linear term of the E-O effect, corresponding to the Pockels effect, is taken into account. So, when an external electrical field $\vec{E} = (E_x, E_y, E_z)$ is applied on the layer of $LiNbO_3$, the index variation due to the E-O effect will be given by the following tensorial expression:

$$\begin{bmatrix} \Delta(\frac{1}{n^2})_1 \\ \Delta(\frac{1}{n^2})_2 \\ \cdot \\ \cdot \\ \cdot \\ \Delta(\frac{1}{n^2})_6 \end{bmatrix} = \begin{bmatrix} 0 & -r_{22} & r_{13} \\ 0 & r_{22} & r_{13} \\ 0 & 0 & r_{33} \\ 0 & r_{51} & 0 \\ r_{51} & 0 & 0 \\ -r_{22} & 0 & 0 \end{bmatrix} \begin{bmatrix} E_x \\ E_y \\ E_z \end{bmatrix} \quad , \tag{3.3}$$

where $\Delta(\frac{1}{n^2})_i$ is the variation of the i^{th} element of the inverse square of the index matrix, as introduced in Chapter 1. The expression of this matrix is:

$$(\frac{1}{\widetilde{n^2}}) = \begin{bmatrix} \frac{1}{n_x^2} + \Delta(\frac{1}{n^2})_1 & \Delta(\frac{1}{n^2})_6 & \Delta(\frac{1}{n^2})_5 \\ \Delta(\frac{1}{n^2})_6 & \frac{1}{n_y^2} + \Delta(\frac{1}{n^2})_2 & \Delta(\frac{1}{n^2})_4 \\ \Delta(\frac{1}{n^2})_5 & \Delta(\frac{1}{n^2})_4 & \frac{1}{n_z^2} + \Delta(\frac{1}{n^2})_3 \end{bmatrix} \quad , \tag{3.4}$$

and the index ellipsoid equation writes as:

$$\begin{aligned} (\frac{1}{n_o^2} - r_{22}E_y + r_{13}E_z)x^2 + (\frac{1}{n_o^2} + r_{22}E_y + r_{13}E_z)y^2 + (\frac{1}{n_e^2} + r_{33}E_z)z^2 \\ +2r_{51}E_y yz + 2r_{51}E_x zx - 2r_{22}E_x xy = 1. \end{aligned} \tag{3.5}$$

This equation is valid when a static electric field with components along x, y and z is applied. In the following, we will chose a particular direction for the static electric field, *a priori* the most convenient for our purpose.

3.2.3 Crystal Orientation and Variation of Permittivity

The question of the choice of the orientation of the crystal is not trivial. We have to consider the spectral tunability that can be achieved, the possibility to preserve the polarization independence property of the filter, and at last, the possibility to manufacture the structure. The second and third points will be treated in Sections 3.4 and 3.5. The orientation that will give the greatest tunability is not so obvious. Indeed, in general, the index ellipsoid changes in form and orientation when a static field is applied, and the consequence on the effective index of the guided modes that can propagate is not direct. We will illustrate this point in the chapter describing $BaTiO3$. Moreover, it would be necessary, in order to quantify the magnitude of the modification of the index ellipsoid, to introduce a scalar parameter, that is to say a figure of merit (FOM). This could be for example, as in reference[59], the optical index in the crystal proper axis that varies the most. Yet, this approach may be not suitable for our purpose (the guided mode propagation problem).

In the case of $LiNbO_3$, we can observe in table 3.1 that the greatest E-O coefficients is r_{33} which is involved if the static electric field is applied along the oz axis. Thus, intuitively, we think that the greatest tunability will be obtained if the static electric field is applied along z. The r_{51} coefficient, whose value is close to that of r_{33}, would be involved for a field applied along Oy or Ox. Yet, in this configuration, the material becomes anisotropic in the plane perpendicular to the axis along which the electric field is applied, which is not suitable for the polarization independence property of the filter, as it will be seen latter. Thus we turn the electro-optic crystal so that the direction that corresponds to the ordinary refractive index n_o is perpendicular to the static electric field and that of the extraordinary refractive index n_e is parallel to it, as illustrated in Fig. 3.2.

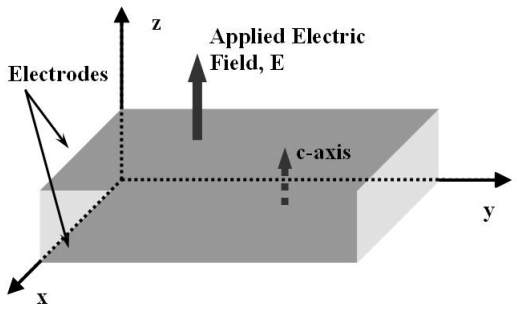

Figure 3.2 : *Arrangement of the crystal and the applied static electric field. The applied field* $\boldsymbol{E}$ *and the c-axis of the crystal are parallels.*

Two electrodes are used to apply the external field, the c-axis of $LiNbO_3$ and the static electric field direction are both along the z direction. When the electrical field $(0, 0, E_z)$ is applied, the largest E-O coefficient r_{33} is involved, together with r_{13}. Eq. 3.5 can be simplified into:

$$(\frac{1}{n_o^2} + r_{13}E_z)x^2 + (\frac{1}{n_o^2} + r_{13}E_z)y^2 + (\frac{1}{n_e^2} + r_{33}E_z)z^2 = 1. \tag{3.6}$$

From this equation it can be observed that the orientation of the index ellipsoids does not change, but the values of the ellipse's radii vary, the one along x remaining equals to the

one along y. Hence, $LiNbO_3$ under an electric field along z still keeps its uniaxial negative characteristic with optical axes along z, but with different refractive index values. The conservation of the isotropy in the xy plane is very interesting for our filtering application purpose, especially concerning the polarization independence property.

According to the relationship between the refractive index and the permittivity tensor, $[\varepsilon^{'}] = [n^{'2}]$, we can calculate the new permittivity $\varepsilon^{'}$. From the Eq. 3.6 we get:

$$[\frac{1}{n^{'2}}] = \begin{bmatrix} \frac{1}{n_o^2} + r_{13}E_z & 0 & 0 \\ 0 & \frac{1}{n_o^2} + r_{13}E_z & 0 \\ 0 & 0 & \frac{1}{n_e^2} + r_{33}E_z \end{bmatrix} , \tag{3.7}$$

then we inverse the matrix $[\frac{1}{n^{'2}}]$ and get the new permittivity ε_{LiNbO3}:

$$\varepsilon_{LiNbO3} = \begin{pmatrix} \frac{n_o^2}{1+r_{13}E_z n_o^2} & 0 & 0 \\ 0 & \frac{n_o^2}{1+r_{13}E_z n_o^2} & 0 \\ 0 & 0 & \frac{n_e^2}{1+r_{33}E_z n_e^2}. \end{pmatrix} \tag{3.8}$$

We find again that the crystal remains uniaxial with its optical axis along z. We show the variation of the permittivity tensor coefficients with respect to the applied voltage in Fig. 3.3:

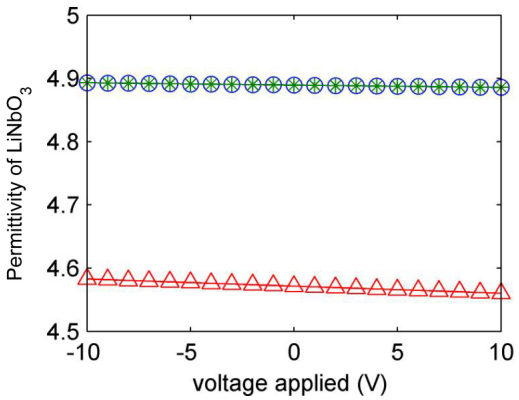

Figure 3.3 : *The change of the permittivity elements under the condition of external static electric field applied along z direction. Circle, star and triangle marks correspond to ε_{11}, ε_{22}, ε_{33} respectively.*

In this simulation, the thickness of $LiNbO_3$ layer is equal to 350nm, the external voltage varies from -10V to 10V, so the range of intensity of the static electric field is [-2.86, 2.86]$\times 10^7$ V/m, which is less than the breakdown limit of the material (see table 3.1).

We can find that the three coefficients decrease as the voltage increases. At the wavelength 1550nm, the permittivities ε_{11} and ε_{22} change from 4.8894 at 0V to 4.8835 at 10V, and ε_{33} changes from 4.5715 to 4.5532. The variation of ε_{33} is larger than that of ε_{11} and ε_{22} in the same condition of variation of V. This is due to the difference between the r_{33} and r_{13} coefficients.

As a conclusion, by now, we have presented the E-O effect in $LiNbO_3$ and the orientation we have chosen for the $LiNbO_3$ layer. Applying the external electrical field along

the z direction and orienting the $LiNbO_3$ layer to make its optical axis parallel to z involves the greatest E-O coefficient. Intuitively, we believe that this is the most convenient configuration for tunability. Moreover, in that case, the layer remains isotropic in the xy plane, which is important for the polarization independence property of the filter.

3.3 Design of the Structure

In the present Chapter, the aim is the study of the properties of a resonant grating filter including an E-O layer of $LiNbO_3$. For this study to be relevant for applications, we have chosen to work with a structure which presents the following properties:

1. A controllable narrow reflection band (resonant peak);
2. A maximal reflective efficiency for the center wavelength and a low sideband;
3. A large angular tolerance as compared to the divergence of a standard incident beam;
4. An independence with respect to the polarization of the incident wave.

We have designed a filter structure based on a two-dimensional grating on the top of a stack of dielectric layers including a layer of $LiNbO_3$. In this section, we will mainly introduce this filter structure from conception to constitution.

3.3.1 Composition of the structure

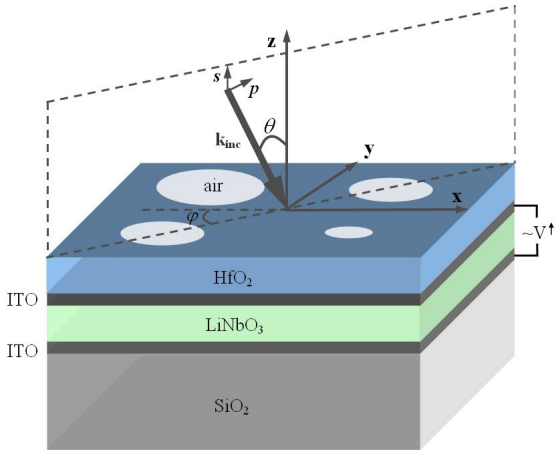

Figure 3.4 : *The schematic diagram of the optimized GMR filter's structure based on $LiNbO_3$.*

Table 3.2 : *Material's permittivity of each layer at 1550nm.*

Layer number	Material	Permittivity	Thickness
0 (substrata)	Silica	$\varepsilon_{SiO_2} = 2.082$	
1	ITO	$\varepsilon_{ITO} = 1.613$	50nm
2	$LiNbO_3$	$\varepsilon_{x,y} = 4.89$ $\varepsilon_z = 4.57$	-
3	ITO	$\varepsilon_{ITO} = 1.613$	50nm
4	$HfO2$	$\varepsilon_X = 3.24$	100nm
5	$HfO2$ and air	$\varepsilon_X = 3.24$ $\varepsilon_{air} = 1.00$	419.5nm
6(superstrata)	air	$\varepsilon_{air} = 1.00$	

As shown in Fig.3.4, the stack is composed of a silica substrate, a layer of E-O material $LiNbO_3$, which will be the guiding layer (its thickness depends on the configuration), and a grating etched in a HfO_2 layer. HfO_2 has been chosen for its low refraction index with respect to $LiNbO_3$, so that the guided mode can have its field maximum in the $LiNbO_3$ layer. Two layers of ITO (indium tin oxide) surrounding the $LiNbO_3$ layer will be used as electrodes to apply the external electrical field. The ITO is a well known conducting oxide material which presents advantages in both electrical conductivity and optical transparency. Meanwhile, it is also easy to be deposited as a thin film[60]. In the spectral region on which we focus, ITO presents a small absorption character (k=0.02 at 1550nm)[61]. In the following, we focus on studying the physical aspect of the resonance phenomenon in $LiNbO_3$ based GMR filter. Hence, for the sake of simplicity, we ignore, for this first study, the imaginary part of the index of ITO during the simulation. Latter in the section concerning the manufacture, we will explain what kind of deposition method allows to minimize the absorption coefficient of ITO.

The grating is 2D and illuminated under normal incidence, in order to obtain the polarization independence property, and the pattern is "doubly-periodic" to optimize the angular tolerance.

All the structures studied in the following have the same composition but with different parameters, which are all given in the Appendix-2.

In the next paragraph, we detail the rules we used to optimize the parameters of theses structures.

3.3.2 Rules for Tunable GMR Filter Designing

We first present a brief reminder of the link between the parameters of the structure and its optical properties, and the design rules that follow from it. Then, we emphasize the supplementary step brought in the design process by taking into account the E-O effect and the purpose of tunability.

Some of the filter properties can be deduced from the study of the equivalent homogeneous structure as defined in Chapter 1. The reflectivity outside resonance is given by the reflectivity of the equivalent homogeneous structure. Hence, in order to obtain a low sideband, the whole filter should be a stack that forms an antireflection structure. Here, the main layers are E-O material layer, 2D grating layer and isolating layer, so it can be considered as a three layers stack, where the two layers of ITO electrode have been neglected, because of its thin thickness. From the coupling condition, the position of the

peak depends linearly both on the effective index of the guided mode of the equivalent structure and on the grating period. As a consequence, modifying the stack will modify the center wavelength of the filter. However, it can also be shifted at the desired wavelength simply by changing the grating period while conserving the holes radii versus period ratio. One has in addition to keep in mind that in order to avoid energy losses, one diffraction order only (zero order) must be propagative in the substrate and superstrate. Hence, the grating period must be smaller than the incidence wavelength (sub-wavelength grating). The last two important features are the spectral bandwidth and the angular tolerance. They depend on the field of the guided mode that is excited, on the grating thickness and on the grating pattern.

From these rules, we can deduce a first set of parameters, and calculate the angular and spectral bandwidths of the structure. Then an iterative optimization process can begin:
(1). Optimization of the thickness of the grating in order to adjust the spectral bandwidth.
(2). Optimization of the pattern in order to maximize the angular bandwidth versus spectral bandwidth ratio.
(3). Optimization of the period; All the above steps modify the center wavelength of the filter. It can be re-adjusted by varying the grating period.

In addition to this procedure, because of the tunability requirement, a supplementary step has to be included in this optimization process. Indeed, the achievable tunability may depend on the profile of the guided mode field in the E-O layer. In the next paragraph, we study the influence of the guided mode order and the distance from cut-off on the tunability of the resonance peak. These features can be adjusted by changing the thickness of the $LiNbO_3$ layer, which requires repeating again the optimization procedure described herein.

3.3.3 Influence of the Profile of the Guided Mode Field

We start by studying the evolution of the guided modes of an equivalent planar structure (namely structure 3.1 in the Appendix 2) when the thickness of the $LiNbO_3$ varies. We plot on Fig. 3.5 the amplitude of the reflected electric field as a function of the thickness h of the $LiNbO_3$ layer and the normalized x-component of the in-plane wave vector. We observe several bright curves corresponding to modes of different orders and polarization excited in the structure. Note that as the structure is isotropic in the xy plane, the modes are either TE or TM.

It is obvious that when the $LiNbO_3$ layer thickness increases, the number of modes in the layer augments. The choice of the guided mode propagation constant $\widetilde{\alpha}_g$ (normalized with respect to the wavenumber in vacuum) and the thickness of the layer determine the profile of the mode field, and thus the properties of the resonance peak. In order to study the influence of the mode field profile, we take the TE mode as an example and choose four typical points which are indicated on Fig.3.5:
(1). point A, thin layer thickness (h = 0.15 μm, $\widetilde{\alpha}_g = 1.69$), first order mode;
(2). point B, moderate layer thickness (h = 0.35 μm, $\widetilde{\alpha}_g = 1.91$), first order mode;
(3). point C, thick layer thickness (h = 0.55 μm, $\widetilde{\alpha}_g = 2.02$), first order mode;
(4). point D, thick layer thickness (h = 0.55 μm, $\widetilde{\alpha}_g = 1.57$), second order mode.

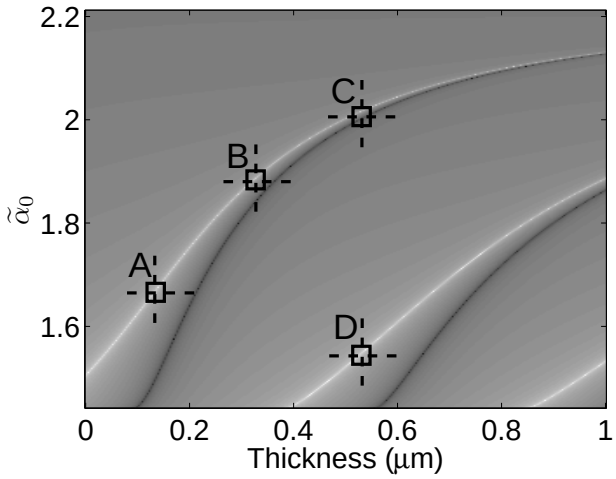

Figure 3.5 : *The reflected electric field with respect to the thickness of the $LiNbO_3$ layer and the normalized x-component of the in-plane wave vector.*

For these four situations, we firstly adjust the grating period to locate the resonant peaks at the same wavelength range, with the purpose of analyzing the effect of the mode field profile on the tunability under the same condition (the parameters are given in the Appendix 2, Fig. 5.3, 5.4, 5.5).

Fig. 3.6 shows the reflectivity spectrum for each working point, without and with a $1.4 \times 10^7 V/m$ applied electrical field. The tunabilities are 0.53nm, 0.81nm, 0.88nm and 0.56nm respectively for points A, B, C and D. Points A and D correspond to modes quite close to the cut-off. Their field may be less confined in the $LiNbO_3$ layer than modes B and C, which may explain their lower tunability. The fact that the tunability for point C is slightly greater than for point B supports this conclusion. The order of the mode seems not to be relevant since point A and D have quite the same tunability.

The best choice of the working point is finally made according to the total performance of the structure, taking into account the interaction imposed by the grating. From this point of view, the resonant peak property at point B is the best among these four points. Its peak width is the smallest ($\mathbf{Q} \simeq 15000$) and the tunability is larger than for points A and D. Point C holds these two similar characters as point B, but its sideband is obviously higher than point B, which it's not suitable for application. Thus for the study in the next section, we choose the structure which corresponds to the point B.

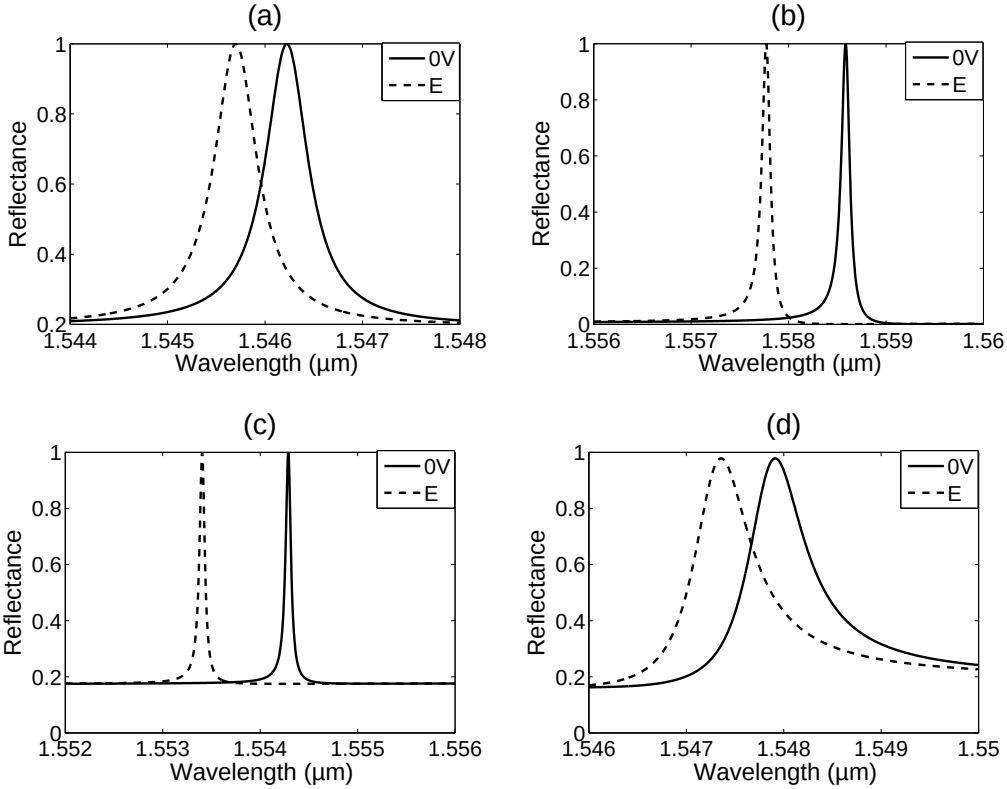

Figure 3.6 : *The comparison of resonance peak and tunability with different points in the mode profile.*

3.4 Detailed Study of the Tunability Properties of the Structure

The brief comparative study of the mode structure in the previous section allows us in this section to first study in detail the center wavelength shift with respect to the applied voltage. Then, we focus on the spectral shape with respect to the incident polarization, with and without voltage applied. Last, we study the reflectivity versus the angle of incidence for different planes of incidence. For these three points, we compare the TE mode and the TM mode that can be seen in Fig. 3.5 close to point B.

3.4.1 Tunability as a Function of the Applied Voltage

In this part, we want to discuss the relationship between the shift of the resonant peak and the applied voltage. From the previous discussion in chapter 1 we know that the shift of the resonant peak in the spectrum is basically due to the change of the permittivity tensor of the E-O material, which modifies the effective index of the mode. In Fig.3.7 we present the result of the resonant peak position changes for a TE and a TM mode. Figure 3.7(a) and (b) shows the reflectivity spectrum for the TE mode and TM mode, respectively, for several applied voltages from 0V to 20V, with a 5V step. As the thickness of the E-O layer is 0.35 μm, the maximal electric intensity is equal to $5.7 \times 10^7 V/m$, which is bellow the breakdown limit of the material. In Fig.3.7 (c) and (d) we have plotted the variation of

the center wavelength with respect to the applied voltage for the TE mode and TM mode, respectively.

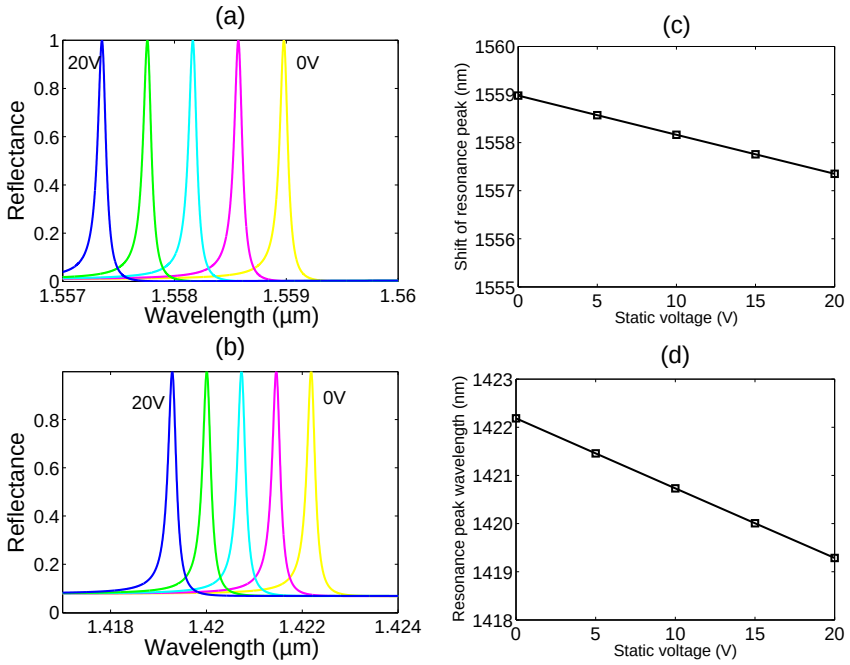

Figure 3.7 : *Resonant peak positions under different applied voltages for the TE mode (a) and the TM mode (b); center wavelength shift with respect to the applied voltage for the TE mode (c) and TM mode (d).*

It is easy to understand why the resonant peak wavelength for TE mode λ_{TE} is larger than that of TM mode. For a given filter structure and with the same condition of incidence, the normalized x-component of the mode propagation constant $\widetilde{\alpha}_{TE}$ for the TE mode is larger than $\widetilde{\alpha}_{TM}$ for the TM mode. According to the resonant condition $\lambda_{peak} = \frac{\widetilde{\alpha}}{D}$, where D is the grating period, a larger value of $\widetilde{\alpha}$ corresponds to a larger wavelength of resonant peak.

Fig. 3.7 shows that the resonance peak for both the TE and the TM mode shifts as the applied voltage increases, which means that the concept of tunable resonant grating works. When the external applied voltage changes from 0V to 20V, the peak of the TE mode shifts within 1.63 nm in the direction of the shorter wavelength, and the peak of the TM mode shifts within 2.9 nm in the same direction. This shift tendency can be explained by the permittivity variation as the voltage changes. Fig. 3.3 shows the change of the permittivity components with respect to the applied voltage. As the voltage augments, the three elements of the permittivity tensor ε decrease, which explain the shift of the peak towards shorter wavelengths (the effective index of the guided modes decreases). Moreover, the variation of ε_{33} is larger than that of ε_{11} and ε_{22}. For the TE mode, with field components (E_x, H_y, H_z), the only permittivity tensor element involved is ε_{11}, and for the TM mode, with field components (E_y, E_z, H_x), both of ε_{22} and ε_{33} are implied. As a consequence the shift of the TM mode resonant peak is larger than that of the TE mode. Last, we observe that for both TE and TM modes, the shift is linear with respect to V, which may be related to the linear dependency of the permittivity tensor coefficients for this variation range (see Fig. 3.3).

Meanwhile, these peaks also keep a low sideband level as the applied voltage changes, which is important for applications.

Now, we will focus on the properties of the spectral peak as a function of the polarization and applied voltage.

3.4.2 Spectral Peak Properties

Fig. 3.8 shows the peak in the reflectivity spectrum for both TE (Fig. 3.8(a), (b)) and TM (Fig. 3.8(c), (d)) mode of structure 3.3 (Fig. 5.4 in Appendix 2) illuminated by a normal incident wave with s (solid line) and p (circles) polarizations. The case for no voltage applied (Fig. 3.8(a), (c)) and 10V voltage applied (Fig.3.8(b), (d)) are presented.

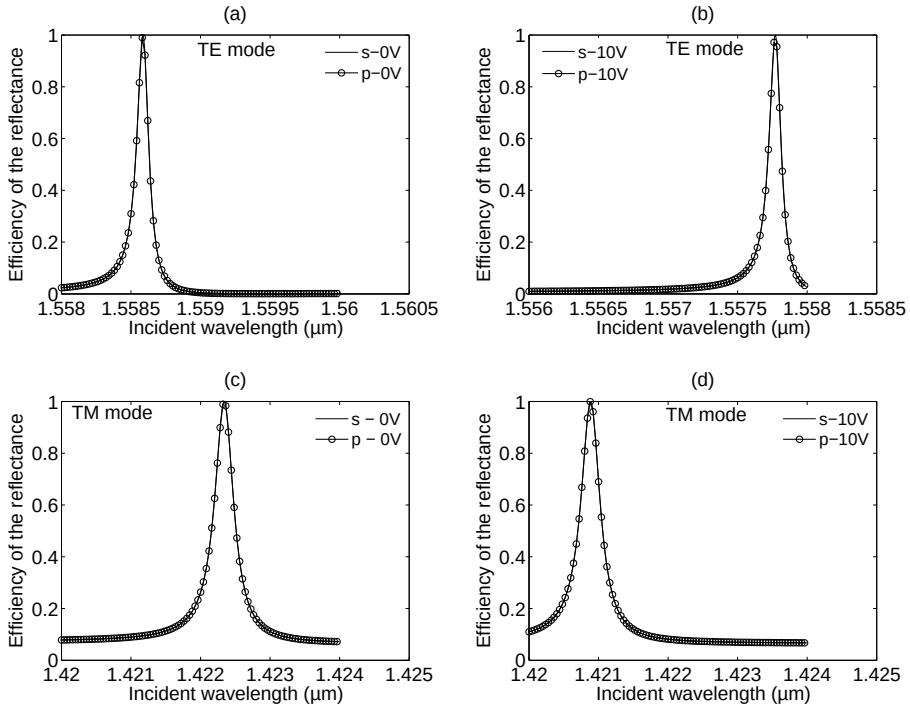

Figure 3.8 : *The filtering center wavelength and the linewidth of the resonance peak for structure 3.3 (Fig. 5.4). (a). TE mode resonant peak for normal incidence without applied voltage; (b). TE mode resonant peak for normal incidence with 10V applied voltage; (a). TM mode resonant peak for normal incidence without applied voltage; (b). TM mode resonant peak for normal incidence with 10V applied voltage.*

We can read from the figure that: for the TE mode, the filter central wavelength λ_{TE} = 1558.3 nm and the FWHM (full width at half maximum) $\Delta\lambda_1$ is equal to 0.104 nm for both s and p polarization incident wave; for the TM mode, the filter central wavelength λ_{TM} = 1422.2 nm and the FWHM $\Delta\lambda_2$ is equal to 0.224 nm. The FWHM is the same whether a voltage is applied or not. Hence, the filter, no matter it is based on a TE or a TM guided mode resonance, is independent of the incident polarization and this property persists when a voltage is applied.

The factor **Q** (wavelength to bandwidth ratio) can be calculated as:

$$Q_{TE} = \frac{\lambda_{TE}}{\Delta\lambda_1} = 14984$$
$$Q_{TM} = \frac{\lambda_{TM}}{\Delta\lambda_2} = 6354, \tag{3.9}$$

which are both extremely high.

The linewidth for the TM mode is more than twice larger than for the TE mode. This can be explained by the strength of the coupling between the incident field and the mode field. As the value of $\widetilde{\alpha}_{TE}$ is larger than $\widetilde{\alpha}_{TM}$, the TE mode decreases more quickly outside the guiding layer than the TM mode so that its field is more localized, and may show a narrower bandwidth. Yet, the coupling between the incident field and the mode field involves several parameters (see for example[16]) which may be different for the TE mode and the TM mode (especially because of the fact that the TM mode has a part of its electric field along z), and the difference between the effective index may be not the only explanation for the bandwidth difference.

3.4.3 Angular Peak Properties

To study the angular tolerance with respect to the incident wave beam, we move from the case of normal incidence to the oblique one. The wavelength of the incident plane wave is equal to the center wavelength of the resonant peak in the situation of normal incidence. The incident angle varies in the range of $[-\theta\,^\circ, \theta\,^\circ]$ in both xz and yz planes. We plotted both the reflective (solid line) and transmissive (dash line) efficiency with respect to the incident angle θ for s or p polarization, for both TE (Fig. 3.9) and TM modes (Fig. 3.10). The Full Width at Half Maximum (FWHM) is taken as a characteristic representing the angular tolerance of the filter. For each mode, the curves in the xz plane are similar to that in the xy plane which is due to the isotropy of the structure in the xy plane. We observe that the angular tolerances along the x and y directions are different, depending on the propagation direction of the mode. In particular, in Fig. 3.9(a) and (c), the excited modes propagate in both positive and negative directions parallel to the plane of incidence, while in Fig. 3.9(b) and (d), the direction of propagation of the modes is perpendicular to the plane of incidence. Note that the definitions of the directions of the s and p polarizations are given with respect to the plane of incidence.

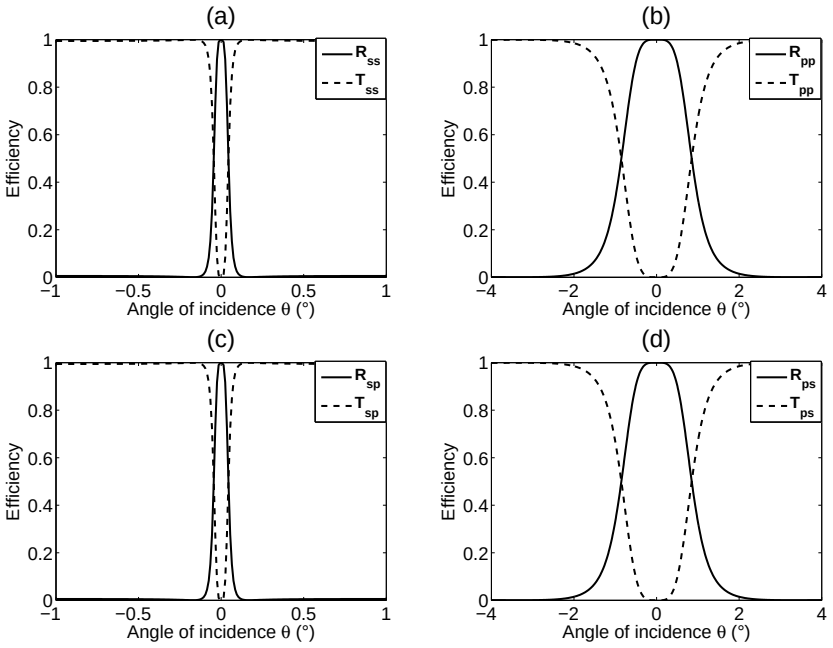

Figure 3.9 : *TE mode angular tolerance for the structure 5.4, $\lambda = 1559nm$. The incidence wave is: (a). s polarized in xz plane; (b). p polarized in xz plane; (c). s polarized in yz plane; (d). p polarized in yz plane.*

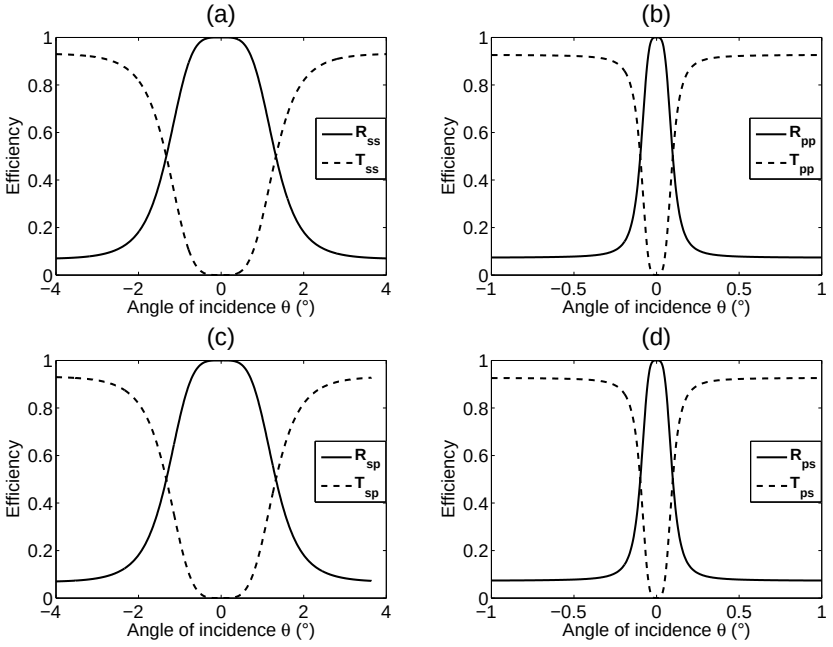

Figure 3.10 : *TM mode angular tolerance for the structure 5.4, $\lambda = 1422.2nm$. The incidence wave is: (a). xz incidence plane, s polarization; (b). xz incidence plane, p polarization; (c). yz incidence plane, s polarization; (d). yz incidence plane, p polarization.*

For the TE mode the wavelength of the incident plane wave is $\lambda = 1559nm$, which is the peak position wavelength under normal incidence. When the incident plane wave with

s or p polarization varies in the xz plane (3.9 (a) and (c)), the angular width is equals to $0.09\,^\circ$, however it increases to $1.71\,^\circ$ for the yz plane case (3.9 (b) and (d)). For the TM mode case the incidence wavelength is $\lambda = 1422nm$. When the incident plane wave with s and p polarization varies in the xz plane (3.10 (a) and (c)), the angular width is equals to $2.66\,^\circ$, however it reduces to $0.2\,^\circ$ approximately for the yz plane case (3.10 (b) and (d)).

These differences can be easily explained by considering the coupling equation: the norm of the in-plane resonant diffraction order wave vector $\overrightarrow{k_{inc}} + \overrightarrow{K}$ varies more rapidly with respect to the polar incidence angle θ when $\overrightarrow{k_{inc}}$ and $\overrightarrow{K}$ are collinear than when they are perpendicular to each other. Hence, the coupling condition is broken more rapidly with respect to θ in the former case than in the latter.

Since the field of a TE mode is orthogonal to its direction of propagation, an s polarized incident wave excites a TE mode propagating in the direction given by the plane of incidence (Fig. 3.9 (a) and (c)), and in the orthogonal direction when for a p polarized wave (Fig. 3.9 (b) and (d)). The contrary is true for a TM mode.

Now, we study the effect of applying a voltage. We applied a 5V voltage on the stack, the center resonant peak position of TE and TM modes move to 1558.2nm and 1421.6 nm, then we choose these new value as the incidence wavelength and do the same measurement. Calculation results are presented in Fig. 3.11 and 3.12 below:

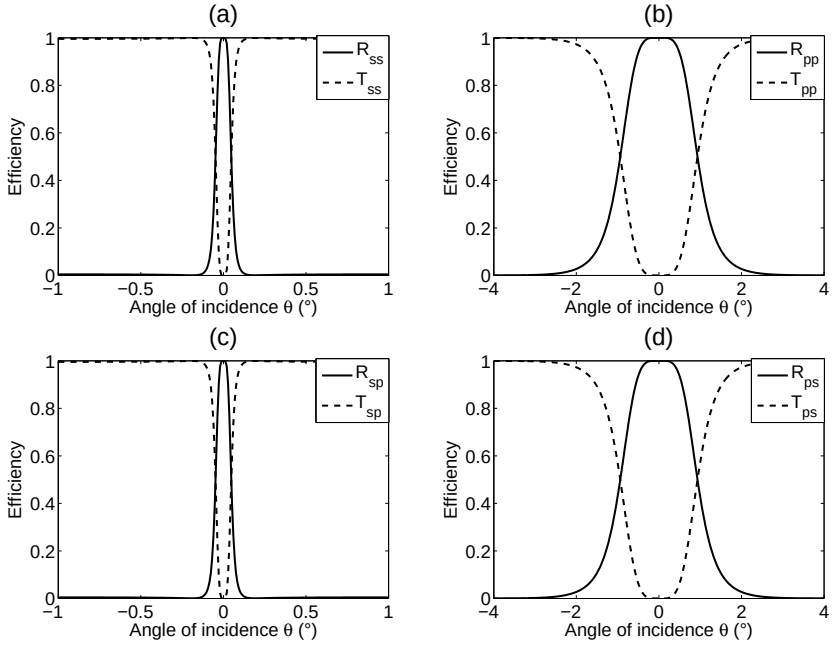

Figure 3.11 : *TE mode angular tolerance for the structure with 5V applied voltage, $\lambda = 1558.2nm$. The incidence wave is: (a). xz incidence plane, s polarization; (b). xz incidence plane, p polarization; (c). yz incidence plane, s polarization; (d). yz incidence plane, p polarization.*

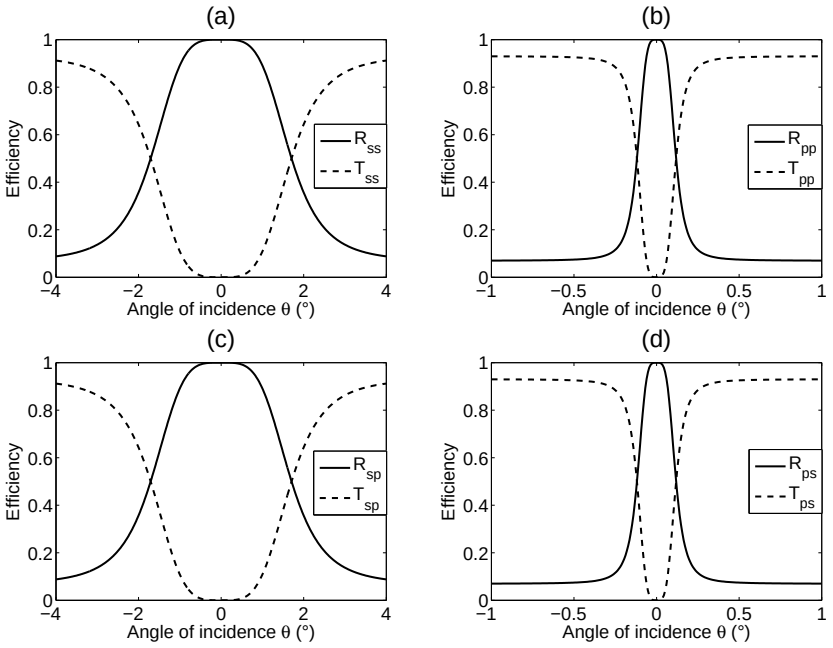

Figure 3.12 : *TM mode angular tolerance for the structure with 5V applied voltage, $\lambda = 1421.6nm$. The incidence wave is: (a). xz incidence plane, s polarization; (b). xz incidence plane, p polarization; (c). yz incidence plane, s polarization; (d). yz incidence plane, p polarization.*

From the two figures we can find that, when the external voltage is applied, the resonant peak position shifts but the angular tolerances are well kept. This is an important feature of this GMR tunable filter from for the application concerned.

3.5 Discussion on the Filter Manufacturing

In the previous two sections, we have studied numerically the characteristics of the tunable GMR filter which takes advantage of the electro-optical effect in the $LiNbO_3$ layer. This section is intended to discuss the manufacturing process of the filter. There are two key steps during the construction of the active filter: one is the fabrication of the stack, especially the deposition of the E-O thin film and another is the realization of the diffraction grating.

The choice of the technique and deposition parameters depends on the material's forms (amorphous or crystalline) and the optical properties required (permittivity, absorption coefficient and active behavior). Fabrication of $LiNbO_3$ layer has been studied by various methods, such as rf-magnetron sputtering[62], molecular beam epitaxy[63], liquid phase epitaxy[64], MOCVD[65], sol-gel method[66] and especially the pulsed laser deposition (PLD) technique[67]. The latter becomes an universally accepted solution to obtain high quality stoichiometric multicompetent thin film on various substrates, such as Al_2O_3, Si, SiO_2[68–70].

The main difficulty in fabricating the devices we propose is the problem of crystal growth on an amorphous material. Whereas epitaxial growth may partially solves this problem, recently wafer bonding and ion slicing process has been proposed to cut thin layers (680nm in particular) from a bulk crystal of an E-O material, and to deposit electrodes, amorphous buffers and other layers[71].

For the electrodes, it is important to ensure the minimum of absorption so as not to reduce the amplitude of the component's overall response. Moreover, in GMR filter, the resonance peak thinness and height are very sensitive to the material intrinsic absorption. On the other hand, the electrode's low resistivity corresponds to a high conductivity and allows itself to achieve stronger static electric fields. So apparently one should provide electrode layers whose resistivity and absorption are lowest as possible. As shown latter in chapter 4 for the case of $BaTiO_3$, the losses in ITO layers can completely spoil the resonance effect so that instead of a peak one observes a minimum in the reflectivity. This is due to the fact that the electrodes are positioned at the boundaries of the guiding layer. To avoid this, it is possible to separate them by a buffer layer of SiO_2 below, and to deposit the upper electrode on the grating surface before etching it (see Fig. 4.26 in chapter 4).

For a grating structure with dimension as those designed, and for the area of etching needed (at least $1mm^2$), the e-beam lithography is highly appropriate. The etching can be realized by the technique of reactive plasma etching. In the past ten years some resonant gratings with a "doubly periodic" pattern have been realized. The e-beam lithography was chosen to write the grating, followed by a dry etching. A detailed work of optical and geometric characterization of the sample has then followed in order to analyze the effect of the fabrication defaults on the optical properties of the component[72–74]. It appears that narrow spectral width can be achieved (0.28nm at 1550 wavelength) but that the performances (spectral bandwidth, reflectivity at resonance) are limited by the drift of one or more parameters during the fabrication process. As a conclusion, the angular tolerance of the filter must be as great as possible in order to diminish the impact of fabrication errors (the reflected beam spreads out all the lesser than the angular tolerance is large).

3.6 Conclusion

This chapter was devoted to the study of the guided mode resonance phenomenon in a structure including an electro-optic material ($LiNbO_3$) layer. We were able to demonstrate numerically the possibility to achieve a tunable narrow band filter based on the E-O effect.

The orientation of the crystal with respect to the static electric field has been chosen such that the greatest E-O coefficient of $LiNbO_3$ is involved. Then we contrasted four modes with different field profile excited in the equivalent homogeneous planar structure, in order to figure out the relationship between the tunability of the resonance peak and the modes.

The performances of the whole structure, including a bidimensional "doubly periodic" grating pattern have then been analyzed. Consistent with our expectations, the resonance peak showed a narrow filtering band (factor Q can reach 6000 theoretically), an optimized angular tolerance (0.09° for TE mode, 0.2° for TM mode), and a polarization independence. The polarization independence property, optimized angular tolerance, and spectral shape of the peak are preserved when a voltage is applied. The resonance peak shifts linearly with respect to the applied voltage. However, in the range of the material breakdown limit, the shift extends to less than 10nm. This may be not enough for most applications, so we move to another E-O material, namely $BaTiO_3$, to search for stronger tunability. $BaTiO_3$ is moreover a bi-axial anisotropic material, even when no voltage is applied, which will give more complex behavior with respect to the incidence polarization.

Chapter 4

Guided Mode Resonant(GMR) Filters Based on Barium Titanate

4.1 Introduction

Barium Titanate ($BaTiO_3$) has attracted a lot of interest since several decades because of its interesting properties. First, it is chemically and mechanically stable, second, it presents ferroelectric properties at and above room temperature, and finally it can be easily manufactured and used in the form of ceramic polycrystalline samples.[75] Polycrystalline barium titanate displays relatively large temperature coefficient of the electrical conductivity, making it a useful material for thermistors and self-regulating electric heating systems.[76,77] As a dielectric ceramics, it can be used for capacitors and as a piezoelectric material for microphones and other transducers.[78,79] Crystaline $BaTiO_3$ can also find use in nonlinear optics because of its high beam-coupling gain and large operating range from visible to near-infrared.[80] $BaTiO_3$ thin films display electrooptic modulation with extremely high frequency.[81] It has been reported as a key component in many application areas due to its good pyroelectric and ferroelectric properties, such as tunable microwave devices and memory devices.[82–84]

$BaTiO_3$ presents also a relatively strong electro-optic effect. In this chapter, we introduce $BaTiO_3$ as the active layer instead of $LiNbO_3$ used in chapter 3, aiming to achieve greater tunability of the GMR grating. The filter structure and simulation approach used in this chapter are basically the same as in chapter 3. The main difference is the orientation of the material with respect to the applied static electric field for the purpose of maximizing the modification of permittivity due to the E-O effect, that has interesting consequences on the resonant peak characteristics.

First, we present the E-O effect of the $BaTiO_3$ material and the orientation of this anisotropic material layer, as it was done in the Chapter 3. However, because of the difference between the crystalline structures of $BaTiO_3$ and $LiNbO_3$, we will consider two kinds of orientations of the $BaTiO_3$ crystal and compare with $LiNbO_3$. The structure description is omitted because it is already presented in the previous chapters. After that, we analyze the behavior of the resonant peak with respect to the applied voltage and with respect to the polarization of the incident wave. Narrow-band filtering and tunability are studied at first, followed by the analysis of the sensitivity with respect to the angle and polarization of the incident wave, addressed to two different filter structures.

4.2 Electro-Optic Effect in $BaTiO_3$

In this part, we introduce the electro-optic properties of $BaTiO_3$, we describe two kinds of orientations for the crystal and the modification of the permittivity tensor induced by an external static electric field in both cases.

4.2.1 Optical Properties and E-O Effect

$BaTiO_3$ has a high electro-optic coefficient as compared to many other ferroelectric materials. It can be grown on Si substrate using a buffer layer such as MgO[85] or TiN[86].

For $BaTiO_3$ crystal with a 4mm point-group symmetry, only five elements of linear E-O effect tensor are non-null, having only three different values. These elements are as follows:

$$r_{13} = r_{23}, \quad r_{51} = r_{42}, \quad r_{33} \tag{4.1}$$

As presented in chapter 1, a non-linear, quadratic electro-optic effect (Kerr effect) also exists in these crystals. This effect is generally concealed in materials presenting a Pockels effect. For example, the Kerr effect in the ferroelectric, tetragonal state of $BaTiO_3$ (below the Curie temperature of 120°C) is usually neglected in applications and even so, good comparisons between the simulations and the experimental results are obtained[30,81]. Yet, in resonant gratings, the slightest variation in the index has to be multiplied by the period to obtain the variation on the resonant wavelength (see the coupling eq. 1.2). Moreover, the order of magnitude of the Kerr coefficients[87] spur us on analyzing the influence of the Kerr effect. Note that above 120°C, $BaTiO_3$ exists in a paraelectric, cubic state (point group symmetry m3m). As in this state, the $BaTiO_3$ is centro-symmetric, the Pockels effect is not present, and the Kerr effect is more important than in the tetragonal state. The non null Kerr coefficients for $BaTiO_3$ in the tetragonal state that are involved in our non-centrosymmetric configuration are[17]:

$$s_{22} = s_{11}, \quad s_{32} = s_{31}, \quad s_{12} \tag{4.2}$$

Table 4.1 gives the comparison between $BaTiO_3$ and $LiNbO_3$, together with the value of the electro-optic coefficients and the refractive index.

Table 4.1 : *Comparison of the optical properties of $BaTiO_3$ and $LiNbO_3$* [87,88].

material	$LiNbO_3$	$BaTiO_3$
crystal type	negative uniaxial	negative uniaxial
symmetry system	3m	4mm
refractive index (1550nm)	n_o=2.211 n_e=2.138	n_o=2.437 n_e=2.365
linear E-O (pm/V)	r_{33}=30.8 r_{13}=8.6 r_{51}=28 r_{22}=3.4	r_{33}=28 r_{13}=8 r_{51}=1300
quadratic E-O ($\times 10^{-17} m^2/V^2$)		$s_{12} = -3.5 \pm 0.3$ $s_{13} = -8.0 \pm 0.7$

We observe that the refractive index of $BaTiO_3$ at 1550 nm is larger than that of $LiNbO_3$, this leads to higher index contrast between E-O and other dielectric layers, which is suitable for localization of the field of the guided mode predominantly in the E-O layer. In terms of E-O efficiency, the value of the coefficients r_{33} and r_{13} for the two materials are approximately equal, but the largest one of $BaTiO_3$ r_{51} (namely, r_{42}) is nearly 400 times larger than that of $LiNbO_3$. This rarely large electro-optic coefficient is of main interest to us, thus the E-O properties of $BaTiO_3$ will be discussed in detail in the next section.

For the quadratic E-O coefficients of $BaTiO_3$, we just listed two value of them in the table. To our knowledge only the values of these two coefficients are reported in the literatures[87]. Concerning the s_{22} coefficient that has not been evaluated in this article, we will consider that it is null. Yet, we have checked that if s_{22} has the same order of magnitude than s_{12} and s_{32}, it does not lead to a significant modification in the propagation constants of the modes. We separate the study of the linear and the quadratic E-O effect in two parts, at first addressing only the linear effect. Further on in sec. 4.7 we study the influence of the second-order terms on the tunability of the device, taking into account both

linear and nonlinear effects. This approach makes it possible to compare the magnitude of the two effects.

4.2.2 Crystal Orientations and Permittivity Variation

We have the choice to orientate the $BaTiO_3$ crystal in such a way that it is isotropic in the xy plane, as it was the case with $LiNbO_3$ in chapter 3 (Fig. 3.2). In this orientation the ordinary refractive index n_o lies in direction perpendicular to the axis z and the extraordinary refractive index n_e direction is parallel to z. When an electrical field along z is applied, the linear E-O effect modifies the permittivity tensor that takes the form:

$$\widetilde{\varepsilon_2} = \begin{pmatrix} \frac{n_o^2}{1+r_{13}E_z n_o^2} & 0 & 0 \\ 0 & \frac{n_o^2}{1+r_{13}E_z n_o^2} & 0 \\ 0 & 0 & \frac{n_e^2}{1+r_{33}E_z n_e^2} \end{pmatrix}, \tag{4.3}$$

In Fig. 4.1, we show the results of the permittivity change for this type of orientation. It can be said that all the elements of the permittivity tensor decrease almost linearly as the static field intensity in the z direction increases. The crystal remains isotropic with axis along z when an electric field is applied. The variation of ϵ_{zz} is larger than that of ϵ_{xx} and ϵ_{yy}, which can be explained by the fact that the coefficient r_{33} is greater than r_{13}. At the wavelength 1550nm, the permittivity change of ϵ_{xx} (or equivalently of ϵ_{yy}) is equal to 0.0049 from 0V to 10V, and the permittivity change of ϵ_{zz} is equal to 0.0153. The tendency of variation is same as for $LiNbO_3$ studied in chapter 3, however the values of change are even smaller than for $LiNbO_3$, so they can not satisfy our purposes, and we need to find another working configuration.

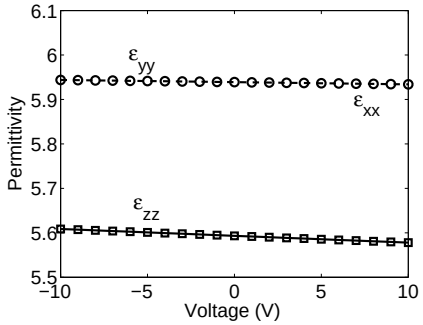

Figure 4.1 : *The permittivity tensor variations for first type of $BaTiO_3$ orientation.*

From the previous chapters, we know that the applied external electrical field modifies the index ellipsoid according to the Eq. 1.9. If we want to achieve the strongest E-O effect under the same electrical field condition, the greatest coefficient must be involved. The highest E-O coefficient of $BaTiO_3$ is the component r_{51}. Thus, we obviously have to orient the crystal to make its proper axis x_2 (or alternatively x_1) collinear to the axis z along which the electric field is applied. (see Fig. 4.2). In this configuration, the crystal is anisotropic in the xy plane, even if no static electric field is applied.

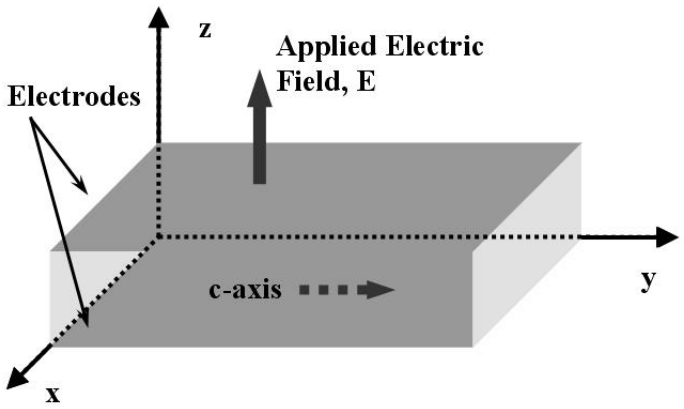

Figure 4.2 : *Schema of the material orientation with respect to the applied static electric field.*

In that configuration, when the external voltage is applied along the z direction, the permittivity tensor of the crystal with respect to the applied external electric field takes the following form in the (x,y,z) basis:

$$\begin{bmatrix} \Delta(\frac{1}{n^2})_1 \\ \Delta(\frac{1}{n^2})_2 \\ \cdot \\ \cdot \\ \cdot \\ \Delta(\frac{1}{n^2})_6 \end{bmatrix} = \begin{bmatrix} 0 & 0 & r_{13} \\ 0 & 0 & r_{13} \\ 0 & 0 & r_{33} \\ 0 & r_{42} & 0 \\ r_{51} & 0 & 0 \\ 0 & 0 & 0 \end{bmatrix} \begin{bmatrix} 0 \\ 0 \\ E_Z \end{bmatrix} \quad , \tag{4.4}$$

and the modified permittivity tensor can be rewritten in following form:

$$\widetilde{\varepsilon_1} = \begin{pmatrix} n_o^2 & 0 & 0 \\ 0 & \frac{n_e^2}{1-(r_{42}E_z n_o n_e)^2} & -\frac{r_{42}E_z(n_o n_e)^2}{1-(r_{42}E_z n_o n_e)^2} \\ 0 & -\frac{r_{42}E_z(n_o n_e)^2}{1-(r_{42}E_z n_o n_e)^2} & \frac{n_o^2}{1-(r_{42}E_z n_o n_e)^2} \end{pmatrix}, \tag{4.5}$$

We can see that, in addition to its initial anisotropy in the xy-plane without an external field, the index ellipsoid rotates around the x-axis when a static electric field is applied. It appears also that the index along x does not change.

In Fig.4.3, we show the numeric results of the permittivity changes for this type of orientation. For both configurations, the thickness of the $BaTiO_3$ layer is equal to 350nm, the external electrical field is applied along the z direction and varies from -10V to 10V, so that the static electric field varies in the range [-2.86, 2.86]$\times 10^7$ V/m, and remains under the breakdown limits of the material. The values for the reflective index are for a 1550nm wavelength.

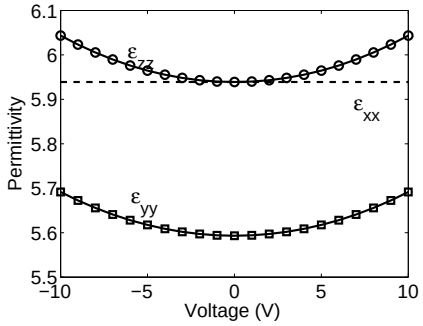

Figure 4.3 : *The permittivity tensor variations for the second type of $BaTiO_3$ orientation 2. , diagonal coefficients of $\widetilde{\varepsilon_1}$.*

We can observe in this figure that when an external electric field is applied, ϵ_{xx} remains unchanged, as expected from Eq. 4.5. The change of ϵ_{yy}, ϵ_{zz} has an approximatively quadratic relationship with the electric field intensity. The permittivity change of ϵ_{yy} is equal to 0.0983 from 0V to 10V, the permittivity change of ϵ_{zz} is equal to 0.1044. Comparing these values with those obtained in Fig. 4.1, it can be seen that the changes are more than six times greater in orientation 2 than in orientation 1.

Moreover, in this configuration, two off-diagonal elements, $\epsilon_{yz} = \epsilon_{zy}$, become non-zero when a static electric field is applied. Their variation with respect to the applied voltage is shown in Fig.4.4. The value of these two off diagonal elements varies linearly with the intensity, and the variation is larger than that of the diagonal elements.

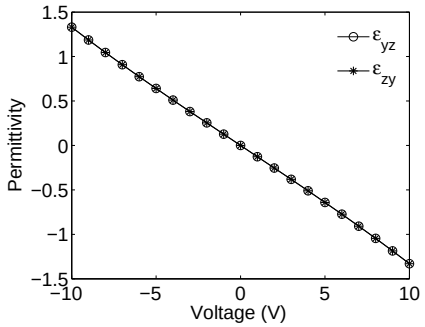

Figure 4.4 : *Variation of the out off diagonal elements of the permittivity tensor versus the external applied voltage.*

As a summary, in the first type of orientation, the crystal is uniaxial with isotropy in the xy plane, and this property is kept when a static electric field is applied along z. On the contrary, in the second one, the crystal becomes bi-axial, with one of its proper axis remaining along x, with the same index n_o.

At the same time, the elements along the diagonal have an approximative quadratic dependence on the applied voltage. These differences will have consequences in the resonant peak properties, which will be studied in detail in the next section.

4.3 Study of the Filter Based on E-O Effect in $BaTiO_3$

4.3.1 Filter Structure

In the same manner as for the filter based on $LiNbO_3$ described in chapter 3, we will use a bi-periodic two dimensional grating in order to study the resonance response of the waveguide. In order to chose the parameters of the structure, we follow the same optimization procedure as that described in chapter 3. Figure 4.5 and table 4.2 present the schema of the structure used in this chapter and the permittivity value for each layer from bottom to top respectively.

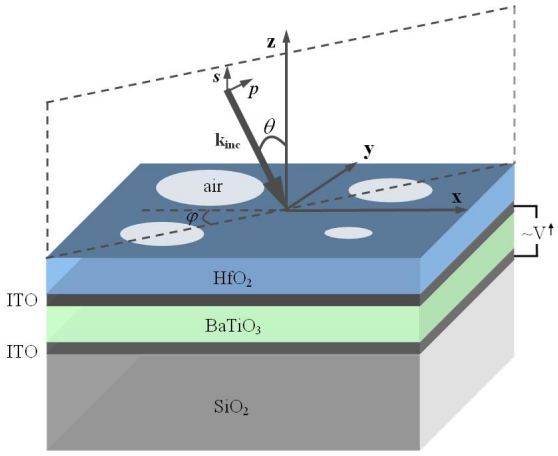

Figure 4.5 : *The schematic diagram of the GMR filter based on $BaTiO_3$.*

Table 4.2 : *Material's permittivity of each layer.*

Layer number	Material	Permittivity	Thickness
0 (substrate)	Silica	$\varepsilon_{SiO_2} = 2.082$	
1	ITO	$\varepsilon_{ITO} = 1.613$	50nm
2	$BaTiO_3$	$\varepsilon_{x,z} = 5.939$ $\varepsilon_y = 5.593$	-
3	ITO	$\varepsilon_{ITO} = 1.613$	50nm
4	HfO_2	$\varepsilon_{HfO_2} = 3.24$	100nm
5	HfO_2 and air	$\varepsilon_{HfO_2} = 3.24$ $\varepsilon_{air} = 1.00$	413.7nm
6(superstrate)	air	$\varepsilon_{air} = 1.00$	

The main change of the structure is the material of the guided-mode layer. Structures studied in the following have the similar composition but with different parameters, which are all given in the Appendix 2. As this filter structure has been explained in chapters 1 and 3, here we directly move to the discussion of the simulation approach.

4.3.2 Modal Structure of the Equivalent Homogenous Planar System

Following what we did for the structure based on $LiNbO_3$, we first search the modes of the equivalent homogeneous planar structure in order to properly choose the parameters

of the structure, namely the E-O layer thickness and the grating period. The following two images (Fig. 4.6) represent the dispersion relationship of the structure described in the previous paragraph.

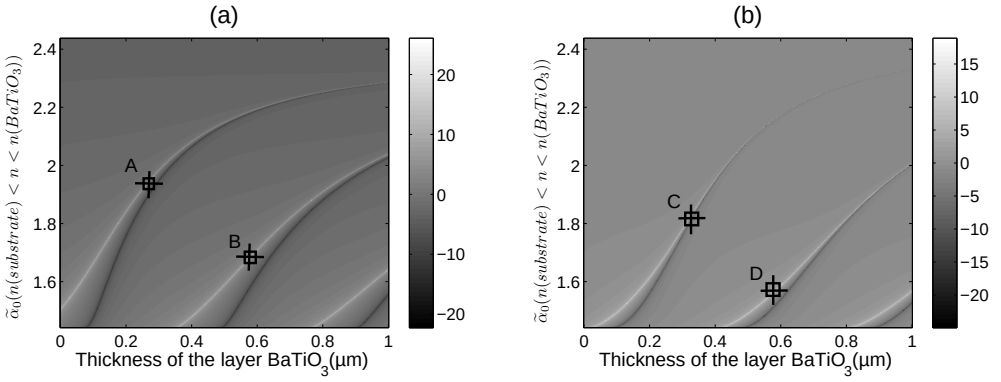

Figure 4.6 : *Dispersion relationship respect to $\widetilde{\alpha}_0$. (a). Dispersion image of TE mode; (b).Dispersion image of TM mode.*

We have plotted in Fig. 4.6 (a) the amplitude of the y component of the reflected electric field, versus the thickness h_{BaTiO_3} of the $BaTiO_3$ layer and $\widetilde{\alpha}_0$, the x component of the incident wave vector normalized with respect to the wavenumber in vacuum, for $\widetilde{\alpha}_0$ greater than 1. Hence, we can see in Fig. 4.6 (a) the evolution of the effective index of the guided modes of the equivalent planar structure with respect the h_{BaTiO_3} for TE modes, representing a resonance of the reflectivity calculated with evanescent incident wave. Note that when no voltage is applied, the proper axis of the crystal is along the x, y and z axis, so the modes propagating along x or y are pure TE or pure TM. Fig. 4.6 (b) is similar to Fig. 4.6 (a) but with the x component of the reflected electric field plotted, instead of the y component in order to represent the TM modes.

In these two figures, the thickness of the top equivalent layer is fixed at 519nm, and we set the wavelength equals to 1550nm and α_0 meets the condition:

$$max(n_{substrate}, n_{superstrate}) < \widetilde{\alpha}_0 < n_o(BaTiO_3),$$

where n stands for the corresponding refractive index. As the thickness increases, we observe appearence of greater number of modes in the structure. In addition, as expected, the effective index of the modes approach to a upper limit, which is equal to the ordinary reflective index n_o of $BaTiO_3$ for the TM modes (field along x and z), while for the TE modes (field along y), it approaches to the extraordinary reflective index n_e, as can be determined by the orientation of the index ellipsoid and shown in the following Fig. 4.7

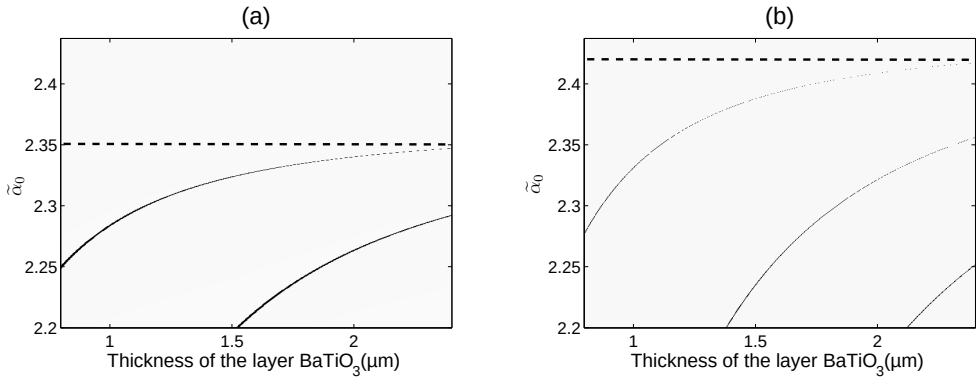

Figure 4.7 : *Limitation of the effective index of the modes propagating in x direction. (a). TE mode; (b). TM mode.*

Similar to the approach in chapter 3, we choose two different points in the dispersion profile as shown in Fig.4.6. Points A and C stand for the first order mode of the structure with a 341 nm thick $BaTiO_3$ layer. It is a TE (respectively TM) mode with effective index $\widetilde{\alpha}_0 = 2.01$ (respectively 1.87). Points B and D represent the second order modes of the structure with a thicker 570nm $BaTiO_3$ layer. It is a TE (respectively TM) mode with effective index $\widetilde{\alpha}_0 = 1.67$ (respectively 1.56).

Note that similar but different dispersion relations are expected with respect to $\widetilde{\beta}_0$, the y direction component of the incident wave vector normalized with respect to the wave number in vacuum, the difference being due to the anisotropy of the $BaTiO_3$ layer in the xy plane, as the following Fig. 4.8 shows:

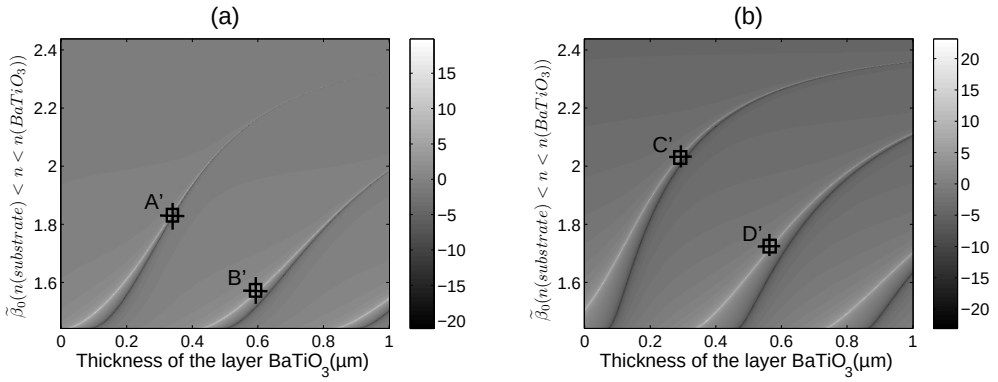

Figure 4.8 : *Dispersion relationship respect to $\widetilde{\beta}_0$. (a). Dispersion image of TM mode; (b).Dispersion image of TE mode.*

The characteristics of the excitation of these eight modes though a grating are studied in detail in the following.

4.3.3 Summary of the Properties of the Resonance Peaks in the Resonant Grating Structure

To excite the modes at points A and C (Fig. 4.6), we choose a period $D = 840$nm for the 2D grating, and $D = 956.8$nm to excite the modes at point B and D. All the parameters of these two structures (called respectively structure 1 and structure 2 throughout

this chapter)are summarized in the Appendix 2 (structure 1 is described in Fig.5.7 and structure 2 in Fig. 5.8).

For each structure, because of the anisotropy, we can expect four resonance peaks:

- one for the TE mode propagating along x,
- one for the TE mode propagating along y,
- one for the TM mode propagating along x,
- one for the TM mode propagating along y.

in fig. 4.9, we plot the spectral dependence around the four peaks for the structure 5.8:

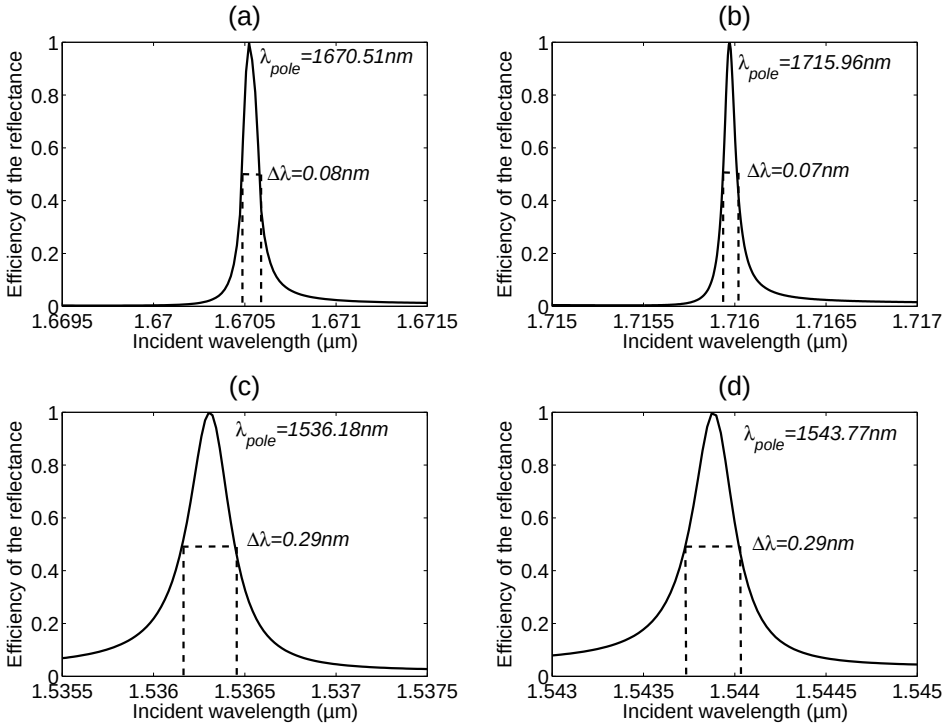

Figure 4.9 : *The resonant peak position and the linewidth of the four types of mode; (a). TE along x direction; (b). TE along y direction; (c). TM along y direction; (d). TM along x direction.*

From the simulated result, we can conclude that:

First, as expected, for one type of mode, the center wavelength of the resonance peak is different when the mode propagates along x or along y, because of the xy plane anisotropy of $BaTiO_3$. In particular, $BaTiO_3$ was oriented with its ordinary refractive index n_o along the x direction, and extraordinary index n_e along y direction, and for $BaTiO_3$, n_o is larger than n_e. A wave that propagates in the xz plane sees either n_e index (TE wave) or n_o index (TM wave). A wave that propagates in the yz plane see either the n_o index (TE wave), or both n_e and n_o (TM wave). We deduce that the effective index of the TE mode is greater when it propagates in the y direction than in the x direction. It follows, according

to the resonant condition, that the wavelength of a TE mode in y direction is larger than that along x direction, which is confirmed numerically. The oposite behavior is expected and numerically confirmed for the TM mode.

Second, the width of the resonance peaks is almost the same, independently of the direction of excitation, but different for the TE and TM modes. The width of a resonance peak depends mainly on the grating thickness, grating pattern, and profile of the field of the mode, especially in the grating region. The grating is invariant by a rotation that changes x in y, the system thickness is the same everywhere. Moreover, we can suppose that the profile of the field of the mode, especially in the grating region, is similar, if the mode propagates along x or y, since the anisotropy is weak, and the guided layer ($BaTiO_3$ layer) is far from the grating region. Theses remarks may explain the similar spectral width along x or y for the same polarization of mode.

Third, the peak width, corresponding to the TE mode is narrower than for the TM mode. This fact has already been explained in the chapter 3.

The factors **Q** (wavelength-to-bandwidth ratio) for these four resonance peaks corresponding to table 4.3 are equal to:

$$Q_A = \frac{1670.51}{0.08} = 20881 \qquad Q_{A'} = \frac{1715.96}{0.07} = 24514$$
$$Q_{C'} = \frac{1536.18}{0.29} = 5297 \qquad Q_C = \frac{1543.77}{0.29} = 5323,$$

which are all extremely high value.

The same calculations were done for the structure 2 (see Fig. 5.8 as shown in Appendix 2).

The following two tables summarize the calculated values of the most important characteristics, namely resonant peak linewidth, tunability, angular tolerance and polarization independence. The first four columns indicate the incidence polarization, the kind of mode excited in the structure (TE or TM), the center wavelength of the peak without applied voltage and also the FWHM of the resonance peak. The next two columns show the angular tolerance with respect to the polar incidence angle θ when the incident wave swing in the xz plane and yz plane respectively. In the last column, we also give the shift of the filter center when the applied voltage V is 5V, the details are given in the next subsections.

Table 4.3 : *Numerically computed results for the TE and TM modes in the structure 1 (Fig. 5.7 in appendix).*

Structure with D= 840nm and 341nm $BaTiO_3$ layer

	Incidence	Mode	Peak center (nm)	FWHM (nm)	Angular tolerance (x) (°)	Angular tolerance (y) (°)	Peak shift (nm)
1 - A	s	TE along x	1670.51	0.08	0.06	1.68	24.77
2 - A'	p	TE along y	1715.96	0.07	1.73	0.07	0.01
3 - C'	s	TM along y	1536.18	0.29	3.42	0.23	4.73
4 - C	p	TM along x	1543.77	0.29	0.19	3.27	-16.04

Modes 1 to 4 of structure 1 (Table 4.3) correspond to modes A, A', C' and C of the planar structure (see Fig.4.6 and 4.8). In fact, the modes of the structure including the grating are different from the modes of the equivalent planar structure because of the fact

that the grating modifies the field of the modes, especially in this configuration where two counter propagative modes can be excited in each direction. This is why we choose different notations for the modes.

Table 4.4 : *Numerically computed results for the TE and TM modes in the structure 5.8.*

Structure with D= 956.8nm and 570nm $BaTiO_3$ layer

	Incidence	Mode	Peak center (nm)	FWHM	Angular tolerance (x) (^{o})	Angular tolerance (y) (^{o})	Peak shift (nm)
1 - B	s	TE along x	1551.94	0.44	0.39	4.46	6.25
2 - B'	p	TE along y	1589.14	0.40	4.06	0.36	0.001
3 - D'	s	TM along y	1484.93	0.67	4.42	0.46	1.67
4 - D	p	TM along x	1494.06	0.67	0.46	7.39	-3.84

Modes 1 to 4 of structure 2 (Table 4.4) correspond to modes B, B', D' and D of the planar structure (see Fig. 4.6 and 4.8).

In the next sections, we present more details regarding the tunability, the angular tolerance and behavior versus the incident polarization of these resonance peaks.

4.4 Peak Shifts as a Function of the Applied Voltage

In this section, we anylise the tunability performances of the filter based on the $BaTiO_3$. First, we compare the tunability of the four modes excited in structure 1. Next, structure 1 and 2 are compared, in order to get a physical understanding of the phenomenon in this anisotropic case.

4.4.1 Comparison of the Tunability for the Four Modes of Structure 1

Fig. 4.10 shows the variation of the resonance peak position in the reflection spectra when the external applied voltage changes from 0 to 5 V . Fig. 4.10(a), (b), (c) and (d) correspond respectively to the modes 1, 2, 3 and 4 excited in structure 1.

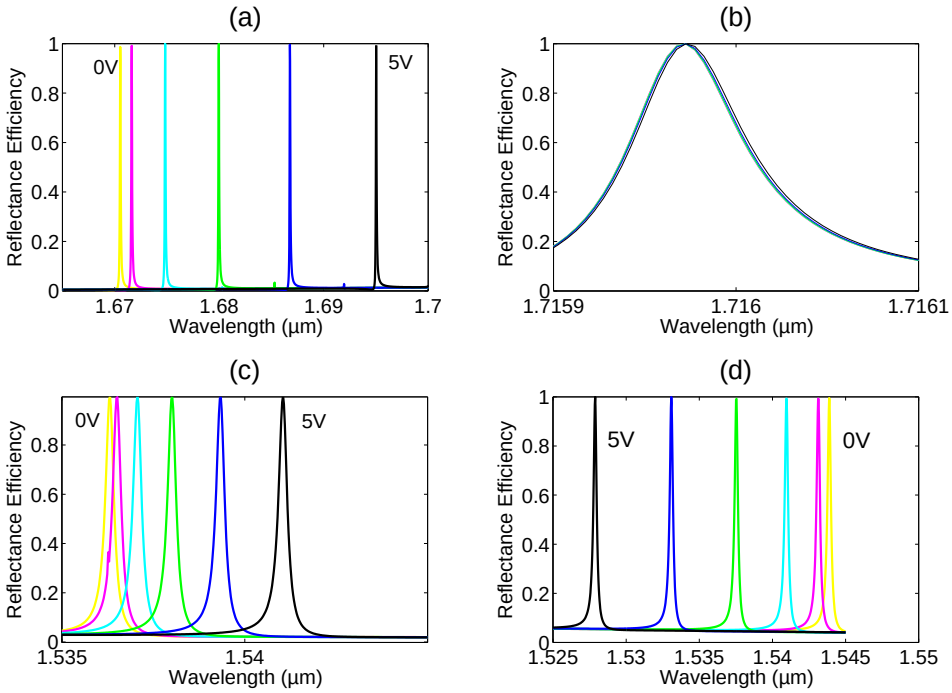

Figure 4.10 : *Simulated reflection spectra versus the applied voltages.*

We find that the TE mode along the x direction (Fig. 4.10a) shows the strongest tunability (24.77nm) among the four modes, but the same mode along the y direction (Fig. 4.10b) barely shifts (0.01nm) under the same condition (note the change of the scale in this figure). On the other hand, the TM mode propagating along x (Fig. 4.10d) shift is 16.04nm to the smaller wavelength, while the TM mode propagating along y (Fig. 4.10c) shift is only 4.73nm. In addition, in Fig.4.11, we have plotted the shift of the resonance peaks for the four modes with respect to the applied voltage.

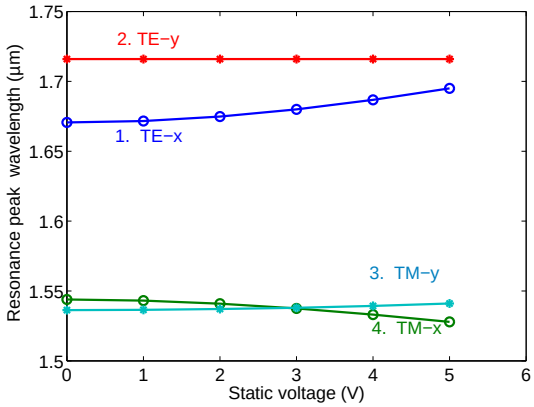

Figure 4.11 : *Resonance peak wavelength versus external static voltage for TE and TM modes in structure 1.*

To understand the evolution of the spectral position with the applied voltages, we study the change of the effective indexes of the modes that exist in the equivalent planar structure. Fig. 4.12 presents the variation of product of the grating period with these

effective indexes due the applied voltage, when the modes propagate in the x direction (β=0) and y direction (α=0) . The modes correspond to the engraved structure listed in the table 4.3. We observe quite the same variation in fig. 4.12, which means that the peak shift is mainly due to a modification of the guided mode (no grating effect) propagation constant.

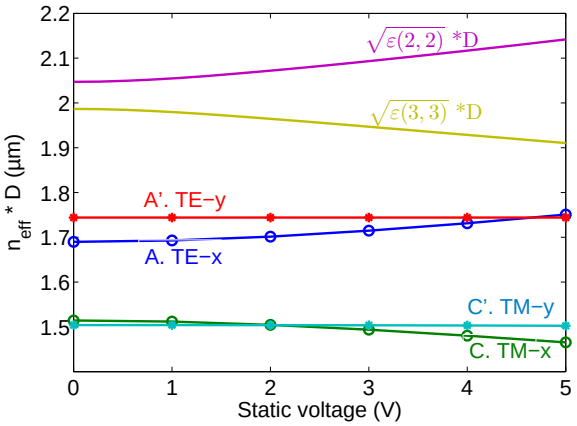

Figure 4.12 : *Effective index variation due to the external static voltage in the equivalent plane structure, situations A, A', C', C correspond to the situations 1, 2, 3, 4 in the Tab. 4.3.*

Moreover, it is possible to directly relate these changes to the variations of the permittivity tensor coefficients (Eq. 4.5), or equivalently the index ellipsoid.

When at first we deal with the case $\alpha = 0$ (mode propagates along y direction), the TE mode has its electric field along x, while the TM mode has its electric field along y and z. When a voltage is applied, as ϵ_{xy} and ϵ_{xz} remain null, the modes in the structure remain purely TE and purely TM types. Moreover, the independence versus the applied voltage of the effective index of the TE mode is easily explained by the fact that it is related to ϵ_{xx}, which does not depend on the applied voltage. On the other hand, the TM mode is related to ϵ_{yy} , ϵ_{yz}, ϵ_{zy} and ϵ_{zz} which change when a voltage is applied, but their effects may cancel each others, so that the effective index of the TM mode hardly depends on the applied voltage.

For the $\beta = 0$ case (modes propagating along x direction), the TE mode has its electric field along y, while the TM mode has its electric field along x and z. As ϵ_{yz} is not null when a voltage is applied, the guided modes can not be simply defined as pure TE or TM mode anymore, there is a mixing between the TE and TM components of the field.

Moreover, as voltage V increases, the material becomes a bi-axial anisotropic material. One of the proper axis of the crystal remains along x while the two others rotate in the yz plane. The coefficients of the permittivity tensor of the crystal in its proper axis stand for a limit for the effective index of the modes that can propagate in this medium. The coefficients in the plane yz are the eigenvalues for the permittivity tensor in Eq.4.5 and are given by:

$$\varepsilon_{2,2/3,3} = \frac{\epsilon_{yy} + \epsilon_{zz}}{2} \pm \sqrt{{\epsilon_{yz}}^2 + \frac{(\epsilon_{yy} - \epsilon_{zz})^2}{2}}. \tag{4.6}$$

As the applied voltage changes, the variation of $D\sqrt{\epsilon_{2,2}}$ and $D\sqrt{\epsilon_{3,3}}$ have been plotted in the Fig. 4.12. We can see that the mode (a) follows the variations of $\epsilon_{2,2}$ while the

mode (b) follows that of $\epsilon_{3,3}$. Eq.4.6 also gives the explanation of the fact that the shifts are independent of the sign of the applied voltage. Indeed, ϵ_{yz} and the electric field E_z is implied with a square power. This is also consistent with the quadratic dependence of the shift versus the applied voltage.

4.4.2 Comparison Between the Tunabilities of the Two Structures

We now compare the tunability of the two structures in order to analyze the influence of the profile of the mode on the tunability. For both structure 1 and structure 2 we found a TE and a TM mode propagating along two orthogonal directions. The results are presented in the table 4.3 and 4.4.

In the last column of these two tables, the shifts of the resonant peaks have been listed for the applied voltage augmenting from 0 to 5V. However, as the thicknesses of the layers are different, the static electric field intensity is not the same within the E-O layer, and the tunability are not directly comparable. In order to have a better comparison, we have plotted in Fig.4.13, the resonant peaks shifts with respect to the external field intensity rather than the voltage. In Fig. 4.13(a), the solid line and the dash line represent respectively the TE mode in the structure 1 and the TE mode in the structure 2. Circle marks and square marks stand for the modes propagating respectively along x direction and y direction. The same notations are taken for Fig. 4.13(b) to describe the TM mode.

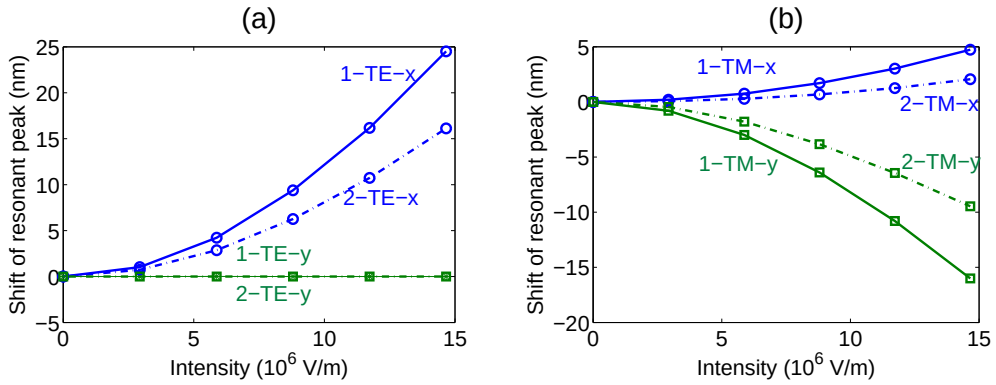

Figure 4.13 : *Shift comparison of the resonant peaks versus the applied voltages for two structures.*

We observe that the modes of the structure 2 have the same behavior with respect to the applied electric field as the modes of the structure 1. The only difference is that the peak shifts are larger in structure 1. This may be related either to the propagation constant of the modes (greater in structure 1) or to the field profile (first order in structure 1 and second order in structure 2). Following the conclusion obtained for the previous chapter on $LiNbO_3$, we believe that the shifts are bigger in structure 1 because the field of the modes are localized more strongly in the E-O layer (greater propagation constant) than that of structure 2.

4.5 Angular Tolerances

We use structure 2 to study the angular tolerances of the different modes along the different directions. From the table 4.4, we observe that the angular tolerances for modes

propagating along x and y are different and depend on the direction of the plane of incidence. For example, for the TE mode along the x direction, when the incident plane wave swing in the xz plane, the angular half-width reaches 4.46 °, however this value reduces to 0.44 ° approximately for the yz plane case. As already mentioned in the previous chapter on $LiNbO_3$, this can be easily explained by considering the coupling Eq. 1.2: the norm of the in-plane resonant diffraction order wave vector $\overrightarrow{k_{inc}} + \overrightarrow{K}$ varies more rapidly with respect to the polar incidence angle θ when $\overrightarrow{k_{inc}}$ and $\overrightarrow{K}$ are collinear than when they are perpendicular.

Nevertheless, because of the anisotropy in the xy plane the behavior of the peaks with respect to θ is more complex than in the $LiNbO_3$ case. To analyse the different cases, which contain both TE and TM modes propagating along x or y direction, we have calculated the modulus of the reflected electric field $|E|$ versus the incidence angle θ and the wavelength λ, as shown in fig. 4.14, when the incident plane is yz. In this figure, the bright curves correspond to the different modes presented in Table 4.4.

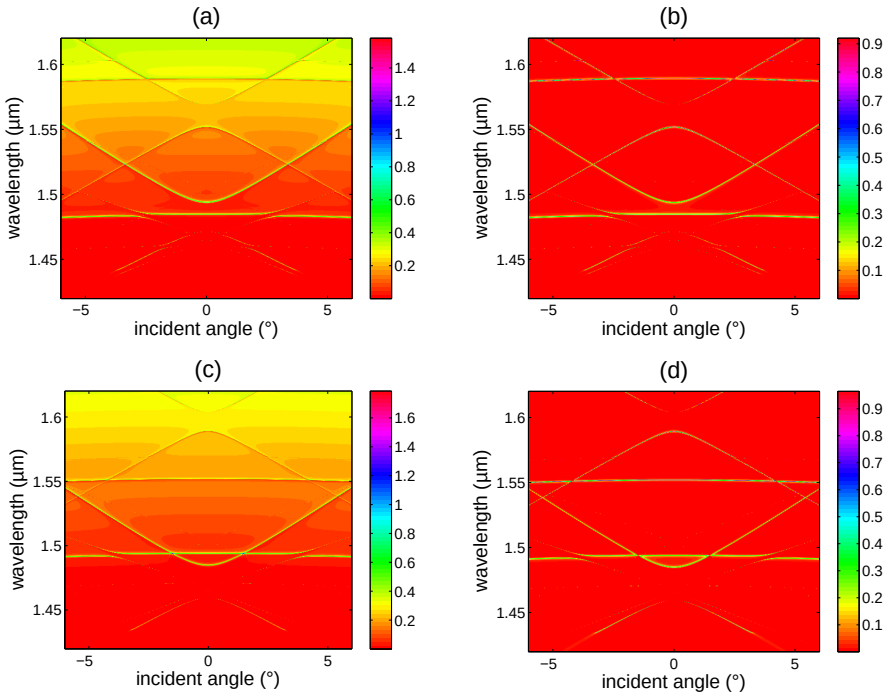

Figure 4.14 : *Map of the reflected field modulus with respect to the incidence angle θ and wavelength λ. (a) s polarization incidence, incident wave swings in xz plane; (b) p polarization incidence, incident wave swings in xz plane; (c) p polarization incidence, incident wave swings in yz plane; (d) s polarization incidence, incident wave swings in yz plane.*

The modes are identified thanks to their resonance wavelength under normal incidence. Moreover, depending on the degree of bend of the curve with respect to the incidence angle, we can distinguish easily the modes with great or weak angular tolerances.

For a detailed explanation for each situation, we zoom into the areas for each resonant peak under the normal incidence, as shown in Fig. 4.15 and 4.16 and plot the logarithm of $|E|$.

The sub-figures Fig. 4.15(a), (b) represent the situation where the incidence plane wave is xz and (c), (d) represent the yz plane case. For each image, the bright curve stands for the resonant peak, and we have represented the resonance wavelength at normal incidence by a dashed line. The strong dependence of the resonance wavelength with respect to the angle of incidence in Fig.4.15 (a) and (d) is consistent with the relatively low angular FWHM of 0.36 ° and 0.39 °. Similarly, the weak dependence of the resonance wavelength with respect to the angle of incidence in Fig. 4.15(b) and 4.15(c) is consistent with the relatively large angular FWHM of 4.46 ° and 4.06 °.

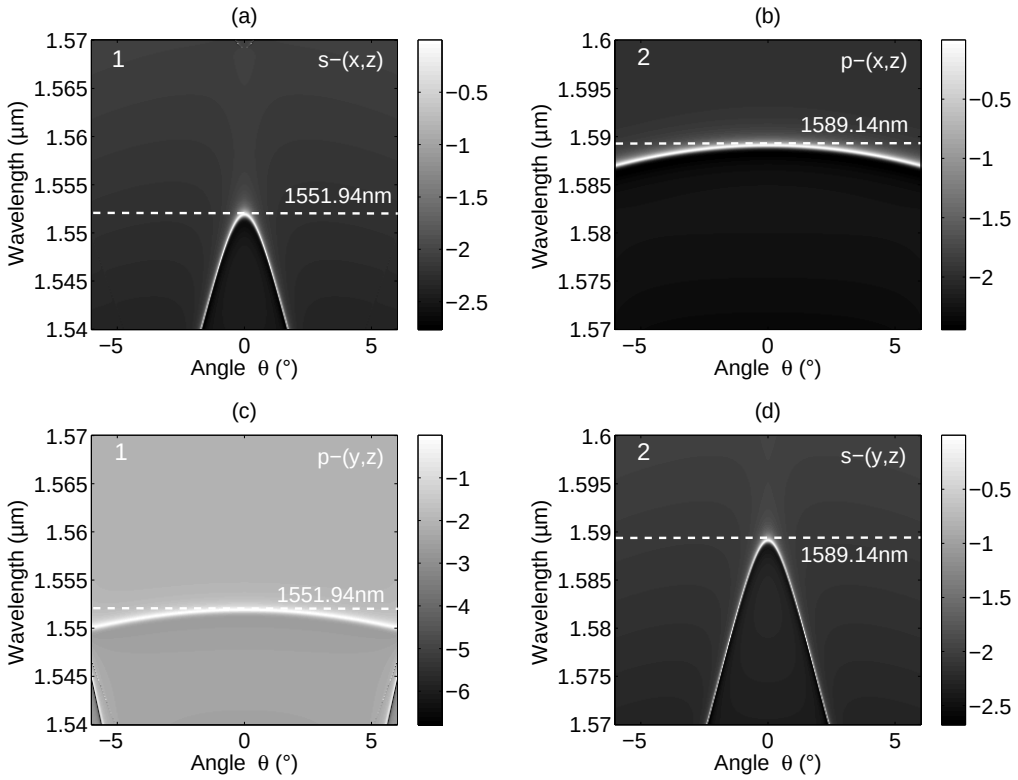

Figure 4.15 : *The angular tolerances for the TE mode. (a) s polarization incidence, incident wave swing in xz plane; (b) p polarization incidence, incident wave swing in xz plane; (c) p polarization incidence, incident wave swing in yz plane; (d) s polarization incidence, incident wave swing in yz plane.*

The analysis of the TM mode is much more complicated, due to the existing crossing points of the resonances in Fig.4.14(b) close to 1495 nm. Similarly as the TE mode, in Fig. 4.16 we show the reflected field distribution $|E|$ for the TM modes with s and p polarization incidences in the xz and yz plane of incidence with respect to θ and λ.

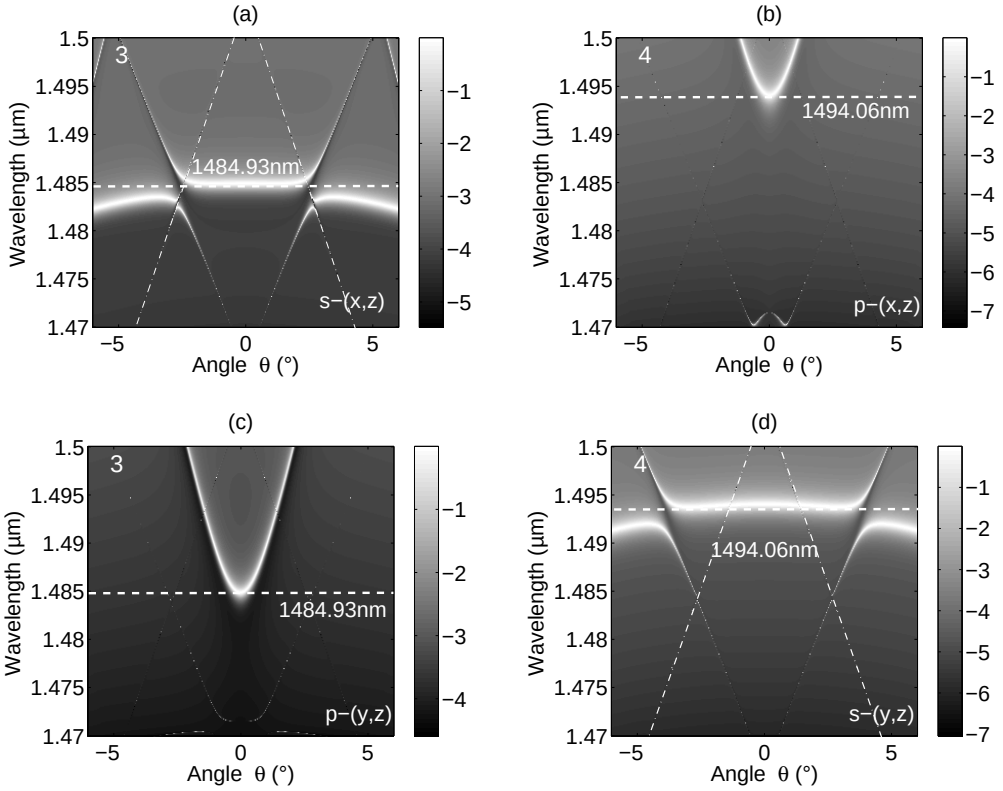

Figure 4.16 : *Same as in Fig.4.15 but for the TM mode. (a) s polarization incidence, incident wave swing in xz plane; (b) p polarization incidence, incident wave swing in xz plane; (c) p polarization incidence, incident wave swing in yz plane; (d) s polarization incidence, incident wave swing in yz plane.*

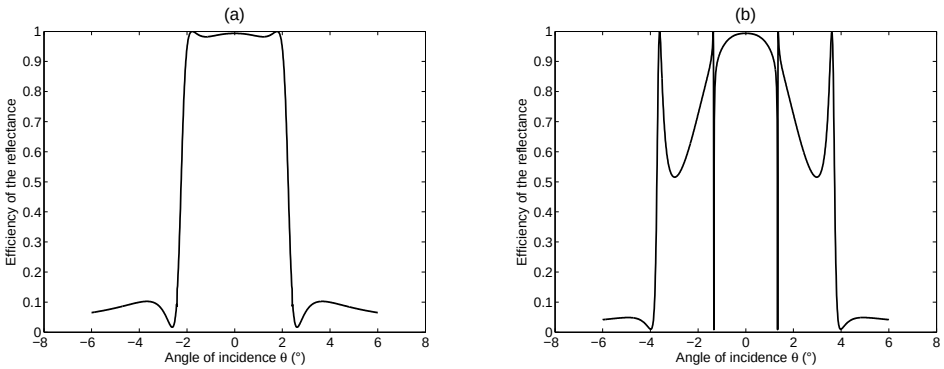

Figure 4.17 : *Two examples of angular dependence with coupling of TM modes. (a) TM mode along y direction, incident wave swing in xz plane, λ=1484.93nm; (b) TM mode along x direction, incident wave swing in yz plane, λ=1494.06nm.*

We observe curves having either a strong or a weak dependence with respect to θ, different for the two incident polarizations and planes of incidence. Contrary to Fig.4.15, we also observe supplementary curves, starting in fig. 4.16(a) around ($\theta \sim \pm 5\,^{\circ}, \lambda = 1.5\mu m$) and ($\theta \sim \pm 5\,^{\circ}, \lambda = 1.47\mu m$). They are due to the excitation of another mode (with effective index 2.22 in the plane equivalent structure) with the (1,-1), (1,1), (1,1),

and (-1,-1) diffraction orders. We plot in fig.4.17 the reflectivity versus θ for an incidence plane along xz (Fig. 4.17(a)) and yz (Fig.4.17(b)). This correspond respectively to a cut of Fig.4.16(a) for λ=1484.93nm and Fig.4.16(d) for λ=1494.06nm respectively in s-polarization. The excitation of the third mode is visible for $\theta \sim \pm 2^\circ$ in Fig. 4.17(a) and $\theta \sim \pm 1.33^\circ$ and $\theta \sim \pm 4^\circ$ in fig. 4.17(b). These points correspond to the intersection points between the curves visible in Fig.4.16(a) and in Fig.4.16(d).

4.6 Polarization Dependence

In order to use the greatest E-O coefficient of $BaTiO_3$, we have chosen to orientate the crystal with its optical axis along y. Hence, the crystal is anisotropic in the xy plane, and the resonance wavelength depends on the polarization of the incident wave, even when no voltage is applied. In this section we propose two approaches to try to recover the property of polarization independence with respect to the incident polarization, at least when no voltage is applied to the E-O crystal.

4.6.1 Approach i: Grating Period Optimization

The basic idea is to adjust the grating periods along x or y in order to bring together the two resonance peaks. We know that when the period increases, so does the peak center wavelength. Take the TM mode in structure 5.7 (table 4.3) as an example. The mode is excited at $\lambda_c = 1536.18$ nm along y, and $\lambda_d = 1543.77$ nm along x. The center wavelength λ_c of the peak corresponding to the mode excited along y is smaller, so we can increase the period D_y in the y direction to bring together the two resonance peaks.

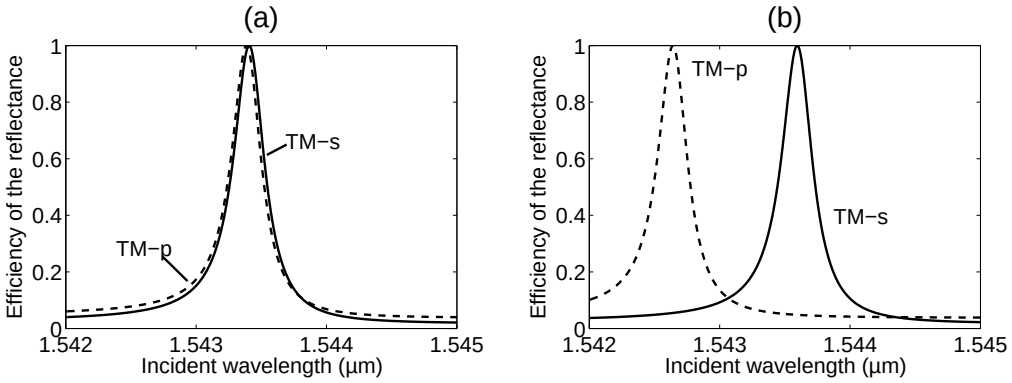

Figure 4.18 : *Two examples of polarization independence for TM modes. (a) TM mode for normal incidence with polarization s and p, λ_{pole}=1543.8 nm, without applied voltage; (b) TM mode for normal incidence with polarization s and p, with 1 V external voltage applied.*

For a period $D_y = 845.5$ nm (D_x remains equal to 840nm), we obtain two peaks, one for the s-polarization and the other for the p-polarization, that are superimposed when no voltage is applied, as shown in fig. 4.18(a).

However, the two resonant peaks are separated at about 1 nm when even only 1 V voltage is applied, as shown in Fig.4.18(b). The reason is that the two TM modes show different tunabilities, moreover, they are in opposite direction: for the TM mode along the y direction, the peak center moves to larger wavelengths when the voltage increases,

while the TM mode along the x direction shifts to smaller wavelengths. Meanwhile, the magnitude of the shift is also different. In conclusion, this approach is effective only in the situation without external voltage. In addition, the inevitable errors in the manufacture process make the accurate control of the period difficult.

4.6.2 Approach ii: Crystal Rotation

The basic idea is to have, when no voltage is applied, the same mode propagation constants along x and y. To do so, we rotate the crystal in such a way that its optical axis form an angle of 45 ° with respect to both directions of periodicity. Without applied voltage, the equivalent plane structure contains one quasi-TE mode and one quasi-TM mode, each one propagating in the x and y directions with the same propagation constant. The important difference with the previous configurations is that now the waveguide modes are elliptically polarized.

This peculiarity is quite important for understanding the next results. The following Fig.4.19 presents the spectral dependence of the reflectivity in the s and p polarizations for the grating structure under normal incidence without external voltage. The top figure is for s incident polarization, R_{ss} and R_{sp} are the energy reflected in the s and p polarizations, respectively. The bottom figure is for p incident polarization, R_{ps} and R_{pp} are the energy reflected in each polarization. The total energy reflected is also plotted. We observe two peaks both for incidences with s or p polarizations, centered at slightly different wavelength values, the first one at $\lambda_{pole} = 1540.2082nm$, and the second one at a distance of 23pm. The polarization conversion is due to the ellipticity of the waveguide mode polarization. The splitting of the positions of the maxima indicates that the grating induces coupling between the modes propagating in direction of x and y. This is possible directly through the grating orders (+/-1, +/-1), because the resonance effect requires excitation of one mode through the diffraction orders (+/-1, 0), and of the other mode through order (0, +/-1).

The mode interaction leads to a creation of two hybrid standing waves having two different resonant wavelengths. The difference is quite small (but detectable), because the coupling is weak. The coupling is possible because of the ellipticity of the modes of the equivalent plane structure (for which there is no coupling), and the fact that the constants of propagation in directions x and y are the same. In the case of $LiNbO_3$ (chapter 3), the waveguide modes of the unperturbed (by the grating) system propagating in perpendicular directions had linear polarizations that were mutually orthogonal in both vectorial and Hermitian sens, thus there was no coupling between them induced by the grating. In the case of $BaTiO_3$ with the crystal axis in y direction, the constants of propagation in direction x and y of the modes were different. In these cases, we observed no coupling between them, even if some of them were elliptically polarized. In the present configuration, the unperturbed (without the grating) modes propagating in perpendicular directions are polarized elliptically, so that their polarizations are mutually orthogonal, but represented as complex vectors. Due to this, the polarizations are not orthogonal in Hermitian sens. This fact makes the coupling between the modes by the grating orders possible.

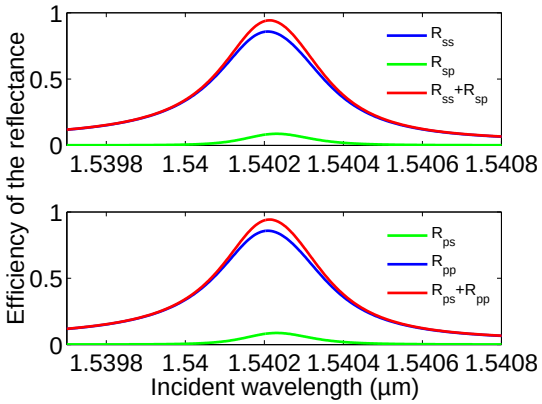

Figure 4.19 : *Reflected energy with incident polarization s (top) and p (bottom), without applied voltage. R_{ab} stands for the energy reflected in polarization a when the incident field is b polarized.*

The coupling that leads to a splitting of positions of the spectral maxima also leads to a decrease of the overall reflectivity maximum from the theoretical 100%, obtained without this coupling. An indeed, the overall energy reflected reaches a maximum of 94.3%, calculated at 1540.2132 nm. As a consequence, the filter is not polarization independent, strictly speaking. This can be observed in the reflectivity at the resonance wavelength when the incident polarization varies. In fig. 4.20, we have plotted the reflectivity at the resonance wavelength with respect to the angle ψ between the incident electric field and the x-axis.

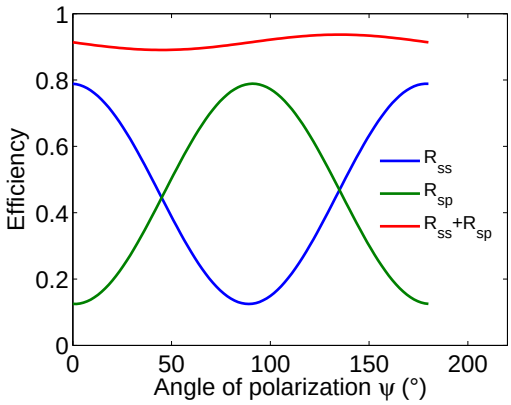

Figure 4.20 : *Reflectivity at the resonance wavelength with respect to the angle ψ between the incident electric field and the s vector.*

As observed, without external voltage the polarization dependence is relatively weak. However, when we apply voltage, the two peaks obtained for different incident polarization split up strongly, as Fig. 4.21 shows for 3 V voltage used. The splitting is almost 3 nm, and the maximum values reach again 100%. The explanation is simple and comes from the rotation of the index ellipsoid with the applied voltage, so that the z axis does no more remain parallel to the ellipsoid axes.

Hence, the modes of the plane equivalent structure propagating along x and y have no more the same propagation constants, thus the large spectral separation of the peaks. The spectral separation makes it impossible the coupling between the modes propagating in perpendicular directions, as far as their propagation constants become different. It can be noticed that the mode excited is either pure TE or pure TM. In fact, the mode excited is obtained by the combination of two counter-propagative modes (along x and $-x$ on one hand, and y and $-y$ on the other hand). This combination may lead to pure TE and pure TM modes.

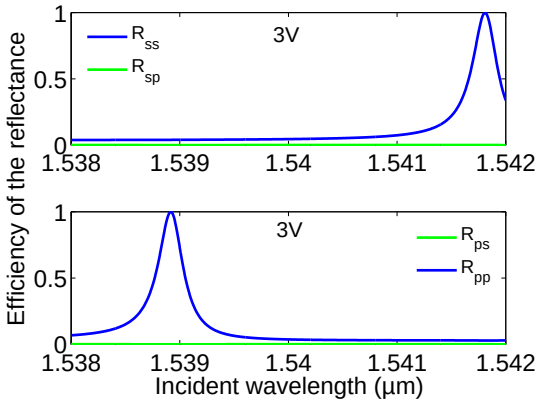

Figure 4.21 : *Reflected energy with incident polarization s (top) and p (bottom), 3V applied voltage. R_{ab} stands for the energy reflected in polarization a when the incident field is b polarized.*

4.7 Tunability Due to Both Linear and Quadratic Electro-optic Effects

As discussed in section 2, $BaTiO_3$ in its room-temperature phase presents both linear and quadratic electro-optic effects. In the previous section we have observed that the linear E-O effect gives the possibility of tuning the position of the resonant maximum in reflection, due to the excitation of a TE waveguide mode, within a range of 25 nm with only 5V external voltage. Although usually second-order effects are weaker than the linear one, it appears that this is not true in our case. Fig. 4.22 presents the variation versus the applied voltage of the elements of the matrix of $\tilde{\epsilon}$, as it was done in Fig. 4.3, but now taking into account both linear and quadratic terms in Eq. 1.11. There are several differences between Fig. 4.3 and Fig. 4.22. At first, taking into account the quadratic effect too, ε_{xx} varies with the applied field, contrary to the linear case. Second, the variations of the other elements are more than twice stronger than when considering only the linear effect, except for ε_{zz}, which changes only slightly compared to the linear case. Third, the variation of the off-diagonal term is no more linear. However, the signs of the variations are the same as in Fig. 4.3, so we can expect the same directions for the shifts of the resonance wavelengths due to the different modes, and similar spectral response, because the modal structure without applied voltage is not influenced by the quadratic E-O effect. This is confirmed by our numerical calculations, as shown in Fig. 4.23.

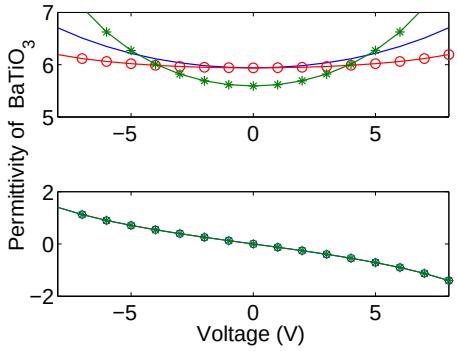

Figure 4.22 : *Changes of the permittivity tensor with respect to the applied voltage taking into account both linear and quadratic effects. ϵ_{xx}, ϵ_{yy}, ϵ_{zz} correspond respectively to linear, star and circle marks in the up figure; ϵ_{yz}, ϵ_{zy} are presented as circles and stars in the low figure.*

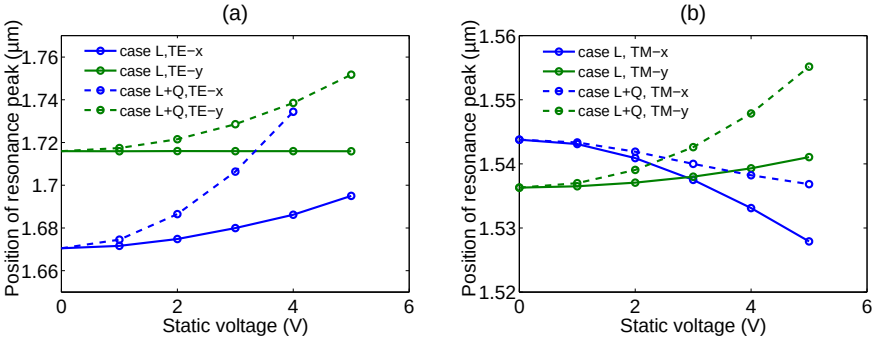

Figure 4.23 : *Resonant peak wavelength versus external static voltage for TE and TM modes in structure 1 in two different cases. Case L corresponds to the linear E-O effect only, in case L+Q both linear and quadratic E-O effect are involved. (a) TE mode in the structure; (b) TM mode in the structure.*

In this figure, we have plotted the shift of the resonant peaks corresponding to the different modes listed in the Table 4.3 as a function of the applied voltage. For comparison, both the linear case (case L) and the linear plus quadratic case (case L+Q) are represented. Contrary to the linear case, we observe a significant shift of the peak of the TE mode that propagates in the y direction, because of the variation of ε_{xx}. For the other modes, that involve the three coefficients ε_{yy}, ε_{zz} and ε_{yz}, their behavior can be explained by the variation of the elements ε_{22} and ε_{33} of the permittivity tensor in the proper axes of the index ellipsoid as it was done in subsection 4.4.1. We have found that ε_{33} decreases less rapidly in the L+Q case than in the L case, which explains the smaller shift of the quasi TM-x mode. The most interesting case from a practical point of view is the stronger shift of the quasi TE-x mode which is related to the faster increase of ε_{22} in the L+Q case. For this mode, the shift of the peak reaches 63.9 nm for 4 V applied (from 1670.5 nm to 1734.4 nm) without visible change of its width which remains close to 0.08 nm.

4.8 ITO Absorption

All the materials we use in our design are practically lossless around 1550 nm, except for ITO, the extinction index of which we have neglected till now. In non-resonant devices, the losses in the ITO layers can be neglected in practice, because the electrodes are optically quite thin. However, when resonant effects are used, even small values of extinction coefficients can lead to large absorption, in particular if the absorbing layers are put in the region of the device where the field is strong. Table 4.5 presents the spectral position of the resonant maximum of the TM-x mode and its maximum values for several different values of the relative permittivity of the ITO layers and for two different configurations. The first configuration corresponds to the structure 1 (Fig.5.7) studied in the previous paragraphs while the second is presented in the following. There are several different values of real and imaginary parts of the refractive index of ITO known in the literature, depending on the deposition conditions.

Table 4.5 : *Absorption of the ITO layer.*

Configuration	Index	Peak position	Line width	Efficiency
1	$1.27 + 0i$	1543.8nm	0.29nm	100%
	$1.27 + 0.12i$	1543.8nm	-	0%
1	$1.61 + 0.01i$	1570.2nm	-	0%
	$1.61 + 0.0003i$	1570.2nm	0.46nm	51%
2	$1.61 + 0.0003i$	1587.7nm	0.47nm	98.88%
	$1.61 + 0.01i$	1587.7nm	0.57nm	84.0%

Figure 4.24 presents the resonant peaks of the TM mode, the refractive index of ITO corresponds to the first two lines of the table use for the real part the values given by Luxpop[89]. If the losses are neglected, the maximum reaches 100%, as the Fig. 4.24 (a) shown. However, when the losses are taken into account, in the Fig. 4.24 (b), the resonance peak disappeared and the maximum is replaced by a minimum.

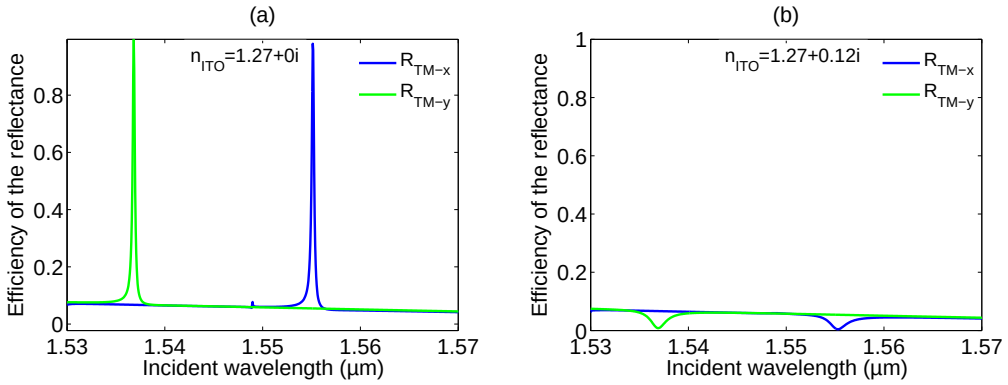

Figure 4.24 : *Resonant peaks of TM mode with configuration described in Fig.5.7. (a). refractive index $n_{ITO} = 1.27 + 0i$, losses are neglected; (b). refractive index $n_{ITO} = 1.27 + 0.12i$, losses taken into account.*

The second two lines of the table 4.5 correspond to another value of the real part of the refractive index[90]. We have also plotted the TM mode resonant peaks in Fig. 4.25, it can be observed that the change of refractive index leads to a shift of the spectral position

of the maximum. However, when the true losses are considered, the maximum disappears, as in the previous case. It is necessary to decrease the losses almost thirty times, to obtain a peak reaching 51% as Fig. 4.25(b) shows, because the electrodes are attached to the high-index guiding layer of $BaTiO_3$.

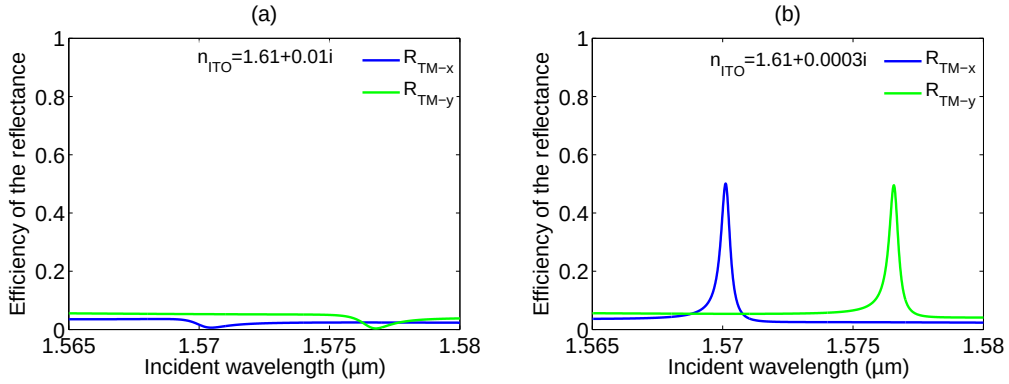

Figure 4.25 : *Resonant peaks of TM mode with configuration described in Fig. 5.9. (a). refractive index* $n_{ITO} = 1.61 + 0.01i$*, true losses are considered; (b). refractive index* $n_{ITO} = 1.61 + 0.0003i$*, decrease value of losses.*

It is possible to decrease the effect of ITO absorption by removing the electrodes away from the guiding layer. This can be done by introducing a buffer layer between the electro-optical layer and the lower electrode. The upper electrode can be deposited over the grating structure before it is etched. This configuration is sketched in Fig. 4.26 and is called configuration 2 in the Table 4.5.

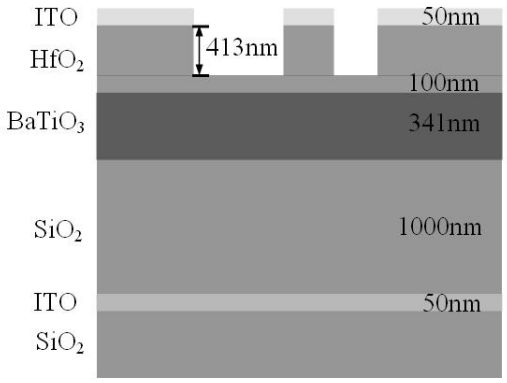

Figure 4.26 : *Schematic diagram of the configuration described in Fig. 5.10.*

As can be observed in Fig. 4.27(a), even with real values of the losses, it is possible to increase the maximum up to 84%. Moreover, the most interesting case of the quasi TE-x mode, which exhibits the greatest tuning is fortunately less influenced by the losses and the reflectivity reaches 93.8% for configuration 2 as Fig. 4.27(b) shows, even when the imaginary part of the index is equal to 0.01. Another configuration for the electrodes has been proposed and experimentally studied[91], however with larger linewidths and at smaller wavelengths.

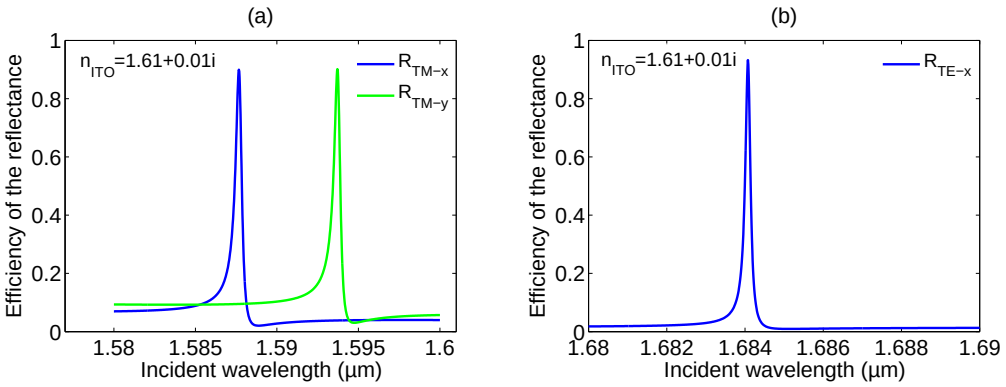

Figure 4.27 : *(a). Resonant peaks of TM mode with configuration described in Fig. 5.9, refractive index $n_{ITO} = 1.61 + 0.01i$, true losses are considered; (b). Resonant peaks of TE mode along x direction with configuration 5.9, refractive index $n_{ITO} = 1.61 + 0.01i$, true losses are considered.*

4.9 Conclusion

In this chapter, we have studied numerically a guided mode resonance filter containing an E-O $BaTiO_3$ layer. We have used two different orientations of $BaTiO_3$ layer, with the purpose of maximize the influence of E-O effect. The results enabled us to confirm numerically the conception of tunable narrow band filter based on the E-O effect in anisotropic material. We have compared the resonant resonances due to the excitation of different kind of guided modes: TE modes and TM modes, first and second order modes with different propagation constants. Depending on the mode, we have obtained strong or weak spectral shifts of the resonant peaks, toward greater or smaller wavelengths. These shifts correspond to the variations of the propagation constant of the guided mode of the equivalent plane structure (without grating). We have reached nearly 64nm (24 nm if the quadratic effect is neglected) of tunability for a peak with Q factor of 20000, for 4 V which is below the $BaTiO_3$ breakdown. The same behavior is observed when taking into account the linear (Pockels) effect only, or both linear and quadratic effects. This device can find application such as for example to adjust the wide spectrum laser source to an optimum wavelength.

The anisotropy of the structure, leads, as expected to a dependence of the peak position on the polarization of the incident wave. It also leads to a more complex behavior with respect to the incidence angles than for isotropic structures. All theses points show the importance of taking into account the anisotropy of the $BaTiO_3$ in the simulations.

We believe that this detailed study of $BaTiO_3$ based guided-mode resonance filter paves the way for further studies, including experimental studies, particularly as we have shown that the deterioration of the spectral selectivity and efficiency caused by the absorption losses of ITO can be reduced by choosing a suitable design.

Chapter 5

Conclusion and Perspectives

5.1 Conclusion

In the introduction, we have raised four pivotal questions that have guided our study, and now we fell capable to give the answers and explanations. This has become possible because of the preliminary work made to extend the existing numerical code for modelization of diffraction by gratings having 2D periodicity to the case when one or more of the plane layers in the structure are made of anisotropic materials.

- How does the applied voltage affect the permittivity of E-O materials within different crystal orientations? What is the impact on the guided modes of the structure?

  Two different typical electro-optic materials, Lithium Niobate and Barium Titanate, have been chosen because of their large E-O coefficients. According to their different crystalline structure and symmetry type, different orientations of the crystal with respect to the static electric field have been chosen such that the greatest E-O coefficient can be involved.

  For the $LiNbO_3$ case, we have considered only the linear E-O effect, and we have chosen the orientation to make the c-axis of $LiNbO_3$ parallel to the static electric field direction. Under this condition, the orientation of the index ellipsoid does not change with the static field, but the values of the ellipse's radii vary. Hence, $LiNbO_3$ still keeps its uniaxial negative characteristic with optical axes along z, but with different refractive index values. The conservation of the isotropy in the xy plane is very interesting for our filtering application purpose, especially concerning the property of polarization independence.

  For the $BaTiO_3$ case, its largest E-O coefficient is the off-diagonal element r_{51} (r_{42}), so we have oriented the crystal to make its proper axis x_2 collinear to the axis z along which the electric field is applied. In this orientation, there is an initial anisotropy in the xy-plane without an external field, and the index ellipsoid rotates around the x-axis when static electric field is applied. For the permittivity tensor, ϵ_{11} remains unchanged, the change of ϵ_{22}, ϵ_{33} has an approximatively quadratic relationship with the electric field intensity. The changes are several times larger than that in $LiNbO_3$ case.

  Also for $BaTiO_3$ case, when quadratic E-O effect was also taken into account, with the same configuration and same orientation, ϵ_{11} varies with the applied field, contrary to the linear case, the variations of the other elements are more than twice stronger than when considering only the linear effect, except for ϵ_{33}, which changes only slightly compared to the linear case. Meanwhile, the variation of the off-diagonal term is no more linear.

  These peculiarities of $BaTiO_3$ strongly affect the polarization response of the device.

- What is the magnitude of the tunability achievable?

  We have confirmed numerically the interest of using an E-O material to tune the center wavelength of a narrow band filter. When the electric field was applied to the E-O layer, the wavelength of the resonant peaks center shifts in the spectrum as the external voltage changes. It can be conclude that, for the GMR filter with $LiNbO_3$ layer, the magnitude of the tunability is linear with respect to the applied

voltage, and in the range of the material breakdown limit, the shift extends to less than 10nm; the $BaTiO_3$ case is more complicated, we have observed strong or weak spectral shifts of the resonant peaks, toward greater or smaller wavelengths. It can reach nearly 64nm (24 nm if the quadratic effect is neglected) of tunability for a peak with Q factor of 20000, for 4 V applied to a layer of $BaTiO_3$on having 341nm thickness, which is below the breakdown intensity.

- How can the tunability be maximized? What are the favorable configurations? Is it possible to exhibit key parameters involved in the tunability?

  It has been confirmed that the peak shift is mainly due to a modification of the guided mode propagation constant, which is the consequence of the variation of the permittivity tensor caused by the applied electric field. Yet, to these questions, we can not give a simple answer, for certain. According to our analysis of different E-O materials and grating configurations, we have found that it not sufficient to only maximize the E-O change of the permittivity tensor components by a proper orientation of the crystal axis, because different guided modes (propagating in different direction and having different polarization) are affected in a different manner by these changes of permittivity. Even when we take advantage of the largest E-O coefficient, different modes exist in the structure that show different tunabilities, as observed for the $BaTiO_3$. The conclusion is that each configuration requires for separate study of tunability.

- How does the anisotropy of the structure impacts the properties of the GMR filter, in particular: resonant peak linewidth and tunability maximum, angular tolerance and polarization independence?

  As expected, the anisotropy of the structure leads to a dependence of the peak position on the polarization of the incident wave, and also to a more complex behavior with respect to the incidence angles than for isotropic structures.

  Concerning the question of tunability, in the $LiNbO_3$ case, the resonance peaks for both the TE and the TM mode shift to the shorter wavelength direction as the applied voltage increases and the shifts are linear with respect to the voltage. We have also found that, under the same intensity condition, the shift of the TM mode is larger than TE mode. In the $BaTiO_3$ case, because of the anisotropy of the structure, the same TE and TM modes propagating along two orthogonal directions have different propagating constants. Among them, TE mode along the x direction shows the strongest tunability, but the same mode along the y direction barely shifts under the same condition. On the other hand, the TM mode propagating along x direction shifts obviously (24nm under 5V voltage) to the smaller wavelength, while the shift of the same mode propagating along y direction is only about quarter of that. However, the quadratic E-O effect makes some changes to these values. Contrary to the linear case, we can observe a significant shift of the peak of the TE mode propagating in the y direction, because of the variation of ϵ_{11}. The shift of the quasi TM mode along x direction becomes smaller in this case, because the components of the permittivity tensor decrease less rapidly than in the linear case. The most interesting case from a practical point of view is the stronger shift of the

quasi TE mode along x direction: it still holds the strongest shift without visible change of its width, and the value of the shift is twice than before.

Concerning the question of angular tolerance, for both the $LiNbO_3$ and $BaTiO_3$ cases, we have observed that the angular tolerance is stronger when the incident wave varies in a plane perpendicular to the direction of propagation of the mode as compared to the case when the incident wave varies in a plane parallel to the direction of propagation of the mode. Moreover, the anisotropy in the $BaTiO_3$ case leads to a more complex behavior since the modes propagating along the x and y directions can not have the same propagation constant.

Concerning the question of polarization independence, in the $LiNbO_3$ case, the polarization independence character of the double periodic grating has been well maintained, even when external electric voltages were applied. However, in the $BaTiO_3$ case, the anisotropy contains two parts, one is the intrinsic anisotropy due to the orientation of the crystal, and another is the derivation of the permittivity ellipsoid coming from the electric field. This anisotropy causes the resonance wavelength to depend on the polarization of the incident wave, and is resposible to different tunability values when the voltage applied.

5.2 Perspectives

Although we have done detailed numerically studies of E-O material based guided-mode resonance filter, there still exist several critic problems unsolved and other possibility for further research. Generally speaking, they can be organized into three main points:

- The problem of polarization dependence
  The tunable GMR filter based on $BaTiO_3$ shows a strong tunability, but it suffer from the polarization dependence. At the end of the chapter 4, we have attempted two approaches to solve this problem, but both of them failed. The method of grating period optimization can superpose the resonant peaks in the spectrum for incidence with s or p polarization when there is no external electric field, however, when the voltage is applied, the two resonant peaks split. Thus, this approach is effective only in the situation without external voltage. Meanwhile, it is difficult to make the accurate control of the period in practice. The second approach is the crystal rotation. As observed, without external voltage the polarization dependence is relatively weak. However, when we apply static voltage, the two peaks obtained for different incident polarization split up strongly. We intend to find a better solution to make the filter being polarization independent with or without applied voltage, and maintain appropriate tunability.

- Filter Fabrication
  The work in this thesis is mainly numerical, some reality factors have been neglected. When we want to manufacture the tunable GMR filter, there are two key factors that must be considered.

  The first is the problem of crystal growth on an amorphous material. Whereas epitaxial growth may partially solves this problem, recently wafer bonding and ion slicing process has been proposed to cut thin layers (680nm in particular) from a bulk crystal of an E-O material, and to deposit electrodes, amorphous buffers and

other layers[71]. Although this method has been applied to $LiNbO_3$, future work is required to study the possibility to apply this method to $BaTiO_3$.

The second is the absorption of the electrode material ITO. All the materials we use in our design are practically lossless around 1550nm, except for ITO. In non-resonant devices, the losses in the ITO layers can be neglected in practice. However, when resonant effects are used, even small values of extinction coefficients can lead to large absorption, in particular if the absorbing layers are put in the region of the device where the field is strong. At the end of the chapter 4, we have tried to introduce a buffer layer between ITO and E-O layer, the refractive efficiency can be controlled in an acceptable range, but more work focused on the configuration design should be done to improve the efficiency performance.

- Choice of Other E-O Materials
  In this thesis, we focused on $LiNbO_3$ and $BaTiO_3$. In fact, there are also many other E-O material who have impressive E-O effect performance, all of them could be used to realize the goal of tunable filtering. Among them, liquid crystals or polymers of liquid crystals show a sufficient potential. The refractive index can highly change when a voltage is applied. Some research works have to be done in this area.

Bibliography

[1] D. Rosenblatt, A. Sharon, and A. A. Friesem. Resonant grating waveguide structures. *IEEE J. Quantum Electron.*, 33(11):2038 – 2059, 1997.

[2] G. Keiser. A review of WDM technology and applications. *Opt. Fiber Techno.*, 5:3 – 39, 1999.

[3] N. Gat. Imaging spectroscopy using tunable filters: a review. In *Proc. SPIE*, volume 4056, pages 50 – 64, 2000.

[4] C. Bacon, Y. Mattley, and R. DeFrece. Miniature spectroscopic instrumentation: applications to biology and chemistry. *Rev. Sci. Instrum.*, 75:1 – 16, 2004.

[5] G. Niederer, H. P. Herzig, J. Shamir, H. Thiele, M. Schnieper, and C. Zschokke. Tunable, oblique incidence resonant grating filter for telecommunications. *Appl. Opt.*, 43:1683 – 1694, 2004.

[6] Rémy Parmentier. *Filttre interférentiel à bande étroite accordable principes de base et application au secteur des télécommunications optiques.* PhD thesis, Univ. de Droit, d'Economis et des Sciences d'Aix-Marseille, 2002.

[7] R. Magnusson and S. S. Wang. New principle for optical filters. *Appl. Phys. Lett.*, 61:1022 – 1024, 1992.

[8] R. R. Boye, R. W. Ziolkowski, and R. K. Kostuk. Resonant waveguide-grating switching device with nonlinear optical material. *Appl. Opt.*, 38:5181 – 5185, 1999.

[9] S. Woltman, G. Jay, and G. Crawford. Liquid-crystal materials find a new order in biomedical applications. *Nat. Mater.*, 6:929 – 938, 2007.

[10] A. Sharon, D. Rosenblatt, A. A. Friesem, H. G. Weber, H. Engel, and R. Steingrueber. Light modulation with resonant grating waveguide structures. *Opt. Lett.*, 21:1564 – 1566, 1996.

[11] H. Ichikawa and H. Kikuta. Dynamic guided-mode resonant grating filter with quadratic electro-optic effect. *J. Opt. Soc. Am. A*, 22:1311 – 1318, 2005.

[12] T. G. Levy-Yurista and A. A. Friesem. Light modulation with electro-optic polymer-based resonant grating waveguide structures. *Opt. Expre.*, 13:4645 – 4651, 2005.

[13] Q. Wang, D. Zhang, Y. Huang, Z. Ni, J. Chen, Y. Zhong, and S. Zhuang. Type of tunable guided-mode resonance filter based on electro-optic characteristic of polymer-dispersed liquid crystal. *Opt. Lett.*, 35:1236 – 1238, 2010.

[14] Fuchiyi Yang. *Energy Transduction in Surface Photonic Crystals.* PhD thesis, Univ. of Illinios at Urbana-Champaign, 2011.

[15] S. Massenot, R. Chevallier, J.-L. de Bougrenet de la Tocnaye, and O. Parriaux. Tunable grating-assisted surface plasmon resonance by use of nano-polymer dispersed liquid crystal electro-optical material. *Opt. Commu.*, 275:318 – 323, 2007.

[16] A.-L. Fehrembach. *Réseaux résonnants à bande interdite photonique, nouveaux filtres pour le D.W.D.M.* Thesis, Aix Marseille Université, 2003.

[17] A. Yariv and P. Yeh. *Optical waves in crystals.* Wiley, 1984.

[18] E. Popov, E. Mashew, and D. Maystre. Theoretical study of the anomalies of coated dielectric gratings. *Opt. Acta.*, 33 (5):607 – 619, 1986.

[19] A.-L. Fehrembach, A. Sentenac, and D. Maystre. Phenomenological theory of filtering by resonant dielectric gratings. *J. opt. Soc. Am. A*, 19 (6):1136 – 1144, 2002.

[20] A.-L. Fehrembach, F. Lemarchand, A. Talneau, and A. Sentenac. High Q polarization independent guided-mode resonance filter with doubly periodic etched Ta2O5 bidimensional grating. *J. of Lightwave Techno.*, 28:2037 – 2044, 2010.

[21] A.-L. Fehrembach, A. Talneau, F. Lemarchand, O. Boyko, and A. Sentenac. Experimental demonstration of a narrowband, angular tolerant, polarization independent, doubly periodic resonant grating filter. *Opt. Lett.*, 32:2269 – 2271, 2007.

[22] A.-L. Fehrembach, D. Maystre, and A. Sentenac. Phenomenological theory of filtering by resonant dielectric gratings. *J. Opt. Soc. Am. A*, 19:1136 – 1145, 2002.

[23] A.-L. Fehrembach and A. Sentenac. Study of waveguide grating eigenmodes for unpolarized filtering applications. *J. Opt. Soc. Am. A*, 20 (3):481 – 488, 2003.

[24] A. Yariv and Y. Pochi. *Optical Waves in Crystals: Propagation and Control of Laser Radiation.* John Wiley and Sons Inc., New-York, 1983.

[25] R. C. Alferness. Waveguide electro-optic modulators. *IEEE Trans. Microwave Theory Tech.*, 30:1121 – 1137, 1982.

[26] T. O. Murphy, E. J. Murphy, and R. W. Irvin. An 8 * 8 ti : LiNbO3 polarization independent photonic switch. Photonics in Switching/ECOC, pages 174 – 176, Florence, Italy, 1994.

[27] D. M. Gill, C. W. Conrad, G. Ford, B. W. Wessels, and S. T. Ho. Thin-film channel waveguide electro-optic modulator in epitaxial BaTiO3. *Appl. Phys. Lett.*, 71:1783 – 1785, 1997.

[28] Z. Y. Yu, F. Xu, X. W. Lin, X. S. Song, X. S. Qian, Q. Wang, and Y. Q. Lu. Tunable broadband isolator based on electro-optically induced linear gratings in a nonlinear photonic crystal. *Opt. Lett.*, 35:3327 – 3329, 2010.

[29] Ed L. Wooten, K. M. Kissa, A. Yi-Yan, E. J. Murphy, D. A. Lafaw, P. F. Hallemeier, D. Maack, D. V. Attanasio, D. J. Fritz, G. J. McBrien, and D. E. Bossi. A review of lithium niobate modulators for fiber-optic communications systems. *IEEE J. Quantum Electron.*, 6:69 – 81, 2000.

[30] A. Petraru, J. Schubert, M. Schmid, and Ch. Buchal. Ferroelectric BaTiO3 thin-film optical modulators. *Appl. Phys. Lett.*, 81(8):1375 – 1377, 2002.

[31] Practical uses and applications of electro-optic modulators. In *link, http://www.newport.com/New-Focus-Application-Note2-Practical-Uses-and-Ap/919642/1033/content.aspx.*

[32] P. Yeh, A. Yariv, and C.-S. Hong. Electromagnetic propagation in periodic stratified media i: General theory. *J. Opt. Soc. Am.*, 67:423, 1977.

[33] W. J. Gunning. Electro-optically tuned spectral filters: A review. *Opt. Eng.*, 20:837, 1981.

[34] J. F. Lotspeich, R. R. Stephens, and D. M. Henderson. Electrooptic tunable filters for infrared wavelengths. *IEEE J. Quantum Electron.*, 18:1253, 1982.

[35] E. A. B. Saleh and M. C. Teich. *Fundamental of Phontonics.* John Wiley and Sons, Inc., New-York, 1991.

[36] M. G. Moharam and T. K. Gaylord. Rigorous coupled-wave analysis of planar-grating diffraction. *J. Opt. Soc. Am.*, 71:811 – 818, 1981.

[37] P. Lalanne and G. M. Morris. High imptoved convergence of cerenkov second-harmonic generation through a graded-index grating coupler: eletromagnetic optimization. *J. Mod. Opt.*, 13:779 – 784, 1996.

[38] G. Granet and B. Guizal. Efficient implementation of the couple-wave method for metallic grating in TM polarization. *J. Opt. Soc. Am. A*, 13:1019 – 1023, 1996.

[39] L. Li. Use of fourier series in the analysis of discontinous periodic structure. *J. Opt. Soc. Am. A*, 13:1870 – 1876, 1996.

[40] L. Li. Formulation and comparison of two recursive matrix algorithms for modeling layered diffrcation gratings. *J. Opt. Soc. Am. A*, 13:1024 – 1035, 1996.

[41] E. Popov and M. Nevière. Maxwell equations in fourier space: fast-converging formulation for diffraction by arbitrary shaped, periodic, anisotropic media. *J. Opt. Soc. Am. A*, 18:2886 – 2894, 2001.

[42] M. Nevière and E. Popov. *Light propagation in peroidic media, differential theory and design.* Marcel Dekker, New-York, 2003.

[43] L. Li. New formulation of the fourier modal method for crossed surface-relief gratings. *J. Opt. Soa. Am. A*, 14:2758 – 2776, 1997.

[44] Y. Zeng, X. Tang, K. Fu, and Z. Wang. Vector diffractive analysis for two-dimensional relief gratings made with anisotropic medium. *Acta Opt. Sin.*, 23:95 – 100, 2003.

[45] N. Château and J. P. Hugonin. Algorithm for rigorous coupled-wave analysis of grating diffraction. *J. Opt. Soc. Am. A*, 11:1321 – 1331, 1994.

[46] N. P. K. Cotter, T. W. Preist, and J. R. Sambles. Scattering-matrix approach to multilayer diffraction. *J. Opt. Soc. Am. A*, 12:1097 – 1103, 1995.

[47] M. G. Moharam, D. A. Pommet, E. B. Grann, and T. K. Gaylord. Stable implementation of the rigorous coupled-wave analysis for surface-relief gratings : enhanced transmission matrix approach. *J. Opt. Soc. Am. A*, 12:1077 – 1086, 1995.

[48] I. Kaminov. *Introduction to Electro-Optics Devices*. Academic, New York, 1985.

[49] T. Tamir. *Guided-wave Optoelectronics*. Springer-Velag, New York, 1990.

[50] A. M. Prokhorov and Yu. S. Kuz'minov. *Crystalline Lithium Niobate*. The Adam Hilger Series on Optics and Optoelectronics, Bristol, 1990.

[51] R. S. Weiset and T. K. Gaylord. Lithium niobate: Summary of physical properties and crystal structure. *Applied Physics A*, 37:191 – 203, 1985.

[52] T. Maldonado and T. Gaylord. Electrooptic effect calculations for arbitrary cases. *AppL Opt.*, 27(24):5051 – 5065, 1982.

[53] N. Korkishko, V. A. Fedorov, E. A. Baranov, M. V. Proyaeva, T. V.Morozova, F. Caccavale, F. Segato, C. Sada, and S. M. Kostritskii. Characterization of a-phase soft proton-exchanged LiNbO3 optical waveguides. *J. Opt.Soc. Am. A*, 18(5):1186 – 1191, 2001.

[54] S. Kostritskii, Y. N. Korkishko, V. A. Fedorov, A. N. Alkaev, V. S.Kritzak, P. Moretti, S. Tascu, and B. Jacquier. Leakage of a guided modecaused by static and light-induced inhomogeneities in channel HTPE-LiNbO3 waveguides. In C. Righini, editor, *Integrated Optical Devices: Fabrication and Testing*, volume 4944 of *Proc. SPIE*, page 346, 2003.

[55] E. Krätzig and O. F. Schirmer. Photorefractive materials and their applications i. In *The Adam Hilger Series on Optics and Optoelectronics*, pages 131 – 166. Springer, Berlin, Heidelberg, 1988.

[56] R. Baets, P. Kaczmarski, and P. Vankwikelberge. Photorefractive materials and their applications i. In R. M. de la Rue J. H. Marsh, editor, *Design and modeling of passive and active optical waveguide devices*, NATO ASI E226, pages 21 – 71, 1992.

[57] A. Yariv. *Optical Electronics*. Holt, Rinehart and Winston, New York, 1985.

[58] B. A. Georges. *Microstructuration par échange photonique sur Nibate de Lithium: application à la réalisation des fonctions de filtrage*. PhD thesis, Université Paris-Est, 2008.

[59] Y. Avahami. *BaTiO3 based materials for piezoelectic and electro-optic applications*. Thesis, Massachusetts Institue of Technology.

[60] Lithium Niobate, *http* : *//en.wikipedia.org/wiki/Lithium_niobate*.

[61] L. J. Meng and F. Placido. Annealing effect on ITO thin films prepared by microwave-enhanced dc reactive magnetron sputtering for telecommunication applications. *Surface and Coatings Technology*, 166:44 – 50, 2002.

[62] N. Fujimura, M. Kakinoki, H. Tsuboi, and T. Ito. LiNbO3 film with a new epitaxial orientation on R-cut sapphire. *J. Appl. Phys*, 75:2169, 1994.

[63] R. A. Betts and C.W. Pitt. Growth of thin-film lithium niobate films by molecular beam epitaxy. *Electron. Lett.*, 21:960, 1985.

[64] H. Tamada, A. Yamada, and M. Saitoh. LiNbO3 thin-film optical waveguide grown by liquid phase epitaxy and its application to second-harmonic generation. *J. Appl. Phys.*, 70:2536, 1991.

[65] Z. Lu, R. Hiskes, S. A. Dicarolis, R. K. Feigelson, F. Leplingard, and J. E. Fouquet. Epitaxial $linbo_3$ thin films on sapphire substrates grown by solid source MOCVD. *J. Mater. Res.*, 9:2258, 1994.

[66] T. A. Derouin, C. E. Lakeman, X. H. Wu, J. S. Speck, and F. F. Lange. Effect of lattice mismatch on the epitaxy of sol-gel LiNbO3 thin films. *J. Mater. Res.*, 12:1391, 1997.

[67] J. W. Son, S. S. Orlov, B. Phillips, and L. Hesselink. Pulsed laser deposition of single phase LiNbO3 thin film waveguide. *J. Electroceram*, 17:591 – 595, 2006.

[68] Y. Shibata, K. Kaya, K. Akashi, M. Kanai, T. Kawai, and S. Kawai. Preparation and characterization of LiNbO3 thin films produced by chemical-vapor deposition. *J. Appl. Phys.*, 77:1498, 1995.

[69] M.-B. Lee, M. Kawasaki, M. Yoshimoto, and H. Koinuma. Heteroepitaxial growth of BaTiO3 films on Si by pulsed laser deposition. *App. Phy. Lett.*, 66:1331 – 1333, 1995.

[70] D. Ghica, C. Ghica, M. Gartner, V. Nelea, C. Martin, A. Cavaleru, and I.N. Mihailescu. Pulsed laser deposition of lithium niobate: a parametric study. *Applied Surface Science*, 138:617 – 621, 1999.

[71] P. Rabiei and P. Gunter. Optical and electro-optical properties of submicrometer lithium niobate slab waveguides prepared by crystal ion slicing and wafer bonding. *App. Phys. Lett.*, 85:4603 – 4005, 2004.

[72] A. Talneau, F. Lemarchand, A.-L. Fehrembach, and A. Sentenac. Impact of electronic lithography irregularities across mm-scale resonant grating filter performances. *Appl. Opt.*, 49:658 – 662, 2010.

[73] A.-L. Fehrembach, F. Lemarchand, and A. Talneau. High q polarization independent guided-mode resonance filter with "doubly periodic " etaced Ta2O5 bidimensional grating. *J. Lightwave Technol.*, 28:2037 – 2044, 2010.

[74] A.L. Fehrembach, O. Gauthier-Lafaye, A. Monmayrant KC. Yu, S. Bonnefont, E. Daran, P. Arguel, F. Lozes-Dupuy, and A. Sentenac. Measurement and modeling of 2D hexagonal resonant-grating filter performance. *J. Opt. Soc. Am. A*, 27:1535 – 1540, 2010.

[75] F. Jona and G. Shirane. *Ferroelectric crystals*. Dover Publications, New York, 1993.

[76] A. L. Affleck, J. Seaton, and C. Leach. Characterisation of the R-T response of BaTiO3 thermistors on three different length scales. *J. of the European Ceramic Society*, 12(27):3439 – 3444, 2007.

[77] N. S. Gajbhiye. Self regulating PTCR heaters based on semiconducting BaTiO3. pages 193 – 199. 1993. International Conference and Exhibition on Advances in Materials and Processes.

[78] Z. Q. Shi, Q. X. Jia, and W. A. Anderson. High-performance barium titanate capacitors with double layer structure. *J. Elec. Mat.*, 11(20):939 – 944, 1991.

[79] P. W. Rehrig, S. E. Park, S. T. McKinstry, G. L. Messing, B. Jones, and T. R. Shrout. Piezoelectric properties of zirconium-doped barium titanate single crystals grown by templated grain growth. *J. Applied Physics*, 86(3):1657 – 1661, 1999.

[80] V. K. Wadhawan. *Introduction to ferroic materials*. CRC Press, New York, 2000.

[81] P. S. Tang, D. Towner, T. Hamano, A. Meier, and B. Wessels. Electrooptic modulation up to 40 GHz in a barium titanate thin film waveguide modulator. *Opt. Expre.*, 12:5962 – 5967, 2004.

[82] Nanoparticle compatibility: New nanocomposite processing technique creates more powerful capacitors. http://gtresearchnews.gatech.edu/newsrelease/barium-titanate.htm.

[83] Ferroelectric and dielectric thin films. In H.S. Nalwa, editor, *Handbook of Thin Film Materials*, volume 3. Academic Press, London, 2002.

[84] M. W. Cole. G-doped Ba0.6Sr0.4TiO3 thin films for tunable microwave applications. *Appl. Phys. Lett.*, 2:77, 2004.

[85] B. W. Wessels. Ferroelectric oxide epitaxial thin films: synthesis and non-linear optical properties. *J. Cryst. Growth*, 25:706 – 710, 1998.

[86] M. Kawasaki, M. Yoshimoto, and H. Koinuma. Heteroepitaxial growth of BaTiO3 films on si by pulsed laser deposition. *Appl. Phys. Lett.*, 11:66, 1995.

[87] M. Melnichuk and L. T. Wood. Method for measuring off-diagonal kerr coefficients by using polarized light transmission. *J. Opt. Soc. Am. A*, 22:377 – 384, 2005.

[88] R. L.Holman, A. l. Johnson, and D. P. Skinner. The desirability of electrooptic ferroelectric materials for guided-wave optics. In *6th International Symposium on Applications of Ferroelectrics*, pages 32 – 41. Lehigh University, 1986.

[89] S. Laux, N. Kaiser, A. Zoller, R. Gutzelmann, H. Lauth, and H. Bernitzki. Room-temperature deposition of indium tin oxide thin films with plasma ion-assisted evaporation. *Thin Solid Films*, 335:1 – 5, 1998.

[90] L.-J. Meng and F. Placido. Annealing effect on ITO thin films prepared by microwave-enhanced dc reactive magnetron sputtering for telecommunication applications. *Surf. Coat. Tech.*, 166:44 – 50, 2003.

[91] S. A. Kemme, R. R. Boye, D. W. Peters, and R.O. Nellums. Active resonant subwavelength grating for scannerless range imaging sensors. In Shibin Jiang; Michel J. F. Digonnet, editor, *Optical Components and Materials IV*, volume 6469 of *Proc. SPIE*, 2007.

List of Figures

List of Tables

Appendix 1. S - Matrix Construction

From the Eq. 2.36 and 2.33 in chapter 2 , we can easily get

$$\mathbf{U}^{(p+1)} = \mathbf{R}_{ud}^{(p)}\mathbf{D}^{(p+1)}, \tag{5.1}$$

$$\mathbf{D}^{(0)} = \mathbf{T}_{dd}^{(p)}\mathbf{D}^{(p+1)} \tag{5.2}$$

If there is no incident waves in medium 0, then we can expand $\mathbf{U}^{(p+1)}$ and $\mathbf{D}^{(p+1)}$ by using divided matrix $\mathbf{t}^{(p)} = \begin{bmatrix} \mathbf{t}_{11}^{(p)} & \mathbf{t}_{12}^{(p)} \\ \mathbf{t}_{ud}^{(p)} & \mathbf{t}_{22}^{(p)} \end{bmatrix}$, then we get following relationship between layers $p+1^{th}$ and p^{th}:

$$\begin{aligned} \mathbf{U}^{(p+1)} &= \mathbf{t}_{11}^{(p)}\phi_{+}^{(p)}\mathbf{U}^{(p)} + \mathbf{t}_{12}^{(p)}\phi_{-}^{(p)}\mathbf{D}^{(p)} \\ \mathbf{D}^{(p+1)} &= \mathbf{t}_{21}^{(p)}\phi_{+}^{(p)}\mathbf{U}^{(p)} + \mathbf{t}_{22}^{(p)}\phi_{-}^{(p)}\mathbf{D}^{(p)} \end{aligned} \tag{5.3}$$

Underling the condition of Eq. 5.1, 5.2 and 5.3, by replacing all the $\mathbf{U}^{(p)}$, we get:

$$\mathbf{t}_{11}^{(n)}\phi_{+}^{(n)}\mathbf{R}_{ud}^{(n-1)}[\phi_{-}^{(n)}]^{-1} + \mathbf{t}_{12}^{(n)} = \mathbf{R}_{ud}^{(n)} * [\mathbf{t}_{21}^{(n)}\phi_{+}^{(n)}\mathbf{R}_{ud}^{(n-1)}[\phi_{-}^{(n)}]^{-1} + \mathbf{t}_{22}^{(n)}] \tag{5.4}$$

In this equation, a new notation Ω is introduced, where $\Omega^{(p)} = \phi_{+}^{(p)}\mathbf{R}_{ud}^{(p-1)}[\phi_{-}^{(p)}]^{-1}$. Then we can solve the equation and obtain the first part of S - Matrix:

$$\mathbf{R}_{ud}^{(p)} = [\mathbf{t}_{11}^{(p)}\Omega^{(p)} + \mathbf{t}_{12}^{(p)}][\mathbf{t}_{21}^{(p)}\Omega^{(p)} + \mathbf{t}_{22}^{(p)}]^{-1} \tag{5.5}$$

Using the Eq.5.3 again , replacing $\mathbf{D}^{(p+1)}$ by $\mathbf{t}_{21}^{(p)}\phi_{+}^{(p)}\mathbf{U}^{(p)} + \mathbf{t}_{22}^{(p)}\phi_{-}^{(p)}\mathbf{D}^{(n)}$,and replacing $\mathbf{U}^{(p)}$ with $\mathbf{R}_{ud}^{(p-1)}\mathbf{D}^{(p)}$, then we get the relation of $\mathbf{T}_{dd}^{(p)}$ and $\mathbf{T}_{dd}^{(p-1)}$,

$$\mathbf{T}_{dd}^{(p)}(\mathbf{t}_{21}^{(p)}\Omega^{(p)} + \mathbf{t}_{22}^{(p)}) = \mathbf{T}_{dd}^{(p-1)}[\phi_{-}^{(p)}]^{-1} \tag{5.6}$$

Solving this equation, we get the second part of **S** - Matrix:

$$\mathbf{T}_{dd}^{(p)} = \mathbf{T}_{dd}^{(p-1)}[\phi_{-}^{(p)}]^{-1}(\mathbf{t}_{21}^{(p)}\Omega^{(p)} + \mathbf{t}_{22}^{(p)}) \tag{5.7}$$

Taking advantage of the similar approach, the other two parts of **S** - Matrix can be achieved and shown in Eq.2.36.

Appendix 2. Schema of Structures

This appendix provides a summary of the structures mentioned in the thesis. For each structure, the graphic symbol recalls the structure serial number, type, and the purpose for which the structure has been studied. Patterns specify the parameters of structures.

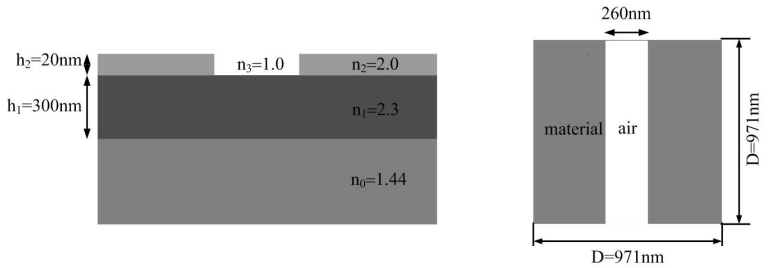

Figure 5.1 : *Structure 1.1 - simple guided mode resonant grating model in the Chapter 1.*

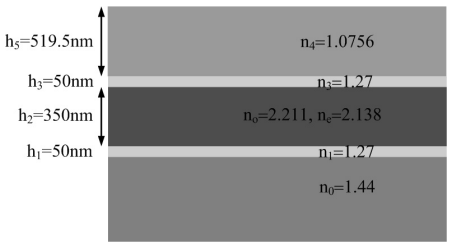

Figure 5.2 : *Structure 3.1 - equivalent structure in the Chapter 3.*

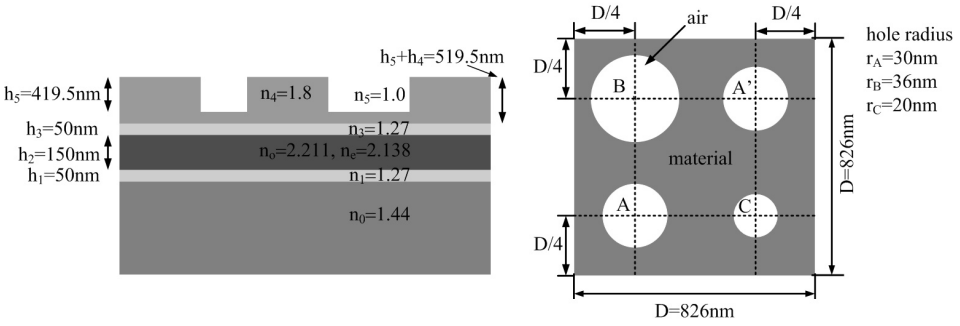

Figure 5.3 : *Structure 3.2 - GMR grating with $LiNbO_3$ correspond to point A in the reflected field map Fig. 3.5. - research the influence of the profile of the guided mode field, also be used to analysis the GMR filter characters in the Chapter 3.*

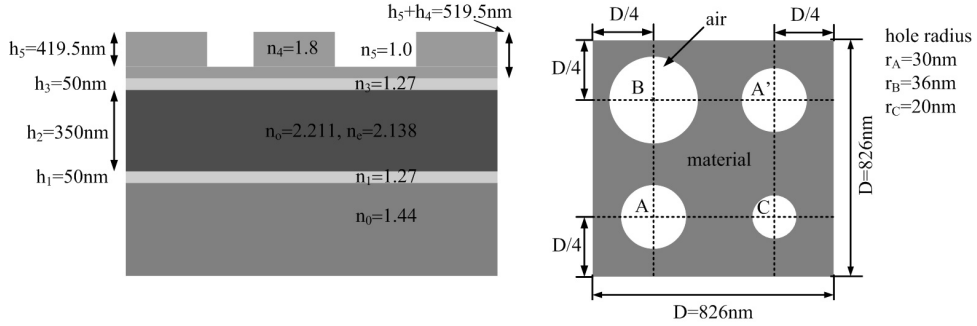

Figure 5.4 : *Structure 3.3 - GMR grating with $LiNbO_3$ correspond to point B in the reflected field map Fig. 3.5. - research the influence of the profile of the guided mode field*

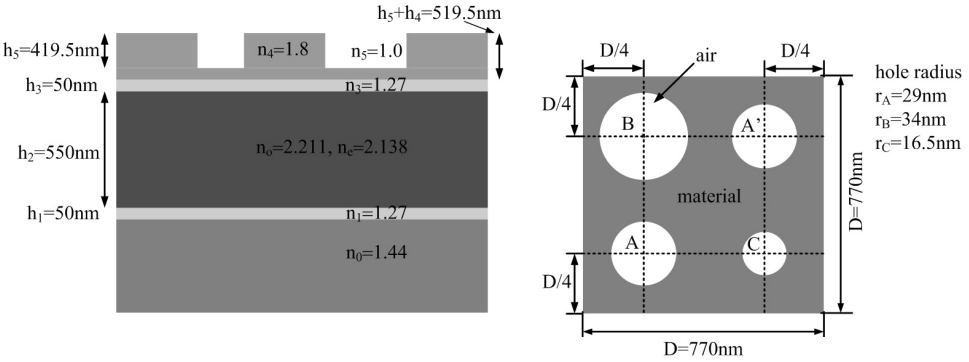

Figure 5.5 : *Structure 3.4 - GMR grating with $LiNbO_3$ correspond to points C and D in the reflected field map Fig. 3.5. - research the influence of the profile of the guided mode field*

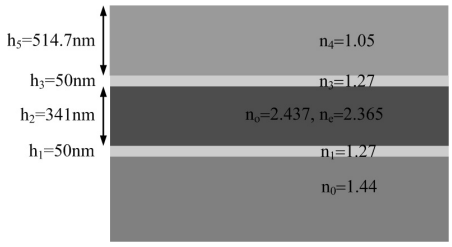

Figure 5.6 : *Structure 4.1 - equivalent structure in the Chapter 4.*

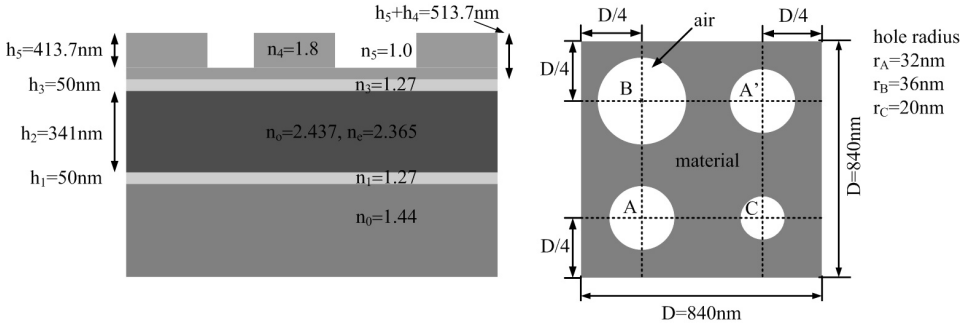

Figure 5.7 : *Structure 4.2 - GMR grating with $BaTiO_3$ correspond to point A in the reflected field map Fig. 4.6. - to analysis the tunability and peak linewidth and angular tolerance characters for the first order modes in the Chapter 4.*

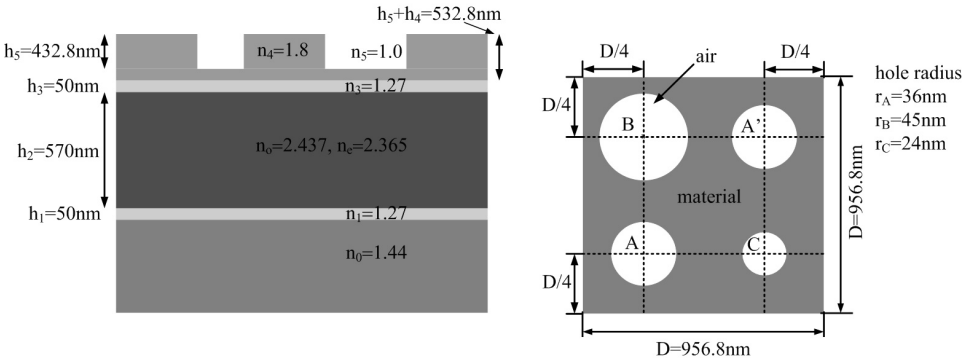

Figure 5.8 : *Structure 4.3 - GMR grating with $BaTiO_3$ correspond to point B in the reflected field map Fig. 4.6. - to analysis the tunability, peak linewidth and angular tolerance characters for the second order modes in the Chapter 4.*

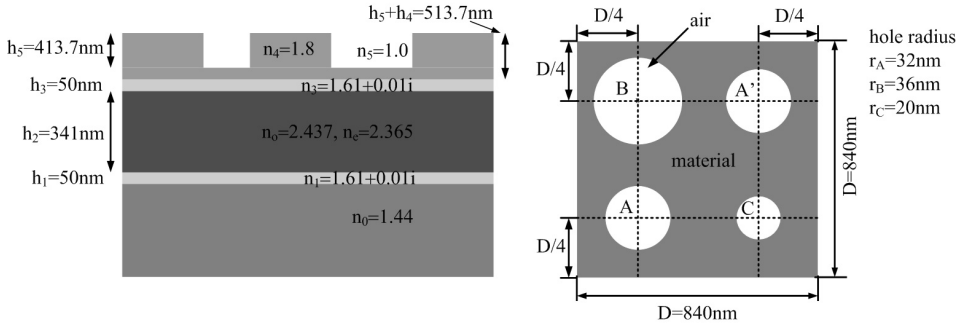

Figure 5.9 : *Structure 4.4 - GMR grating composed with $BaTiO_3$ layer and ITO layer with absorption. - to test the affect on the resonant peak caused by ITO layer with different coefficients k.*

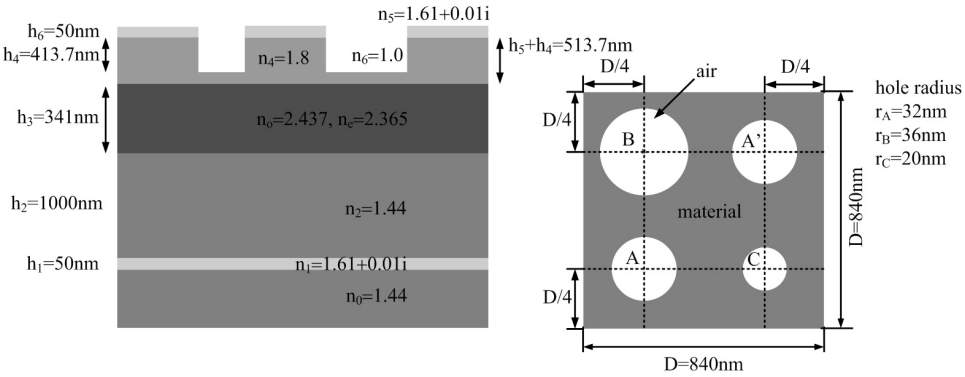

Figure 5.10 : *Structure 4.5 - optimized GMR filter configuration with $BaTiO_3$ layer and ITO layer. - to decrease the influence of ITO absorption on reflective efficient by optimize the stack composition.*

Summary

Tunable Resonant Narrow-Band Filter Based on Electro-optic Materials

A resonant grating filter is a simple structure composed of a stack of a few dielectric layers on which a sub-wavelength grating is engraved. Their main interest is the narrow spectral FWHM they can achieve: in practice, quality factors greater than 7000 have already been obtained. The potential application fields are: optical telecommunications, spectroscopy, lasers, sensoring, etc. We aim to develop the potential of resonant grating filters by studying the tunability of their center wavelength by electro-optic effect. We chose two materials, Lithium Niobate and Barium Titanate, because of their large electro-optic coefficients. We developed a numerical tool based on the Fourier Modal Method including anisotropic materials. This is indispensable to analysis the effects related to the incident polarization. We compared several configurations, allowing a strong (up to 90nm) or weak tunability, independent or not versus the incident polarization. For each case, a physical interpretation is given for the facts that are observed. Last, we conclude by practical considerations concerning the feasibility of the structures and the influence of the absorption losses.

Key words: Diffraction gratings, guided mode resonance, tunable filter, electro-optical effect, angular tolerance, polarization independence

Réseaux Résonnants Accordables pour Filtrage Optique à Bande Étroite

Un filtre à réseau résonnant est une structure simple composée d'un empilement de quelques couches de matériau diélectrique sur lequel est gravé un réseau sub-longueur d'onde. Leur atout principal est la finesse spectrale accessible: en pratique, des facteurs de qualité supérieurs à 7000 ont déjà été obtenus. Les domaines d'applications concernés sont les télécommunications optique, la spectroscopie, les lasers, la détection...Nous souhaitons développer le potentiel des filtres à réseau résonnants en étudiant la possibilité d'accorder leur longueur d'onde de centrage par effet électro-optique. Nous avons choisi deux matériaux électro-optiques, le Niobate de Lithium et le Titanate de Baryum, en raison de leurs fortes propriétés électro-optiques. Nous avons développé un outil numérique basé sur la Méthode Modale de Fourier incluant des matériaux anisotropes. Ceci est indispensable pour analyser les effets liés à la polarisation de l'onde incidente. Nous avons comparé différentes configurations, permettant une accordabilité forte (jusqu'à 90nm) ou faible, indépendante ou non de la polarisation. Pour chaque cas, une interprétation physique des

effets observés est donnée. Enfin, nous concluons par des considérations pratiques concernant la fabricabilité des structures et l'influence des pertes par absorption.

Mot clés: Réseaux de diffraction, résonance de mode guidé, filtre accordable, effet électro-optique, tolérance angulaire, indépendance polarisation